



Advanced Automated HVAC Fault Detection and Diagnostics Commercialization Program

**California Energy Commission
Contract # 500-03-030**

D5.4b – Final Report Describing the Development of Refrigeration Cycle, Temperature-Only Refrigeration Cycle Diagnostics (Subtasks 5.4.1 and 5.4.6)

June 28, 2005

Submitted To:
Accounting Office, MS-2
California Energy Commission
1516 Ninth Street, 1st Floor
Sacramento, CA 95814

Submitted By:
Architectural Energy Corporation
2540 Frontier Avenue, Suite 201
Boulder, Colorado 80301

Prepared By:
Purdue University, Mechanical Engineering
1077 Ray W. Herrick Laboratories
West Lafayette, IN 47907-1077

THIS REPORT WAS PREPARED AS A RESULT OF WORK SPONSORED BY THE CALIFORNIA ENERGY COMMISSION (COMMISSION). IT DOES NOT NECESSARILY REPRESENT THE VIEWS OF THE COMMISSION, ITS EMPLOYEES, OR THE STATE OF CALIFORNIA. THE COMMISSION, THE STATE OF CALIFORNIA, ITS EMPLOYEES, CONTRACTORS, AND SUBCONTRACTORS MAKE NO WARRANTY, EXPRESS OR IMPLIED, AND ASSUME NO LEGAL LIABILITY FOR THE INFORMATION IN THIS REPORT; NOR DOES ANY PARTY REPRESENT THAT THE USE OF THIS INFORMATION WILL NOT INFRINGE UPON PRIVATELY OWNED RIGHTS. THIS REPORT HAS NOT BEEN APPROVED OR DISAPPROVED BY THE COMMISSION NOR HAS THE COMMISSION PASSED UPON THE ACCURACY OR ADEQUACY OF THE INFORMATION IN THIS REPORT.

©2005, PURDUE UNIVERSITY, MECHANICAL ENGINEERING.
ALL RIGHTS RESERVED.

TABLE OF CONTENTS

TABLE OF CONTENTS.....	1
LIST OF FIGURES	3
LIST OF TABLES	5
NOMENCLATURE	6
1 Introduction.....	7
2 Field Emulation Testing and Validation of Decoupling-Based FDD	8
2.1 Implementation of Decoupling-Based FDD.....	8
2.1.1.1 Compressor Module.....	10
2.1.1.2 Condenser Module	11
2.1.1.3 Evaporator Module	12
2.1.1.4 EXPFD Module	12
2.1.1.5 Refrigerant Charge Module	13
2.2 Sensitivity	13
2.3 Robustness	15
3 Virtual Pressure sensors and Temperature Sensor Only FDD.....	24
3.1 Introduction.....	24
3.2 Virtual Pressure Sensors	25
3.2.1 Temperature Sensor Location.....	25
3.2.1.1 Physical Analysis	25
3.2.1.2 Experimental Validation	28
3.2.2 Pressure Estimation Method.....	31
3.3 Temperature Sensor Only FDD	39
3.3.1 Uncertainty Analysis	39
3.3.2 Experimental Validation.....	40
3.3.2.1 System I -- Packaged fixed orifice air conditioners.....	40

3.3.2.2 System II -- Split fixed orifice air conditioners	48
3.3.2.3 System III -- Split TXV air conditioners	50
3.4 Conclusions.....	53
4 Performance Monitoring Indices	54
4.1 Comfort and Indoor Air Quality Indices.....	54
4.2 Efficiency and Economic Indices	56
4.3 Reliability Index.....	57
4.4 Control and miscellaneous indices.....	58
References.....	62
Appendix A Condenser and Evaporator Tube Bend Temperature Profile	63
A. 1 Varying Charge with Dry Coil	63
A.2 Varying Charge with Wet Coil.....	66
A.3 Varying Ambient Temperature with Dry Coil	69
A.4 Varying Evaporator Air Flow (Wet)	71
A.5 Varying Condenser Air Flow (Wet).....	73

LIST OF FIGURES

Figure 2.1: Decoupling-based FDD implementation information flow.....	9
Figure 2.2: Decoupling-based FDD implementation sequence	10
Figure 2.3: Compressor module implementation sequence	11
Figure 2.4: Condenser module implementation sequence	12
Figure 2.5: Evaporator module implementation sequence	12
Figure 2.6: EXPFD module implementation sequence.....	13
Figure 2.7: Refrigerant charge module implementation sequence	13
Figure 2.8: Robustness test for multiple-simultaneous-fault FDD	18
Figure 2.9: FDD Robustness for Compressor Leakage	19
Figure 2.10: FDD Robustness for Condenser Fouling.....	20
Figure 2.11: FDD Robustness for Evaporator Fouling.....	21
Figure 2.12: FDD Robustness for Liquid-line Restriction.....	21
Figure 2.13: FDD Robustness for Refrigerant Charge Faults.....	22
Figure 3.1 Block diagram for a typical vapor compression system.....	26
Figure 3.2 Heat transfer in the condenser de-superheat section	27
Figure 3.3 Simulation of the refrigerant superheat profile across the condenser	27
Figure 3.4 Refrigerant superheat profile across the condenser under nominal charge (for a split TXV system).....	29
Figure 3.5 Refrigerant superheat profile across the condenser under 50% of nominal charge (for a split TXV system)	29
Figure 3.6 Refrigerant superheat profile across the condenser under 150% of nominal charge (for a split TXV system)	30
Figure 3.7 Refrigerant superheat profile across the evaporator under nominal charge (for a split TXV system).....	30
Figure 3.8 Refrigerant superheat profile across the evaporator under 50% of nominal charge (for a split TXV system)	31
Figure 3.9 Refrigerant superheat profile across the evaporator under 150% of nominal charge (for a split TXV system)	31
Figure 3.10 Type I condenser structure	32
Figure 3.11 Type II condenser structure.....	33
Figure 3.12 Type III condenser structure.....	34
Figure 3.13 Refrigerant local pressure profile across a type I condenser (with R410a)...	34
Figure 3.14 Refrigerant local pressure profile across a type II condenser (with R410a) .	35
Figure 3.15 Discharge-line and liquid-line pressures vs. virtual condensing pressure calculated from surface temperature at 4 th return bend (Packaged AC with R410a).....	36
Figure 3.16 Suction-line pressure vs. saturated pressures calculated from surface temperature at the inlet of evaporator	38

Figure 3.17 Virtual suction-line pressure vs. measured suction-line pressure	41
Figure 3.18 Virtual liquid-line pressure vs. measured liquid-line pressure	42
Figure 3.19 Virtual discharge-line pressure vs. measured discharge-line pressure	42
Figure 3.20 Liquid-line subcooling using virtual pressures vs. liquid-line subcooling using measured pressure	43
Figure 3.21 Suction-line superheat using virtual pressure vs. suction-line superheat using measured pressures	43
Figure 3.22 Refrigerant mass flow rate using virtual pressure vs. refrigerant mass flow rate using measured pressure	44
Figure 3.23 Compressor power consumption using virtual pressure vs. compressor power consumption using measured pressure.....	44
Figure 3.24 Compressor leakage indicator determined using virtual pressure vs. compressor leakage indicator determined using measured pressure.....	45
Figure 3.25 Condenser fouling indicator obtained using virtual pressure vs. condenser fouling indicator obtained using measured pressure	46
Figure 3.26 Evaporator fouling indicator from virtual pressure vs. evaporator fouling indicator from measured pressure	47
Figure 3.27 Refrigerant charge fault indicator from virtual pressure vs. refrigerant charge fault indicator from measured pressure	48
Figure 3.28 Compressor leakage indicator from virtual pressure vs. compressor leakage indicator from measured pressure	49
Figure 3.29 Condenser fouling indicator from virtual pressure vs. condenser fouling indicator from measured pressure	49
Figure 3.30 Evaporator fouling indicator from virtual pressure vs. evaporator fouling indicator from measured pressure	50
Figure 3.31 Refrigerant charge fault indicator from virtual pressure vs. refrigerant charge fault indicator from measured pressure	50
Figure 3.32 Compressor leakage indicator from virtual pressure vs. compressor leakage indicator from measured pressure	51
Figure 3.33 Condenser fouling indicator from virtual pressure vs. condenser fouling indicator from measured pressure	52
Figure 3.34 Evaporator fouling indicator from virtual pressure vs. evaporator fouling indicator from measured pressure	52
Figure 3.35 Refrigerant charge fault indicator from virtual pressure vs. refrigerant charge fault indicator from measured pressure	53
Figure 4.1 Thermal comfort plot in psychrometric chart.....	55
Figure 4.2 Actual cooling capacity vs. normal cooling capacity for the packaged air conditioner with R410a as the refrigerant and FXO as the expansion device	55
Figure 4.3 Outdoor air fraction plot.....	56
Figure 4.4 Actual EER vs. normal EER for the packaged air conditioner with R410a as the refrigerant and FXO as the expansion device	57
Figure 4.5 Definition of a compressor run cycle	59
Figure 4.6 Compressor runtime plot	59
Figure 4.7 Compressor off time plot.....	60
Figure 4.8 Economizer operation plot	61

LIST OF TABLES

Table 2.1: Predefined feature values and FDD thresholds	9
Table 2.2: Method of implementing faults and corresponding fault levels simulated.....	14
Table 2.3: FDD sensitivity for individual faults	14
Table 2.4: Fault indicator standard deviations of normal operations and false alarm rates	15
Table 2.5: Individual fault levels implemented in multiple-simultaneous-fault.....	16
Table 2.6: Indicators numbers for the different faults implemented in multiple-simultaneous fault combinations	17
Table 2.7: Normalized fault indicator error and its meaning.....	18
Table 3.1 Typical pressure drop value across different condenser sections	35
Table 3.2 Pressure drop across the condenser sections and evaporator.....	36
Table 3.3 Calculated variables and uncertainties.....	39
Table 3.3 Calculated variables and uncertainties when using virtual pressure sensors....	41

NOMENCLATURE

EER	= Equipment efficiency ratio
$EPDI$	= Economic performance degradation index
FDD	= Fault detection and diagnosis
FXO	= Fixed orifice
HVAC	= Heating, Ventilating, and Air-Conditioning
\dot{m}_{ref}	= Refrigerant mass flow rate
MAT	= Mixed air temperature
P_{cond}	= Condensing pressure
P_{dis}	= Discharge pressure
P_{evap}	= Evaporating pressure
P_{ll}	= Liquid line pressure
P_{suc}	= Suction pressure
\dot{Q}_{cap}	= Cooling capacity
SHR	= Sensible heat ratio
SRB	= Statistical rule-based
RTU	= Rooftop unit
$T_{air,inlet}$	= Inlet air temperature
T_{amb}	= Ambient temperature
T_{cond}	= Condensing temperature
T_{dis}	= Discharge line temperature
T_{evap}	= Evaporating temperature
T_{ll}	= Liquid line temperature
$T_{ref,x}$	= Refrigerant temperature at position x
$T_{ref,inlet}$	= Inlet refrigerant temperature
TXV	= Thermostatic expansion valve
T_{sc}	= Sub-cooling
T_{sh}	= Superheat

1 INTRODUCTION

In a first phase CEC sponsored project, a decoupling-based FDD technique was developed, which handles multiple-simultaneous faults and eliminates a cost-prohibitive system model to do FDD. In this previous work, the decoupling features were verified using laboratory data for a fixed-orifice system. Then the complete decoupling-based FDD technique was demonstrated using a prototype in which four types of faults were artificially introduced one by one and removed one by one. In the current project, FDD performance was evaluated further. Chapter 2 of this report presents a detailed evaluation of the sensitivity and robustness which was tested using data from the prototype under a range of conditions.

In an extension to the first phase project (Braun and Li, 2004a), pressure sensor issues were initially addressed. There is a high risk of introducing refrigerant leaks when installing pressure sensors at the service ports. Therefore, FDSI investigated a more robust method for installing pressure sensors using a capillary tube and Purdue initially investigated a method for obtaining pressure values using virtual/soft pressure sensors. This method not only permanently eliminates the leakage problem but also leads to significantly lower initial costs for automated diagnostics applied to air conditioning and refrigeration applications. In this method, two temperature sensors were used for each heat exchanger coil to obtain target pressures. In order to reduce implementation costs and simplify the installation procedure, Chapter 3 of this report presents a method which uses only one temperature sensor for each heat exchanger coil to obtain pressures. With the virtual pressure sensors combined with the decoupling-based FDD, a temperature only FDD technique is developed. The whole technique has been validated using extensive experimental data.

In Chapter 4 of this report, simple indices are developed to evaluate the performance of the monitored system. These indices should be determined from low-cost measurements and measure impact on comfort, indoor air quality, efficiency, reliability, control performance, etc.

2 FIELD EMULATION TESTING AND VALIDATION OF DECOUPLING-BASED FDD

This chapter first describes how to implement the whole decoupling-based FDD technique, and then validates its sensitivity and robustness using Purdue field emulation testing data.

2.1 Implementation of Decoupling-Based FDD

The simplified one-dimensional normalized distance fault detection classifier described in Phase I final report (Braun and Li, 2004b) is adopted. In order to make the diagnosis classifier more generic, a normalized fault indicator is defined by normalizing the decoupling feature as,

$$IND_{faultname} = \frac{fv_{current}}{fv_{predefined}},$$

where $IND_{faultname}$ denotes the fault indicator of the corresponding $faultname$, $fv_{current}$ denotes the current feature value, and $fv_{predefined}$ is the predefined feature value. The $fv_{predefined}$ is originally chosen as the feature value at an individual fault level causing approximately 20% cooling capacity degradation. Table 2.1 summarizes all the $fv_{predefined}$'s and FDD thresholds which approximately correspond to a 4% of capacity degradation for the Purdue prototype. The thresholds were chosen based on the sensitivity of the method and economic necessity. All the values would be generic for refrigeration systems that use R22.

Figure 2.1 illustrates how to implement decoupling-based FDD. It can be seen the decoupling-based approach uses component models rather than overall system models to do FDD. The information flow in and out of each component model is shown in Figure 2.1, which begins with the system core part, the compressor.

Table 2.1: Predefined feature values and FDD thresholds

Fault name	<i>compleak</i>	<i>condfoul</i>	<i>evapfoul</i>	<i>llrestr</i>	<i>reflow</i>	<i>refover</i>
Feature	ΔT_{dis}	$\Delta \dot{V}_{ca}$	$\Delta \dot{V}_{ea}$	$\Delta^2 P_{ll}$	ΔT_{sh-sc}	ΔT_{sh-sc}
$fV_{predefined}$	15 (F)	$0.25 \dot{V}_{ca,setting}$	$0.25 \dot{V}_{ea,setting}$	4.4 (bar)	10 (F)	10 (F)
Threshold	0.2	0.2	0.2	0.2	0.2	-0.2

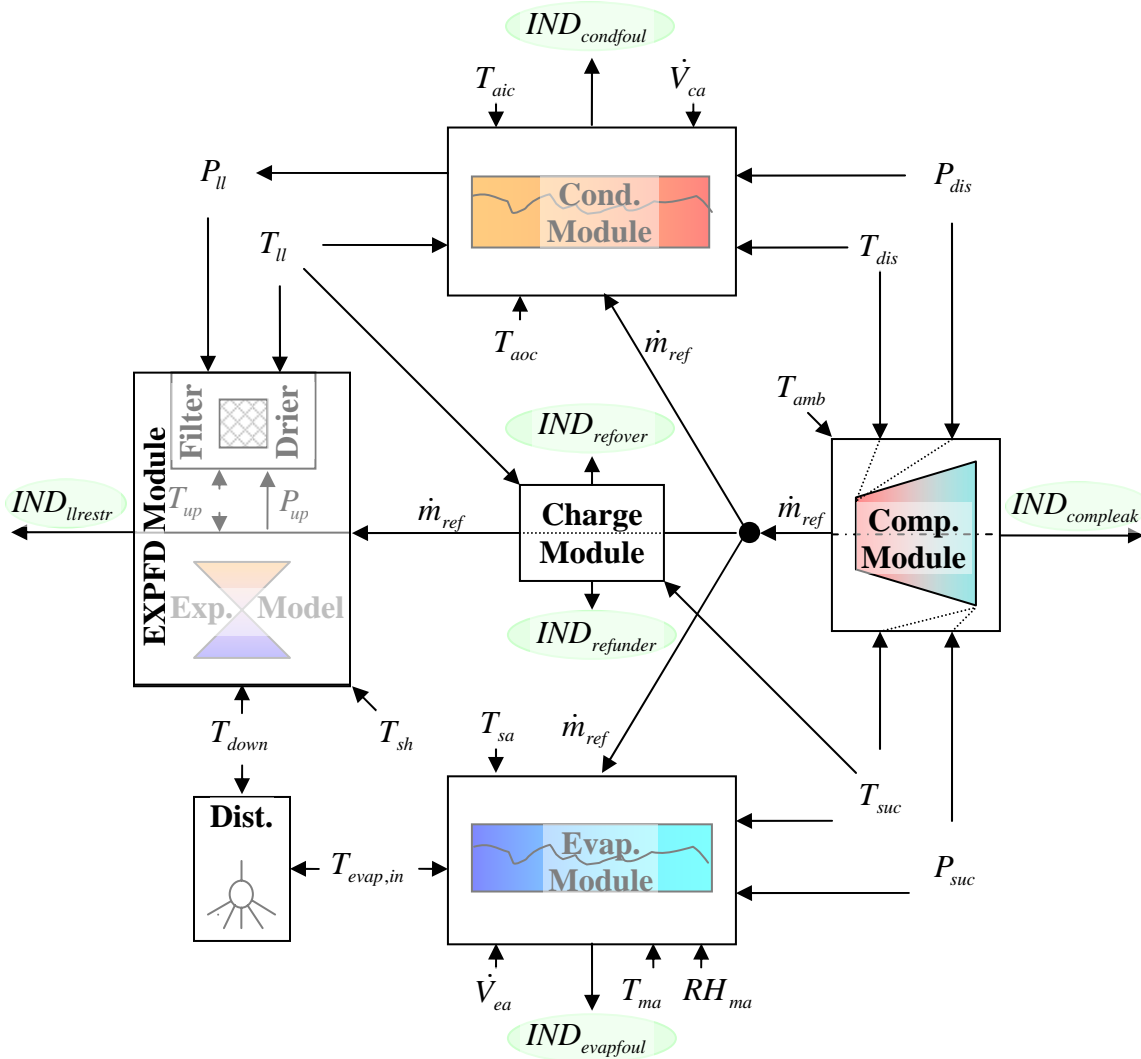


Figure 2.1: Decoupling-based FDD implementation information flow

Figure 2.2 describes the sequence of steps used to do FDD. Firstly, FDD can be done on a compressor using the compressor model alone and refrigerant mass flow rate can be estimated for future use in all the other component models. Secondly, FDD on an evaporator and a condenser can be performed using condenser and evaporator models and the pressure in the liquid-line before the filter/drier can be estimated for use in liquid-line restriction diagnosis.

Having obtained the liquid-line pressure before the filter/drier, liquid-line restriction diagnosis can be made using the expansion device model to estimate the pressure after the filter/drier. Diagnosis of system charge can be accomplished using the estimated condenser outlet subcooling and measured evaporator inlet superheat. The details of using component models are described in the following sections.

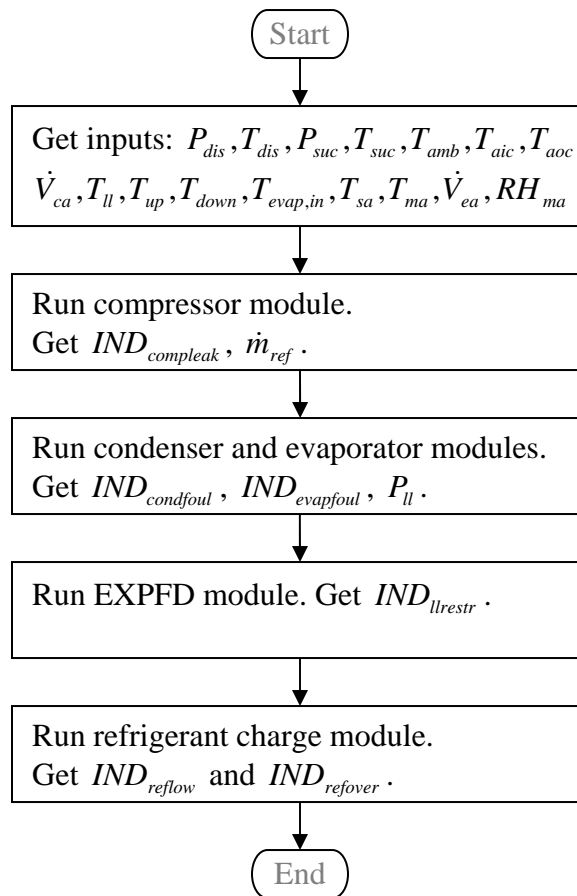


Figure 2.2: Decoupling-based FDD implementation sequence

2.1.1.1 Compressor Module

Figure 2.3 illustrates the compressor module implementation flow chart. Two models are used: a compressor map model and a compressor energy balance model. If the compressor power consumption measurement, \dot{w}_{meas} , is available, use it as the input of the compressor energy

balance model to predict refrigerant mass flow rate, and otherwise, use the predicted value, \dot{w}_{pred} , as the input.

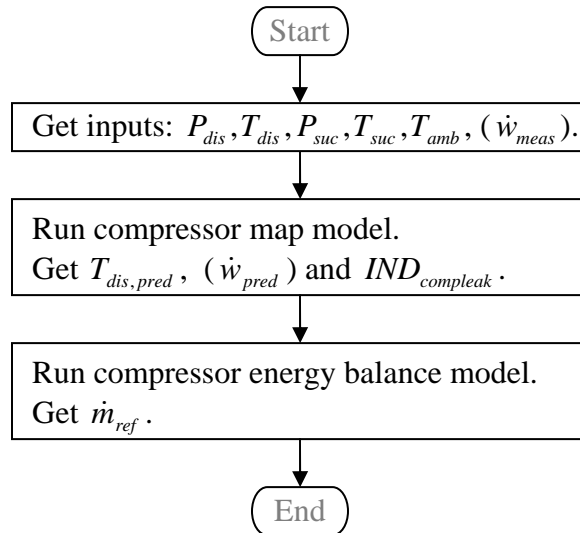


Figure 2.3: Compressor module implementation sequence

2.1.1.2 Condenser Module

As shown in Figure 2.4, the condenser module uses two models: a condenser pressure drop model or a condenser outlet pressure virtual sensor and a condenser energy balance model (Li, 2004).

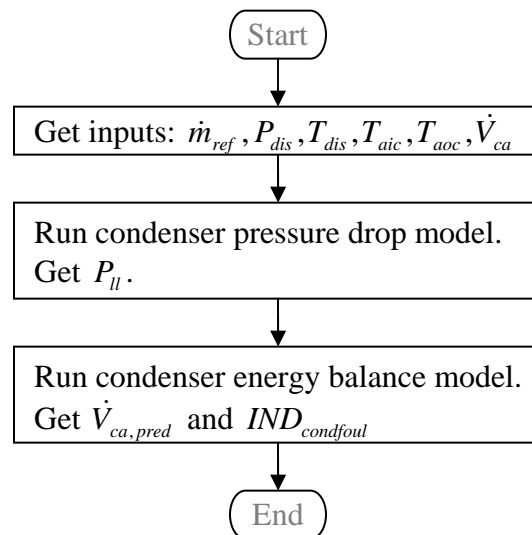


Figure 2.4: Condenser module implementation sequence

2.1.1.3 Evaporator Module

Similar to the condenser module (see Figure 2.5), the evaporator module uses two models: a supply air humidity virtual sensor and an evaporator energy balance model (Li, 2004).

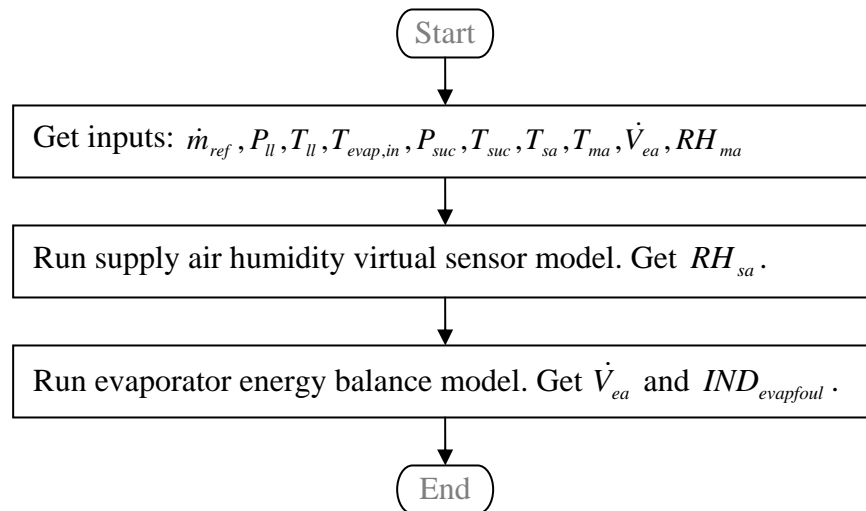


Figure 2.5: Evaporator module implementation sequence

2.1.1.4 EXPFD Module

As shown in Figure 2.6, the EXPFD module uses the expansion device model to estimate the expansion device upstream pressure P_{up} which was described in a previous report (Braun and Li, 2004b). Having obtained the pressures before and after the filter/drier, a fault indicator for a liquid-line restriction can be obtained.

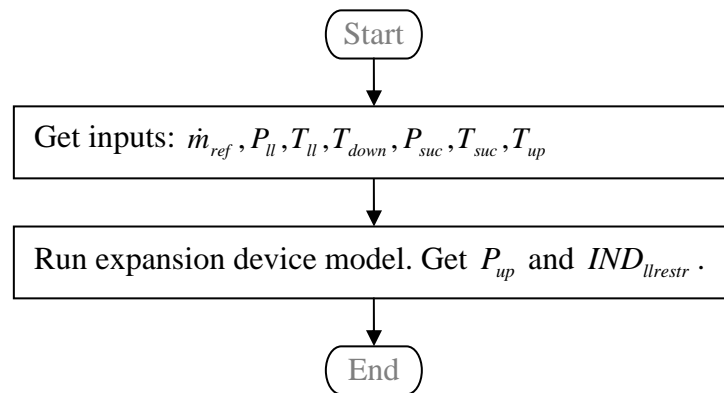


Figure 2.6: EXPFD module implementation sequence

2.1.1.5 Refrigerant Charge Module

The refrigerant charge module (see Figure 2.7) first calculates the liquid-line subcooling and suction line superheat and then calculates the charge fault indicator, $IND_{refcharge}$.

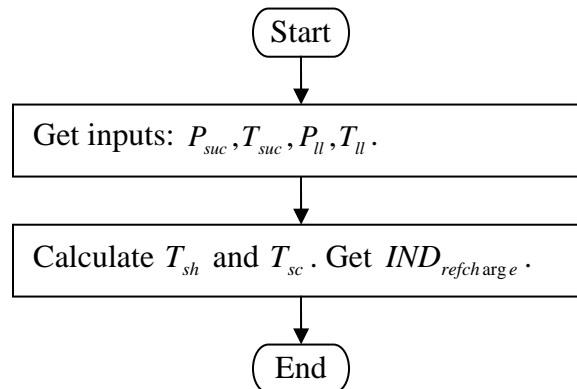


Figure 2.7: Refrigerant charge module implementation sequence

2.2 Sensitivity

For a given fault, the sensitivity of the FDD technique is defined as the lowest fault level that can be successfully detected and diagnosed. Since there are infinite combinations of multiple faults with different fault levels, sensitivity was only evaluated for individual faults. Table 2.2 tabulates the method of implementing faults and corresponding fault levels simulated. Six faults were implemented at the Purdue field site: compressor valve leakage (Compleak), condenser fouling (Condfool), evaporator fouling (Evapfool), liquid-line restriction (Llrestr), refrigerant low charge (Reflow), and refrigerant over charge (Refover). Except for refrigerant charge and

compressor leakage faults for which five fault levels were introduced, four fault levels were introduced for the other three faults. Since tests were performed in the field, the driving conditions were uncontrollable. Typically, they were conducted in the afternoon (from around 1:30 pm to 8:00 pm) when there was no direct solar radiation to sensors. Most of the tests were performed in the summer and fall of 2003 and part of them were conducted in the spring of 2004.

Table 2.2: Method of implementing faults and corresponding fault levels simulated

Faults	Simulation Method	Fault Level Expression	Fault Level Simulated					
			0	1	2	3	4	5
Comp-leak	Partially open a bypass valve between discharge and suction lines	% refrigerant mass flow rate bypass	0%	8%	18%	33%	44%	56%
Cond fou 1	Partially block condenser air flow with paper	% reduction of air volume flow rate	0%	3%	10%	13%	16%	
Evap fou 1	Partially block evaporator air flow with paper	% reduction of air volume flow rate	0%	5%	9%	16%	31%	
Llrestr	Partially close the needle valve on the liquid line	% of the pressure drop from high to low sides	0%	5%	10%	13%	19%	
Reflow	Under-charge the system	% reduction of charge	0%	11%	16%	21%	26%	32%
Refover	Over-charge the system	% increase of charge	0%	11%	16%	21%	26%	32%

Table 2.3 summarizes the FDD sensitivity results. δ_{cap} , δ_{EER} and δ_{SHR} stand for degradation in cooling capacity, energy efficiency ratio (EER) and sensible heat ratio (SHR), respectively. In terms of economic performance degradation index (EPDI) (Braun and Li, 2004a), compressor leakage and liquid-line restriction and refrigerant over charge faults have the highest sensitivities while evaporator fouling and refrigerant charge faults have the lowest sensitivities. In terms of physical fault level, compressor valve leakage and evaporator fouling faults have the highest sensitivities while refrigerant overcharge has the lowest sensitivity. Overall, all individual faults can be identified before they cause 5% of degradation in cooling capacity and EER and SHR and their EPDI reaches 10%.

Table 2.3: FDD sensitivity for individual faults

Faults	Sensitivity
--------	-------------

	Simulated Level	Physical Level	δ_{cap}	δ_{EER}	δ_{SHR}	<i>EPDI</i>
Compnv	1st	8%	5%	3%	-3%	2%
Condfovl	2nd	10%	3%	4%	0%	4%
Evapfoul	2nd	9%	5%	4%	4%	9%
Llrestr	2nd	10%	3%	1%	2%	3%
Refleak	1st	11%	3%	1%	5%	7%
Refover	2nd	16%	2%	2%	0%	2%

Since implementation of one fault at different levels took from three to four hours of a single afternoon, the driving conditions changes but there were no drastic changes of in temperature and humidity. Therefore, although sensitivities in terms of physical level were stable, sensitivities in terms of performance degradation had small variations, because performance degradations vary with driving conditions.

False alarm is an indication of a fault when in actuality a fault has not occurred. For a given technique, there is an inherent tradeoff between minimizing the false alarms and maximizing sensitivity. Table 2.4 lists the theoretical false alarm rates calculated from the fault indicator standard deviations. Except for the liquid-line restriction, all the other faults have very small false alarm rates. Since the sensitivity of liquid-line restriction is high, it seems that there is some potential to reduce its false alarm rate by means of raising the FDD threshold further. However, robustness tests show that it is impractical to raise the FDD threshold.

Table 2.4: Fault indicator standard deviations of normal operations and false alarm rates

Fault Name	Compnv	Condfovl	Evapfoul	Llrestr	Reflow	Refover
FDD Threshold	0.2	0.2	0.2	0.2	0.2	-0.2
Standard Deviation	0.072	0.074	0.091	0.133	0.066	0.066
False Alarm Rate	0.003	0.004	0.014	0.067	0.005	0.005

2.3 Robustness

To verify robustness, multiple-simultaneous fault combinations for six faults were considered. Only one fault level was implemented for each combination, because there are infinite combinations if fault level is considered. Except for compressor leakage, all the other faults were implemented at the levels between the first diagnosed and next levels (see Table 2.5). Compressor valve leakage was tested over a rang of fault levels because 1) a compressor leakage

fault is completely decoupled from the other faults and has the highest robustness while other faults are unilaterally decoupled from it, 2) various compressor leakage faults are required to test the fault evaluation algorithm, and 3) high levels of compressor leakage faults are better for robustness tests of other faults. Fault levels of condenser fouling and liquid-line restriction and refrigerant overcharge were fixed, while two fault levels of refrigerant leakage and evaporator fouling were simulated and compressor leakage fault levels ranged from 20% to 35%. Since refrigerant low charge fault can not occur simultaneously with refrigerant over charge fault, the total number of combinations is the sum of those at low charge,

$$C_r^1 + C_4^2 + C_4^3 + C_4^4 = 15 ,$$

normal charge,

$$C_4^2 + C_4^3 + C_4^4 = 11 ,$$

and over charge,

$$C_r^1 + C_4^2 + C_4^3 + C_4^4 = 15 .$$

All forty-one combinations with individual fault levels implemented are listed in Table 2.5.

Table 2.5: Individual fault levels implemented in multiple-simultaneous-fault

Test No.	comp nv	condfo ul	evapfo ul	llrest r	refle ak	refov er
1	27%	0	0	0	14%	0
2	27%	11%	0	0	14%	0
3	25%	11%	12%	0	11%	0
4	25%	11%	12%	12%	11%	0
5	0	11%	12%	12%	11%	0
6	0	0	12%	12%	11%	0
7	0	0	0	12%	14%	0
8	29%	0	0	12%	14%	0
9	25%	0	12%	12%	11%	0
10	25%	0	12%	0	11%	0
11	0	0	12%	0	11%	0
12	0	11%	12%	0	11%	0
13	0	11%	0	0	14%	0
14	0	11%	0	12%	14%	0
15	29%	11%	0	12%	14%	0
16	32%	11%	0	0	0	0
17	21%	11%	12%	0	0	0

18	21%	11%	12%	12%	0	0
19	0	11%	12%	12%	0	0
20	0	0	12%	12%	0	0
21	19%	0	12%	12%	0	0
22	32%	0	0	12%	0	0
23	0	11%	0	12%	0	0
24	32%	11%	0	12%	0	0
25	0	11%	12%	0	0	0
26	19%	0	12%	0	0	0
27	33%	0	0	0	0	21%
28	32%	11%	0	0	0	21%
29	35%	11%	16%	0	0	21%
30	35%	11%	16%	12%	0	21%
31	0	11%	16%	12%	0	21%
32	0	0	16%	12%	0	21%
33	0	0	0	12%	0	21%
34	32%	0	0	12%	0	21%
35	35%	0	16%	12%	0	21%
36	35%	0	16%	0	0	21%
37	0	0	16%	0	0	21%
38	0	11%	16%	0	0	21%
39	0	11%	0	0	0	21%
40	0	11%	0	12%	0	21%
41	32%	11%	0	12%	0	21%

All the possible forty-one combinations were considered. For reference, indicators for the different faults are given in Table 2.6. Figure 2.8 shows the different combinations of faults implemented for the forty-one different cases and also shows differences between binary indicators (1=fault, 0=no fault) for individual diagnosed and implemented faults. A '-1' denotes a missed diagnosis or sensitivity loss for one fault and a '1' denotes a false alarm. There are two false alarms and two missed diagnoses (lost sensitivity) for combinations with a liquid-line restriction.

Table 2.6: Indicators numbers for the different faults implemented in multiple-simultaneous fault combinations

Fault	Compnv	Condfovl	Evapfovl	Llrestr	Reflow	Refover
Indicator number	1	2	3	4	5	6

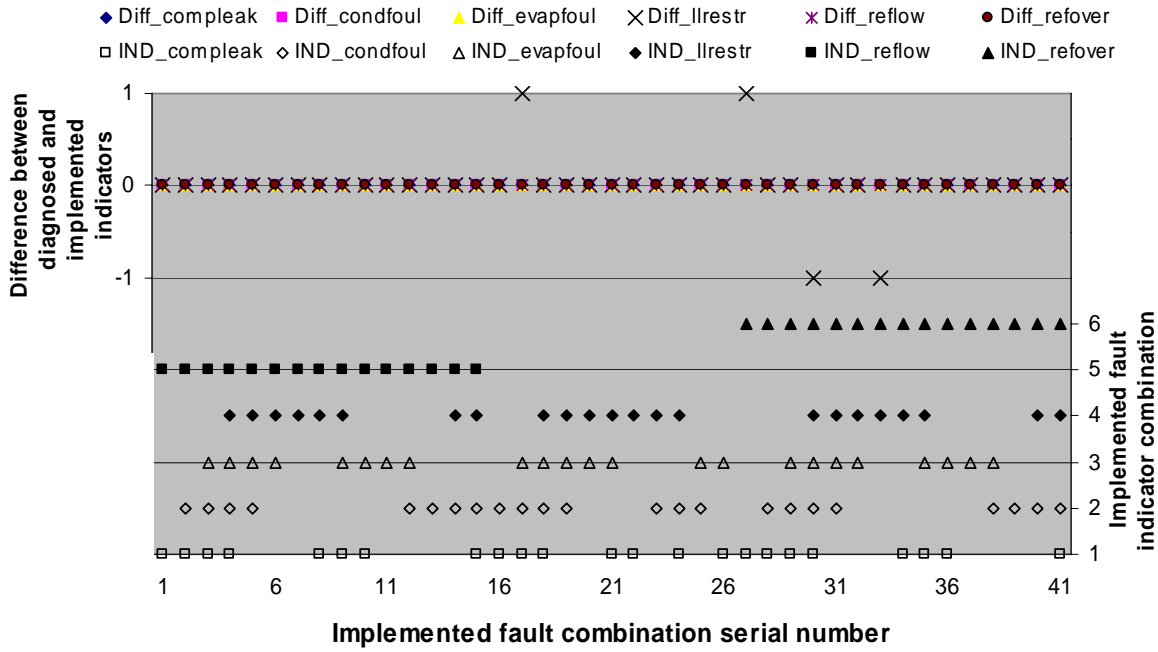


Figure 2.8: Robustness test for multiple-simultaneous-fault FDD

In order to quantify the robustness, an index, a normalized indicator error ρ_i , is defined as,

$$\rho_i = \frac{IND_{i,MSF} - IND_{i,SF}}{\left| IND_{i,SF} - \left| IND_{i,threshold} \right| \right|}.$$

where, i is the individual fault name, $IND_{i,SF}$ is the fault indicator of fault i occurring individually, $IND_{i,MSF}$ is the fault indicator of fault i occurring simultaneously with other faults, $IND_{i,threshold}$ is the FDD threshold of fault i . Table 2.7 summarizes its meanings for different cases.

Table 2.7: Normalized fault indicator error and its meaning

Case	$ \rho_i < 1$	When it is normal		When it is faulty	
		$\rho_i \leq -1$	$\rho_i \geq 1$	$\rho_i \leq -1$	$\rho_i \geq 1$
Recover	OK	False alarm	False alarm	Sensitivity gain	Wrong Diagnosis
Reflow		False alarm	False alarm	Wrong Diagnosis	Sensitivity gain
Other faults		OK	False alarm	Sensitivity loss	Sensitivity gain

Figure 2.9 plots the normalized fault indicator error for compressor leakage. It can be seen that there were no false alarms, sensitivity losses and gains. The normalized fault indicator error is much smaller for faulty operation than normal operation, meaning that the fault indicator has very good robustness against noise and uncertainties and high sensitivity to faults. Especially for faulty operation, the noise and uncertainties are suppressed, meaning that it is less possible to have wrong diagnosis at faulty operation. This confirms the prior theoretical analysis: the compressor valve leakage fault is completely decoupled from all the other faults.

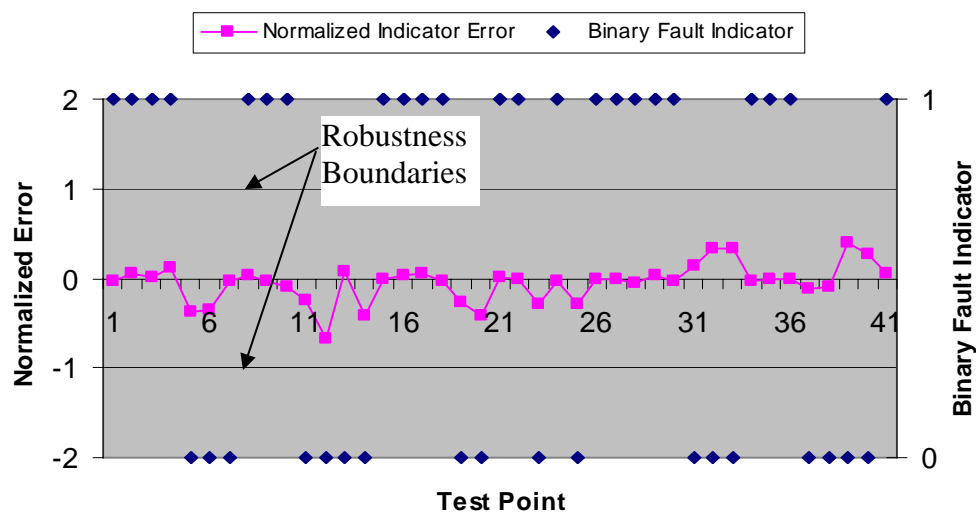


Figure 2.9: FDD Robustness for Compressor Leakage

The normalized fault indicator error for condenser fouling fault is visualized in Figure 2.10. It can be seen that all the points are within the robustness boundaries and there is no obvious difference in robustness between normal operation and faulty operation. Although there were no false alarms and sensitivity losses, robustness was not as good as for compressor valve leakage. There are two factors which affect its robustness: 1) refrigerant mass flow rate estimation and 2) condenser outlet refrigerant enthalpy estimation. It seems that the compressor model and refrigerant mass flow rate correction algorithm have good performance. Theoretical analysis show that if the condenser outlet refrigerant quality is larger than 0.1, the relative error of enthalpy estimation is less than 5%. If the refrigerant charge is more than 50% of the nominal value, the condenser outlet refrigerant quality will not be less than 0.1.

In Figure 2.11, the normalized fault indicator error for evaporator fouling is plotted. It can be seen that there is one point which is out of the range of the robustness boundaries and three points are marginally within the boundaries. However, the point outside the lower boundary does operate normally, so it will not cause any sensitivity loss. Overall, robustness for evaporator fouling was not as good as for compressor leakage and condenser fouling but there were no false alarms and sensitivity losses. There are three factors which affect its robustness: 1) refrigerant mass flow rate estimation, 2) condenser outlet refrigerant enthalpy estimation, and 3) evaporator outlet air enthalpy estimation. Since there is no humidity sensor for evaporator outlet air, its enthalpy is estimated using the by-pass factor method, which adds some additional noise and uncertainty.

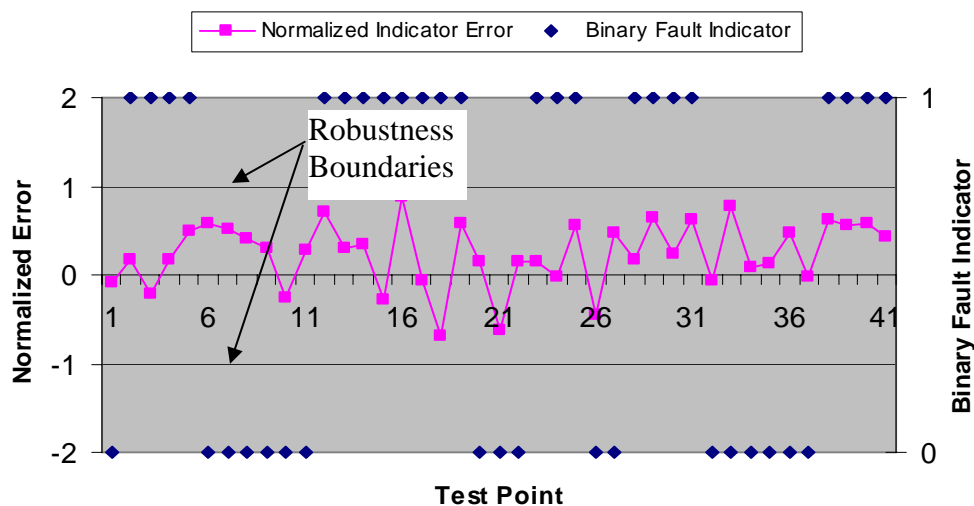


Figure 2.10: FDD Robustness for Condenser Fouling

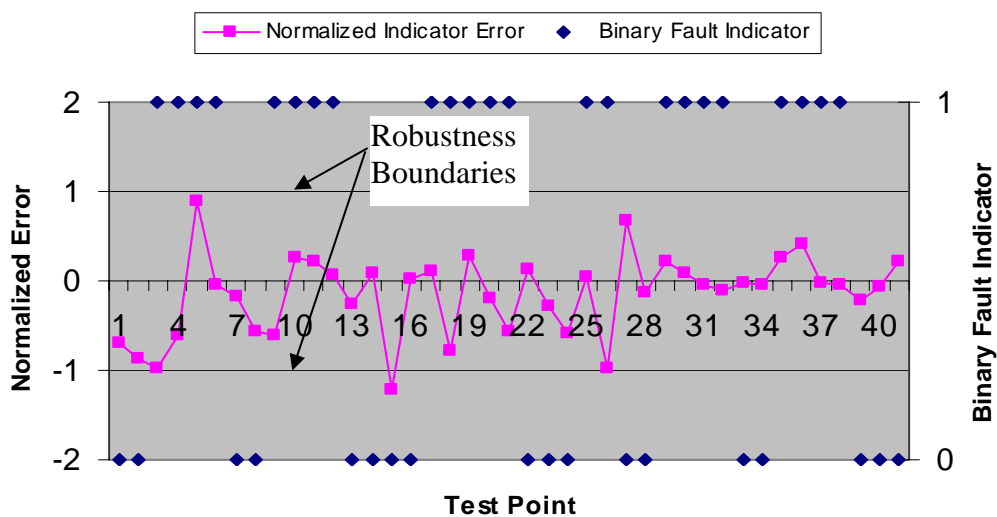


Figure 2.11: FDD Robustness for Evaporator Fouling

The normalized liquid-line restriction fault indicator error is shown in Figure 2.12. It can be seen that there are 6 points which are out of the robustness boundaries. Two of them operating normally are outside of the upper boundary and cause false alarms. Another two operating abnormally are outside of the lower boundary and cause sensitivity losses. The other two of them operating abnormally are outside the upper boundary and cause sensitivity gain. There are three points which are marginally within the boundary.

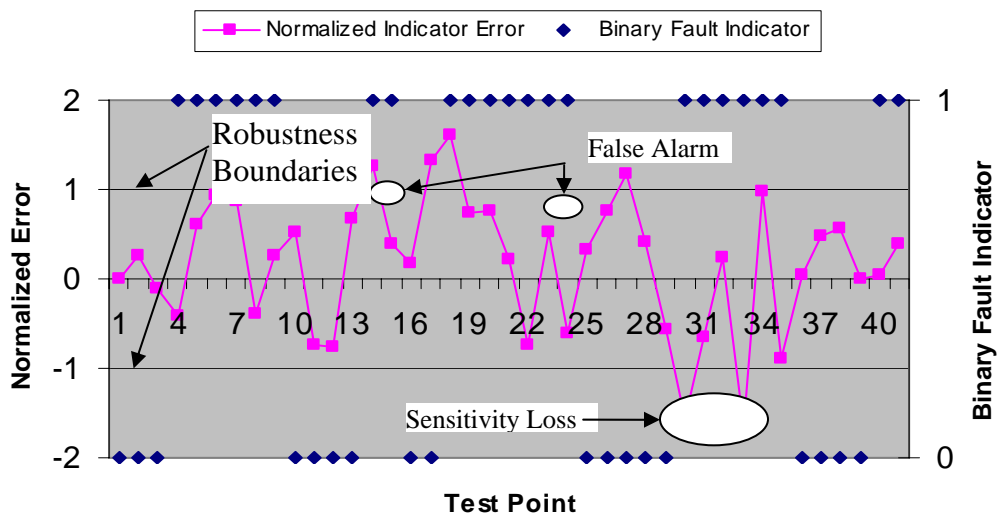


Figure 2.12: FDD Robustness for Liquid-line Restriction

The reason for worse robustness is that more uncertainties are introduced: 1) refrigerant mass flow rate estimation, 2) condenser outlet refrigerant pressure estimation, and 3) estimation

of pressure drop across the TXV. Pressure drop across the TXV is estimated using a TXV model which is pretty sensitive to superheat measurement noise and refrigerant mass flow rate estimation. In addition, when the operation is out of the control range of the TXV, the TXV model will not have good performance. There are two situations where this will occur: 1) when the refrigerant charge is lower than a certain value, the TXV is saturated and will cause abnormally high superheat, and 2) when there is a compressor leakage fault, the evaporating pressure may be high enough to trigger the TXV maximum operation pressure (MOP). In addition to more uncertainties, the pressure drop across the clogged filter/drier itself varies according to refrigerant mass flow rate and refrigerant state even for the same physical fault level.

Since both false alarm and sensitivity loss occur, the idea that the false alarm rate can be reduced by means of raising the diagnosis threshold to reduce some sensitivity can not be entertained. A possible way to reduce the false alarm rate but keep good sensitivity is to use one more pressure sensor in the liquid-line.

The normalized fault indicator error for both refrigerant low charge and over charge is plotted in Figure 2.13. For the refrigerant low charge fault, there are 3 points which are outside of the upper boundary which indicates sensitivity gain, and there were no wrong diagnoses and sensitivity losses. When the refrigerant is normally and over charged, all the test points are within the robustness boundaries and there are no false alarms and sensitivity losses.

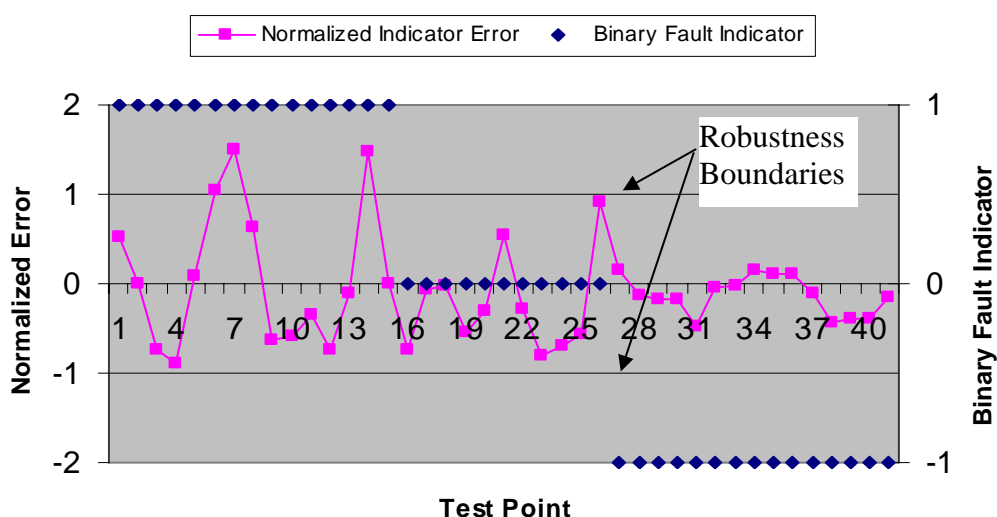


Figure 2.13: FDD Robustness for Refrigerant Charge Faults

In summary, all the individual faults can be identified before they cause 5% of degradation in cooling capacity and EER and SHR and their EPDI reaches 10%. Robustness tests for forty-one multiple-simultaneous-fault combinations showed that that there were only two false alarms and sensitivity losses that occurred for a liquid-line restriction fault.

3 VIRTUAL PRESSURE SENSORS AND TEMPERATURE SENSOR ONLY FDD

3.1 Introduction

Reducing implementation costs is a very important objective at this stage of commercialization for HVAC FDD technology. The decoupling-based FDD technique performs fault diagnostics and performance monitoring using pressures and temperatures. Pressure values are crucial because 1) pressure values are very important to evaluate liquid line subcooling, condensing temperature (CT), evaporating temperature (ET) and suction line superheat and 2) pressure values are critical to predict refrigerant mass flow (\dot{m}_{ref}) and power consumption and thus system performance indices such as EER and capacity (\dot{Q}_{cap}).

However, pressure values are expensive to measure directly. First of all, pressure sensors are far more expensive than temperature sensors, especially for high accuracy ones. Second, pressure measurements are also more expensive than temperature from the data acquisition point of view in that it costs more for the data acquisition equipment to be capable of dealing with pressure sensors. Third, proper installation of pressure sensors in the field is expensive. If the pressure sensors are brazed in place, it would cost several hundred dollars to recover and recharge the system. If, on the other hand, pressure sensors are attached to service ports using fittings, refrigerant leakage will undoubtedly occur at these locations over time.

Consequently, it is desirable to remove the physical pressure sensors and estimate discharge pressure (P_{dis}), condensing pressure (P_{cond}), liquid line pressure (P_{ll}), evaporating pressure (P_{evap}) and suction pressure (P_{suc}) using low-cost temperature sensors. The performance should be robust against variation of driving conditions and all kinds of faults.

Braun and Li (2004a) proposed a technique replacing pressure sensors with two temperature sensors for each coil. In order to reduce implementation costs further, a scheme in which only one temperature sensor is used for each heat exchanger to estimate the pressures was

investigated. Section 3.2 describes development of virtual pressure sensors and section 3.3 describes application of virtual pressure sensors in the temperature sensor only FDD technique.

3.2 Virtual Pressure Sensors

Section 3.2.1 describes where to place the temperature sensor for measuring saturated high-side and low-side pressures and section 3.2.2 presents a simple pressure estimation method based on virtual sensors.

3.2.1 Temperature Sensor Location

3.2.1.1 Physical Analysis

Figure 3.1 illustrates a typical vapor compression system. The system includes four major parts: compressor, condenser, expansion device and evaporator, and lines connecting those parts: discharge line connecting compressor with condenser, liquid line connecting condenser with expansion device and suction line connecting evaporator with compressor.

In a vapor compression refrigeration cycle, refrigerant is compressed by a compressor into highly superheated refrigerant vapor with high pressure; the highly superheated refrigerant vapor is converted into subcooled refrigerant liquid by rejecting heat to the surroundings through a condenser; the subcooled refrigerant liquid is regulated to the low side evaporator and refrigerant exiting the expansion device is typically in two-phase state; this two-phase refrigerant is vaporized and superheated by absorbing heat from its ambient through an evaporator; and the superheated vapor exiting the evaporator enters the compressor for the next cycle.

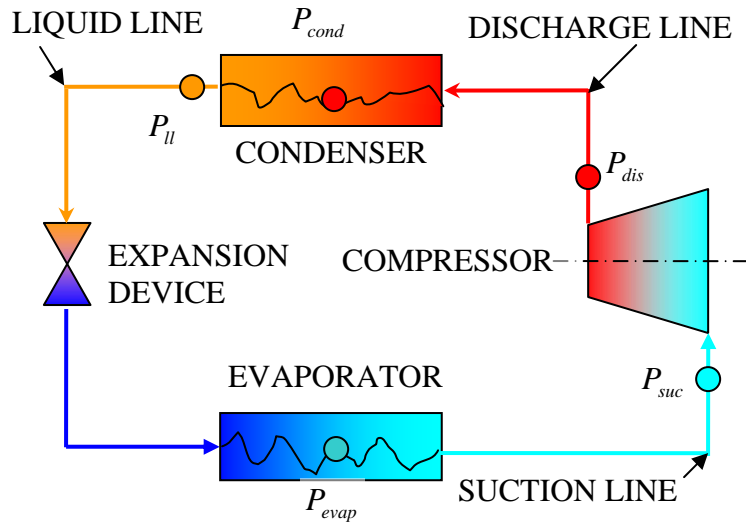


Figure 3.1 Block diagram for a typical vapor compression system

For the low pressure side, it is guaranteed that refrigerant at the inlet of an evaporator is a two-phase mixture. For the high side, the superheated refrigerant vapor first cools down to saturated vapor, then the saturated vapor undergoes a phase change from saturated vapor to saturated liquid, and finally the saturated liquid is further subcooled. So there will always be a portion of the condenser where the refrigerant is a two-phase mixture and the key is to identify the location where the refrigerant condition is always two-phase, regardless of the operating conditions and faults that are present.

Figure 3.2 illustrates the heat transfer in the condenser de-superheat section. The thermal fluid model for the condenser de-superheat section at steady state can be derived as follows:

$$\begin{aligned}
 -\dot{m}_{ref} C_{ref} dT_{ref,x} &= U_i \pi D_i (T_{ref,x} - T_{air,inlet,x}) dx \\
 T_{ref,x} - T_{air,inlet,x} &= (T_{ref,inlet} - T_{air,inlet,0}) \exp\left(\frac{-U_i \pi D_i}{\dot{m}_{ref} C_{ref}} x\right) \\
 T_{ref,x} - T_{cond} &= (T_{ref,inlet} - T_{cond} + T_{cond} - T_{air,inlet,0}) \exp\left(\frac{-U_i \pi D_i}{\dot{m}_{ref} C_{ref}} x\right) - (T_{cond} - T_{air,inlet,x}) \\
 T_{sh,x} &= (T_{sh,inlet} + T_{cond} - T_{air,inlet,0}) \exp\left(\frac{-U_i \pi D_i}{\dot{m}_{ref} C_{ref}} x\right) - (T_{cond} - T_{air,inlet,x}) \quad (3.1)
 \end{aligned}$$

where $T_{ref,x}$ is the refrigerant temperature at location x ; $T_{air,inlet,x}$ is the inlet air temperature at location x ; $T_{ref,inlet}$ is the inlet refrigerant temperature; T_{cond} is the condensing temperature; U_i is

the overall heat transfer coefficient based on inner surface area; \dot{m}_{ref} is the refrigerant mass flow rate; C_{ref} is the refrigerant thermal capacitance; D_i is the inner diameter of the tube.

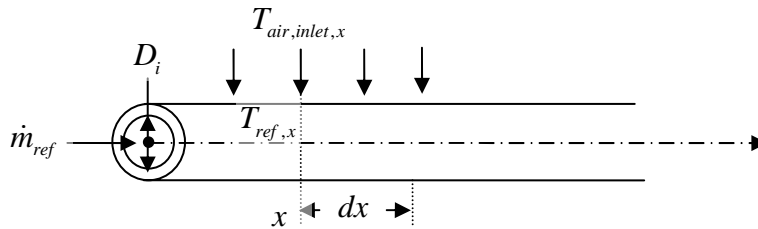


Figure 3.2 Heat transfer in the condenser de-superheat section

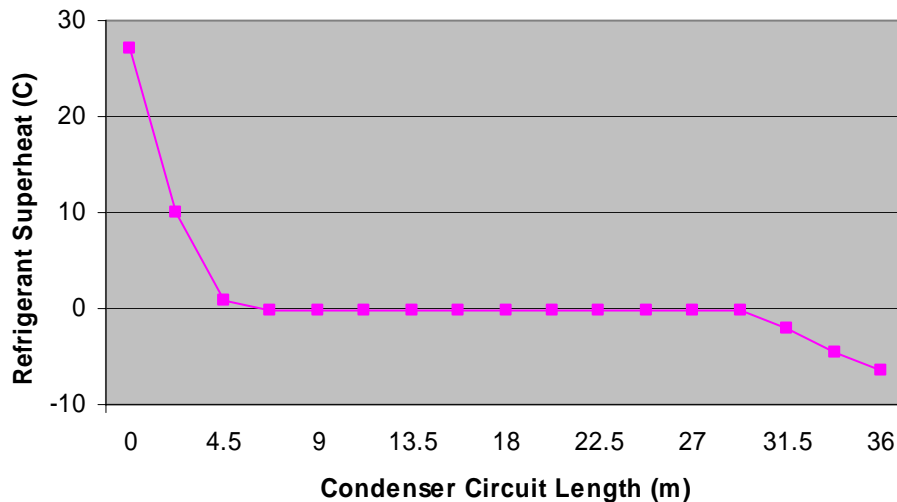


Figure 3.3 Simulation of the refrigerant superheat profile across the condenser

As equation (3.1) shows, the refrigerant temperature in the single-phase flow de-superheating section decreases exponentially. Figure 3.3 plots a typical refrigerant superheat profile across the condenser of a 3-ton air conditioner, which was simulated using ACModel. It can be seen from Figure 3.3 that refrigerant superheat decreases drastically to zero after the first two passes which is around 4.5 meter in length and it takes about another 11 passes for the saturated refrigerant vapor to become saturated refrigerant liquid and finally takes about additional three passes for the saturated refrigerant liquid to obtain some subcooling.

For residential and light commercial application, the condenser de-superheat and two-phase sections are typically designed such that each coil circuit accommodates about 1~1.5 ton

cooling capacity. According to similarity principle, the superheat profile illustrated in Figure 3.3 can be generalized to residential and light commercial air conditioners: it typically takes about four meters (about two passes or 10~15% of one circuit length) for superheated refrigerant vapor to become saturated. Since the saturated section is designed to accommodate about 75% of the total heat rejection, the saturated section accounts for about 60% of a circuit length. So a temperature sensor can be placed after four meters and before 30 meters of condenser tube length.

In summary, the evaporator inlet is guaranteed to be a saturated location and a position between 4 and 30 meters of tube length from the condenser inlet is mostly likely to be a saturated section.

3.2.1.2 Experimental Validation

Extensive laboratorial testing data (96 sets) were collected from systems with 1) different structures -- packaged and split, 2) different expansion devices -- TXV and fixed orifice, and under various driving conditions – 3) various ambient temperatures, 4) various indoor return air temperature and humidity bins, 5) various air flow rates for both heat exchangers, and 6) various refrigerant charge levels.

Appendix 1 plots all the refrigerant temperature profile in the condenser and evaporator of a split TXV system. In summary, among all the factors considered in the testing, only charge has significant impact on condenser local refrigerant temperature distribution. When the system is charged at its nominal level, it takes about two passes (4.5 m) for the high superheated refrigerant to become saturated and about another nine passes to begin to gain subcooling (see Figure 3.4). When charge is extremely low (about 50%), refrigerant is saturated at the third tube bend (7.75m) and there is no noticeable subcooling section (see Figure 3.5). When charge is extremely high (about 150%), refrigerant is saturated at the first tube bend (2.25m) and subcooled at the fifth tube bend (9m) (see Figure 3.6). In other cases, refrigerant is saturated around the second tube bend and subcooled around the twelfth tube bend. So the third and fourth tube bends are guaranteed to be saturated locations.

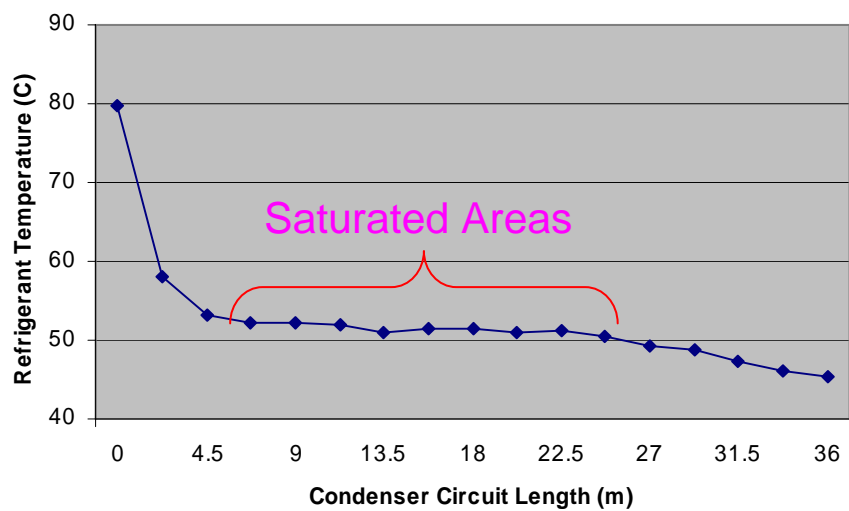


Figure 3.4 Refrigerant superheat profile across the condenser under nominal charge (for a split TXV system)

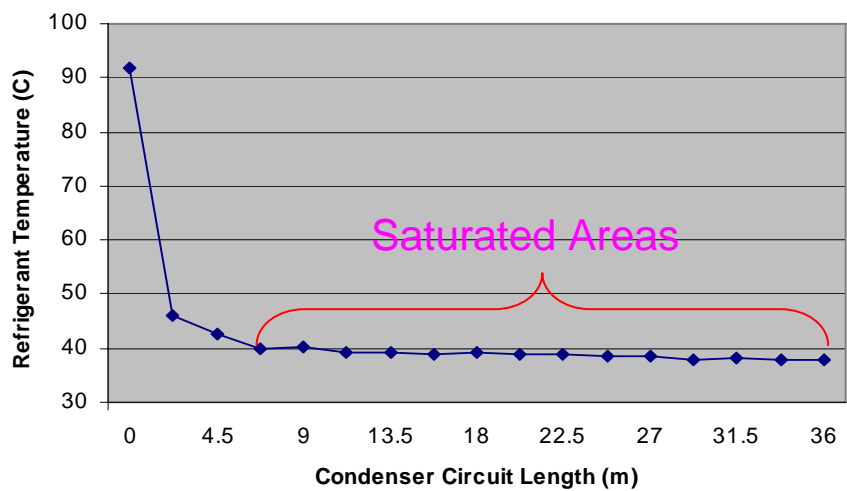


Figure 3.5 Refrigerant superheat profile across the condenser under 50% of nominal charge (for a split TXV system)

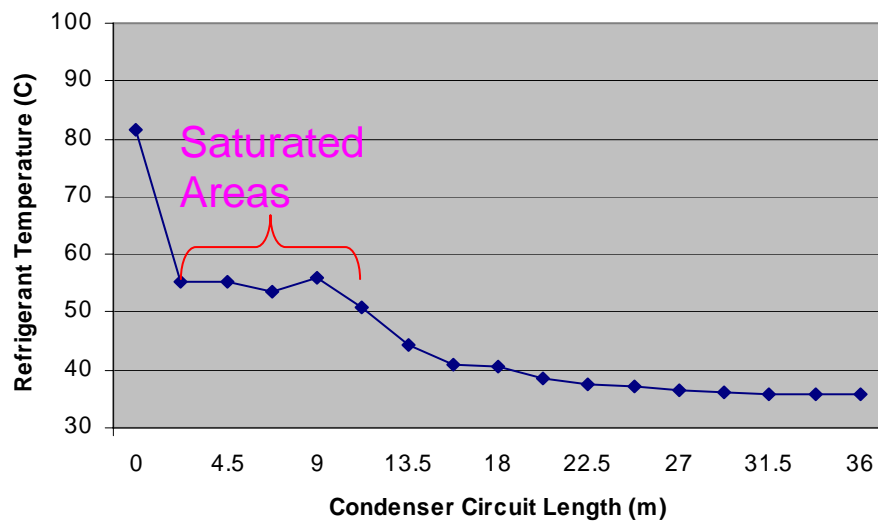


Figure 3.6 Refrigerant superheat profile across the condenser under 150% of nominal charge (for a split TXV system)

For the low side, all the experimental testing data ($\geq 50\%$ charge) show that the inlet of the evaporator is guaranteed to be a saturated location without any exception (see Figures 3.7, 3.8 and 3.9). So the inlet of evaporator is guaranteed to be a saturated location. Typically, when the system charge is normal and the evaporator is clean, 70 percent of the evaporator volume is saturated. However, when the system is at a very low charge level, the evaporator can be superheated after the first pass.

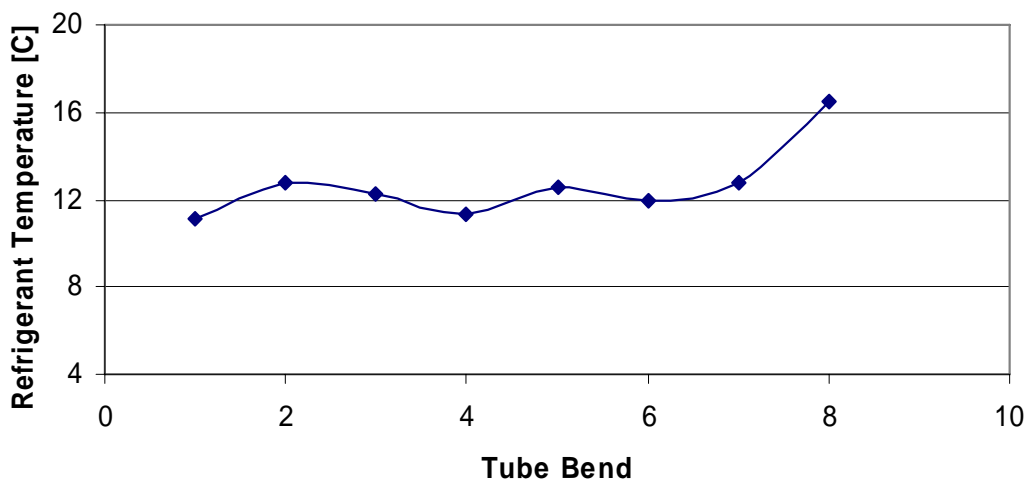


Figure 3.7 Refrigerant superheat profile across the evaporator under nominal charge (for a split TXV system)

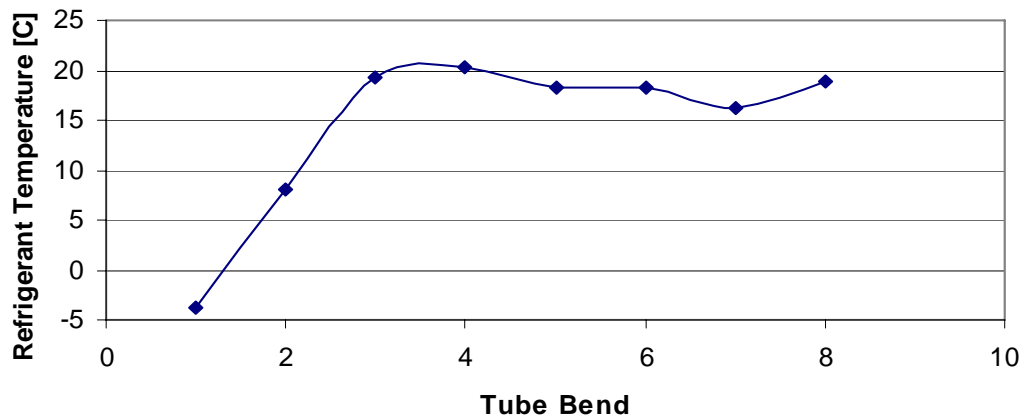


Figure 3.8 Refrigerant superheat profile across the evaporator under 50% of nominal charge (for a split TXV system)

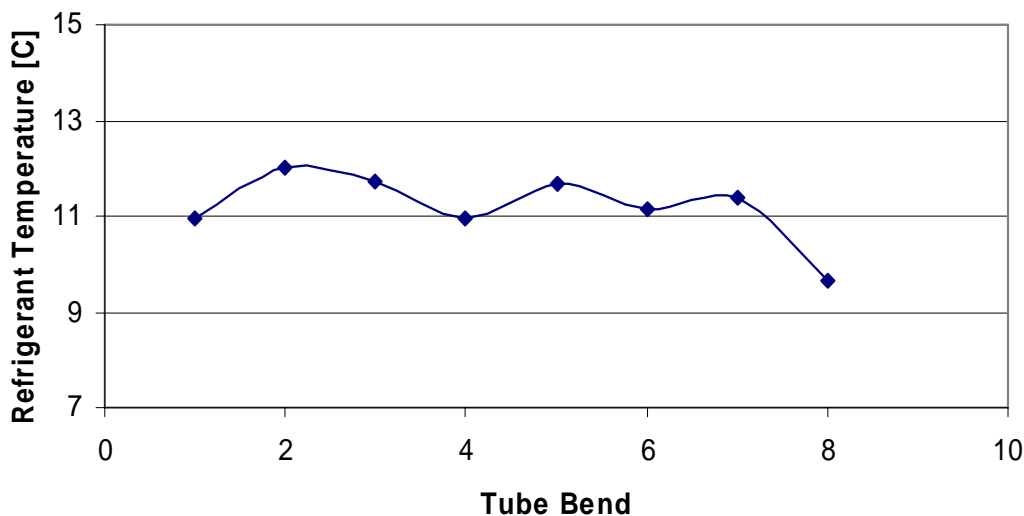


Figure 3.9 Refrigerant superheat profile across the evaporator under 150% of nominal charge (for a split TXV system)

3.2.2 Pressure Estimation Method

Previously, Braun and Li (2004a) proposed a technique using two additional temperature sensors -- one for each coil -- to estimate the target pressure drop. In order to further reduce the implementation costs, the two additional temperature sensors are eliminated and a simplified

pressure drop estimation method is investigated. For residential and light commercial air conditioning application, pressure drop across the high side components (condenser and discharge line) ranges from 15 to 30 psi and pressure drop across the low side components (evaporator and suction line) is about 4 psi.

There are three types of condenser structures. As illustrated in Figure 3.10, a type I condenser has several independent parallel circuits with a number of passes each and then combines at the outlet of the condenser which is the inlet of liquid line. A type I condenser is widely used in heat pumps and occasionally used in small packaged air conditioners.

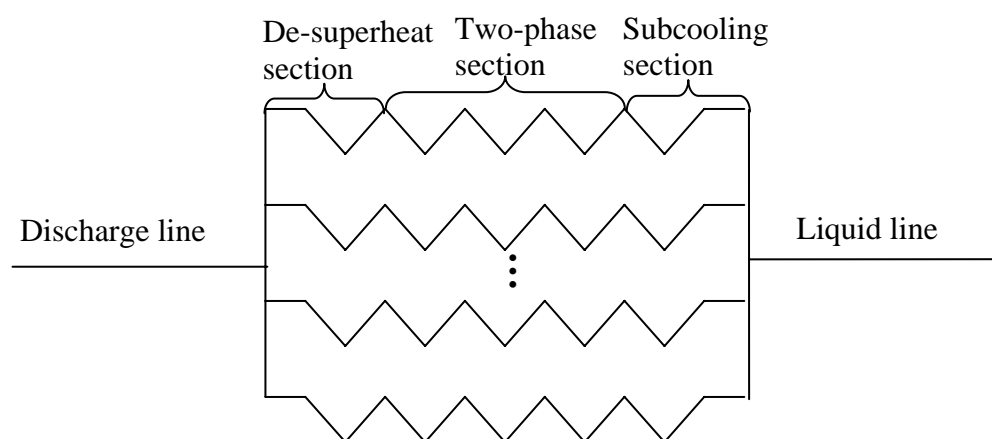


Figure 3.10 Type I condenser structure

Similar to the type I condenser (see Figure 3.11), a type II condenser has several parallel circuits with a number of passes each that then combine and make several more passes before interfacing with the liquid line. Type II condensers are most widely used in air conditioners.

As shown in Figure 3.12, a type III condenser begins with several parallel circuits with a number of passes each that then combine into a fewer number of circuits for a number of passes each that then combine into one circuit for more passes before interfacing with the liquid line. Type III condensers are found in old air conditioners but seldom found in modern air conditioners and heat pumps.

It can be seen that all three condenser types have the same structure for the beginning part – a de-superheat section. Typically, each circuit of the de-superheat section is designed to accommodate around 1~1.5 ton cooling capacity, so the pressure drop across the discharge line and the condenser de-superheat section is expected to be a constant for all the three types of condensers if the driving conditions are the same.

According to simulation by ACModel, the pressure drop across the discharge line and the condenser de-superheat section for type I and type II condensers is about 10 psi (see Figures 3.13 and 3.14). Since different type condensers have different structures for the two-phase sections and subcooling sections, the pressure drop across the two-phase and subcooling sections depends on the condenser structure. As shown in Figures 3.13 and 3.14, the pressure drop across the two-phase and subcooling sections for a type I condenser is about 5 psi and is about 10 psi for a type II condenser. For type III condensers, it can be up to 20 psi. Table 3.1 summarizes typical pressure drop values across different condenser sections for different type condensers. Although the absolute pressure drop values may vary a little due to different refrigerants and different manufacturers, according to similarity principle, the percentage values would be general. The percentage values are put in parentheses in Table 3.1 as well. If the nominal total pressure drop is known, pressure drops across different sections can be calculated.

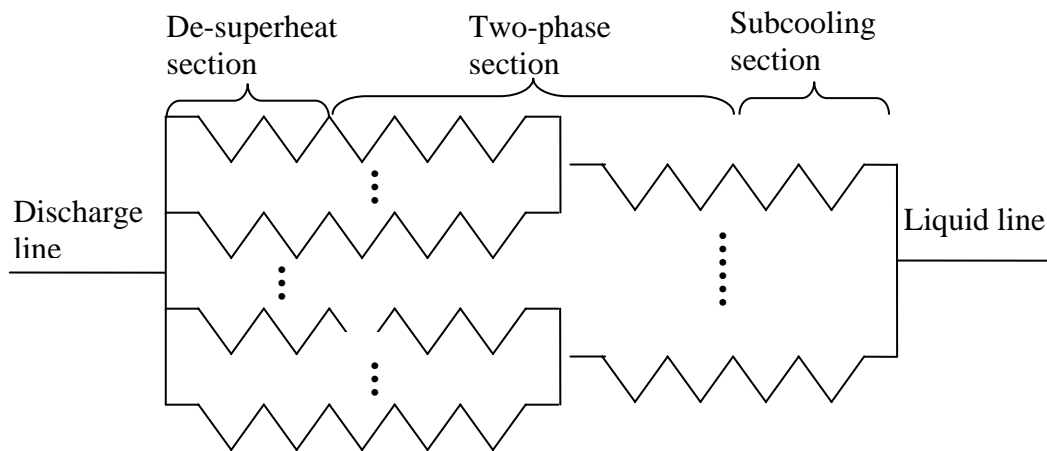


Figure 3.11 Type II condenser structure

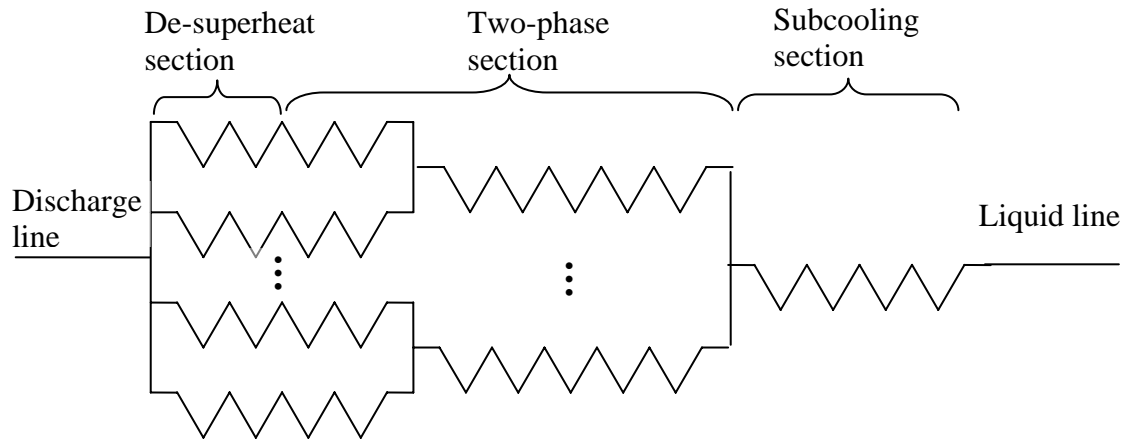


Figure 3.12 Type III condenser structure

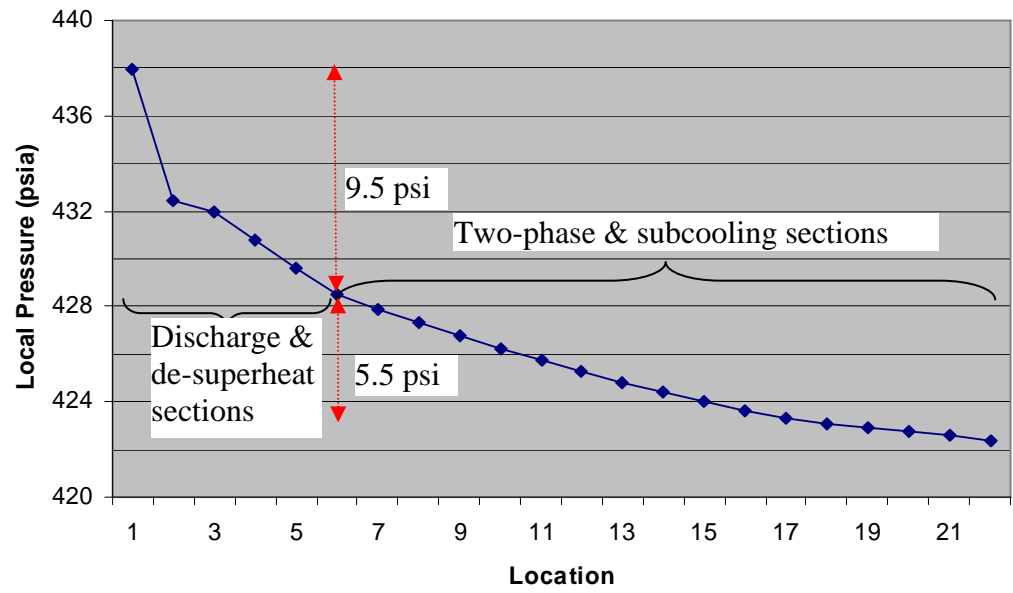


Figure 3.13 Refrigerant local pressure profile across a type I condenser (with R410a)

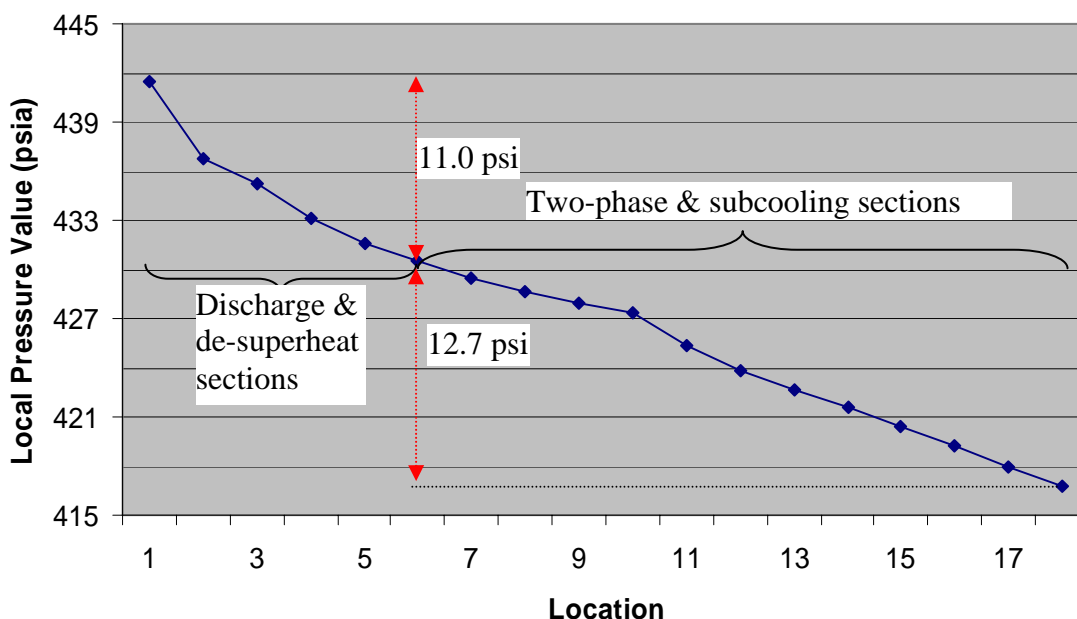


Figure 3.14 Refrigerant local pressure profile across a type II condenser (with R410a)

Table 3.1 Typical pressure drop value across different condenser sections

Condenser type	Default pressure drop (psi)	Discharge line and de-superheat section	Two-phase and subcooling sections
Type I	15	10 (67%)	5 (33%)
Type II	20	10 (50%)	10 (50%)
Type III	30	10 (33%)	20 (67%)

Experimental data collected from a 3-ton packaged air conditioner with R410a as the refrigerant and a type I condenser was used to validate these results. Temperature sensors were placed at the condenser coil return bends and real pressure sensors are used to measure discharge line and liquid line pressures. The temperature measured at the fourth return bend was used to calculate the saturated pressure. Figure 3.15 plots the discharge line pressure and liquid line pressure vs. virtual condensing pressure. It can be seen that the virtual condensing pressure consistently resides between the liquid line pressure and discharge line pressure.

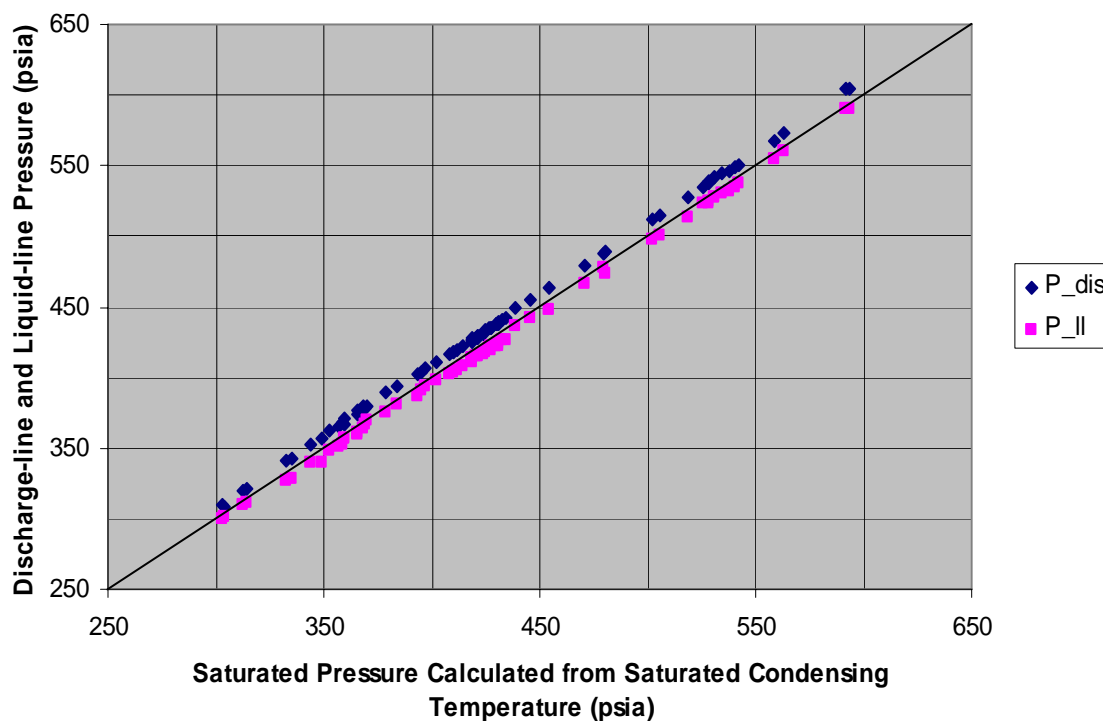


Figure 3.15 Discharge-line and liquid-line pressures vs. virtual condensing pressure calculated from surface temperature at 4th return bend (Packaged AC with R410a)

Table 3.2 summarizes the pressure drops across different sections for this unit. The pressure drop across the discharge line and condenser de-superheat section ranges from 5.1 psi to 11.9 psi with a mean value of 8.7 psi; the pressure drop across two-phase and condenser subcooling sections ranges from 0.3 psi to 8.7 psi with a mean value of 5.0 psi. Data collected under very low (50% of nominal charge) or very high (150% of nominal charge) charge levels cause the pressure drop extremes. When charge is very low, refrigerant mass flow rate is very low (can be half of the nominal value), pressure drop can be very small; when the charge is very high, subcooling will occupy the two-phase section and thus pressure drop across two-phase and subcooling sections can be very large. If 10 psi is assumed for the discharge line and de-superheat sections and 5 psi for two-phase and subcooling sections, the resulting maximum error is ± 4.9 psi for the discharge line and de-superheat sections and ± 4.7 psi for two-phase and subcooling sections (see Table 3.2).

Table 3.2 Pressure drop across the condenser sections and evaporator

	Pressure drops across condenser sections	Pressure drop
--	--	---------------

	Discharge line and de-superheat section (psi)	Two-phase and subcooling sections (psi)	Total (psi)	across evaporator (psi)
Min	5.1	0.3	7.1	1.8
Mean	8.7	5.0	14.0	3.5
Max	11.9	8.7	17.4	5.2
Error	± 4.9	± 4.7	± 7.9	± 2.2

Evaporator structures are simple, with several parallel circuits and no combinations. The pressure drop across an evaporator is typically around 4 psi. For the test systems, temperature sensors were placed at the evaporator coil return bends and real pressure sensors were used to measure suction line pressure. The temperature measured at the evaporator inlet is used to calculate the virtual saturated pressure. Figure 3.16 plots the suction line pressure vs. virtual saturated evaporating pressure. It can be seen that the suction line pressure consistently resides below the calculated saturated evaporating pressure. Table 3.2 tabulates the pressure drop across evaporator. The pressure drop across evaporator ranges from 1.8 psi to 5.2 psi with a mean value of 3.5. If a 4 psi pressure drop is assumed, the resulting maximum error would be ± 2.2 psi.

In summary, Errors resulting from virtual pressure sensors are comparable to the real pressure sensor accuracy with original manufacturer's calibration. Therefore, a method that uses one temperature sensor for each heat exchanger coil and assumes constant pressure drops has reasonably good accuracy. Table 3.1 can be used as a guideline for determining the pressure drops. If there is more information about the total pressure drop across the condenser, the pressure drop estimation can be modified using the percentage values in Table 3.1.

The following section evaluates the overall impact of virtual pressure sensors on the decoupling-based FDD technique performance.

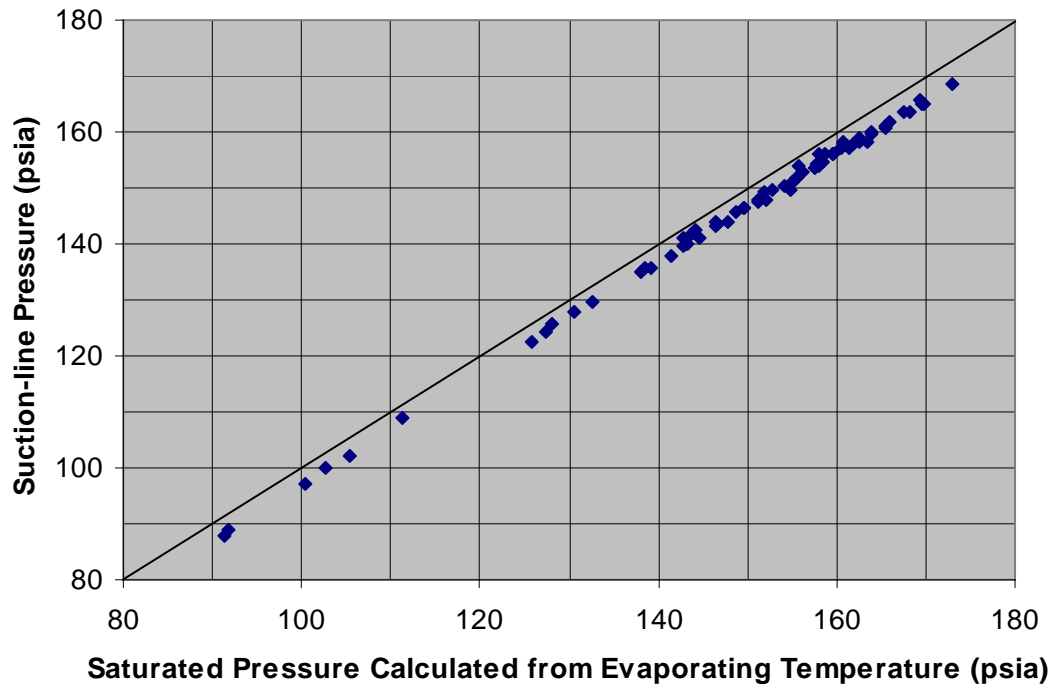


Figure 3.16 Suction-line pressure vs. saturated pressures calculated from surface temperature at the inlet of evaporator

3.3 Temperature Sensor Only FDD

Section 3.3.1 evaluates the uncertainties caused by virtual pressure sensors and section 3.3.2 applies the virtual sensors to decoupling-based FDD.

3.3.1 Uncertainty Analysis

In many cases, an important quantity is not directly measured but rather calculated as a function of one or more variables that are directly measured, i.e., $Y = f(X_1, X_2, \dots)$. The measured variables, X_1 , X_2 , etc. have a random variability which is referred to as its uncertainty. The uncertainties in each of the measured variables can propagate into the value of the calculated quantity, Y . The method for determining this uncertainty propagation is described in NIST Technical Note 1297 (Taylor B.N. and Kuyatt, C.E., Guidelines for Evaluating and Expressing the Uncertainty of NIST Measurement Results, National Institute of Standards and Technology Technical Note 1297, 1994). Assuming the individual measurements are uncorrelated and random, the uncertainty in the calculated quantity can be determined as

$$U_Y = \sqrt{\sum_i \left(\frac{\partial Y}{\partial X_i} \right)^2 U_{X_i}^2}$$

where U represents the uncertainty of the variable.

To perform the uncertainty analysis, the following assumptions for uncertainty of measured variables and constants were made: 1) the location for measuring saturated temperature is robust; 2) temperature sensor's accuracy is ± 1 °F; 3) pressure drop estimation accuracies are ± 4.9 psi for the discharge line and de-superheat sections, 4) ± 4.7 psi for two-phase and subcooling section pressure drops, and 5) ± 2.2 psi for the evaporator and suction line pressure drops. Under typical driving conditions (condenser inlet air dry bulb temperature = 95.2 F, evaporator inlet air dry bulb temperature = 80.1 F, and evaporator inlet air relative humidity = 50.6%), uncertainties for calculated variables are summarized in Table 3.3. From Table 3.3, it can be seen that accuracies in the calculated variables are reasonably good and uncertainties in the fault indicators are within the diagnosis threshold.

Table 3.3 Calculated variables and uncertainties

Calculated Variables	Value
----------------------	-------

Discharge line pressure (psia)	439.7 \pm 7.717
Liquid line pressure (psia)	424.7 \pm 7.592
Suction line pressure (psia)	155.7 \pm 3.409
Liquid line subcooling (F)	13.42 \pm 1.383
Suction line superheat (F)	12.47 \pm 1.335
Mass flow rate (g/s)	66.09 \pm 1.978
Power Consumption (W)	2761 \pm 51.48
EER	11.04 \pm 0.363
Compressor fault indicator	0.032 \pm 0.117
Condenser fouling indicator	-0.003 \pm 0.073
Evaporator fouling indicator	-0.167 \pm 0.074
Refrigerant charge fault indicator	-0.057 \pm 0.069

3.3.2 Experimental Validation

Data collected from three systems were used to validate the whole temperature sensor only technique. The system I is a packaged air conditioner with R410a as the refrigerant, a fixed orifice as the expansion device and a scroll compressor. The system II is a split air conditioner with R410a as the refrigerant, a fixed orifice as the expansion device and a reciprocal compressor. The system III is a split air conditioner with R410a as the refrigerant, a TXV as the expansion device and a reciprocal compressor.

3.3.2.1 System I -- Packaged fixed orifice air conditioners

Figures 3.17, 3.18 and 3.19 plot virtual suction line pressure vs. measured suction line pressure, virtual liquid line pressure vs. measured liquid line pressure, and virtual discharge line pressure vs. measured discharge line pressure, respectively. Figures 3.20 and 3.21 plot liquid line subcooling using virtual pressure sensor vs. liquid line subcooling using real pressure sensor and suction line superheat using virtual pressure sensor vs. suction line superheat using real pressure sensor, respectively. Figures 3.22 and 3.23 plot refrigerant mass flow rate using virtual pressure sensor vs. refrigerant mass flow rate using real pressure sensor and compressor power consumption using virtual pressure sensor vs. compressor power consumption using real pressure sensor. Table 3.3 summarizes detailed errors. It can be seen that all the calculated variables have very good accuracy.

Table 3.3 Calculated variables and uncertainties when using virtual pressure sensors

Calculated Variables	Error		
	Min	Median	Max
Suction line pressure (psia)	-1.2	0.5	2.2
Liquid line pressure (psia)	-3.7	-0.3	3.7
Discharge line pressure (psia)	-4.9	-1.5	1.9
Liquid line subcooling (F)	-0.79	-0.06	0.61
Suction line superheat (F)	-0.93	-0.20	0.45
Mass flow rate (%)	-1.0%	0.5%	2.1%
Power Consumption (%)	-1.5%	-0.4%	0.4%

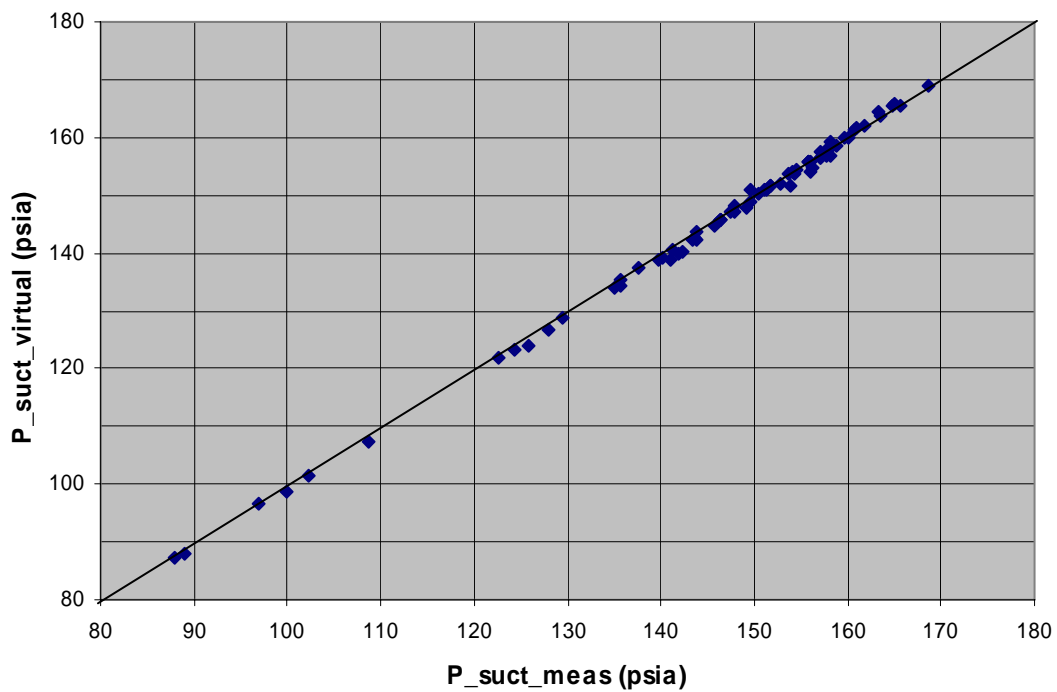


Figure 3.17 Virtual suction-line pressure vs. measured suction-line pressure

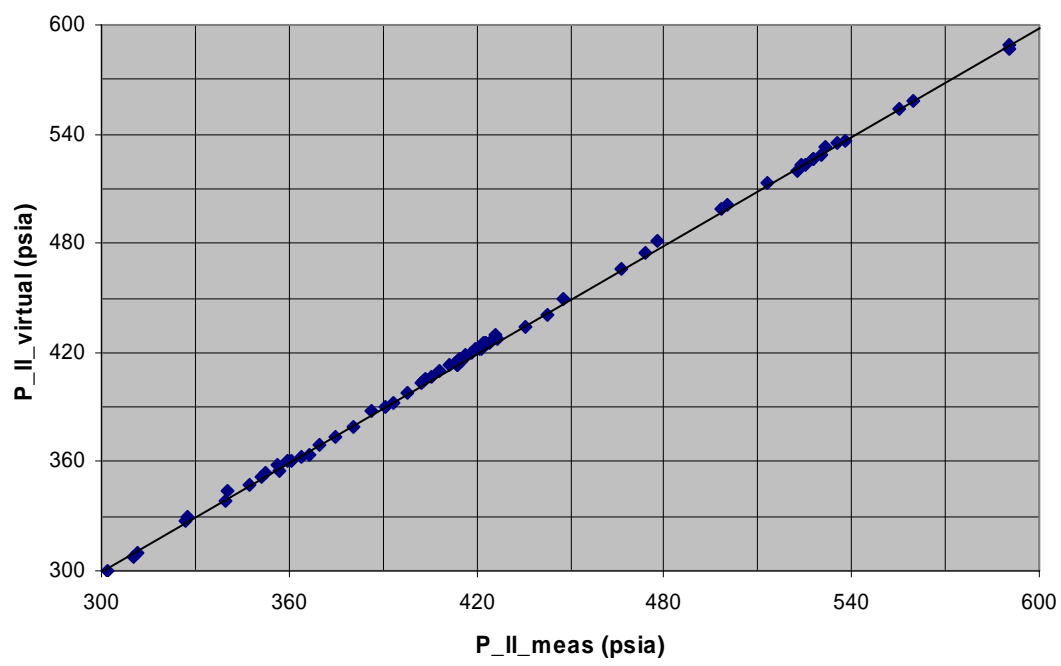


Figure 3.18 Virtual liquid-line pressure vs. measured liquid-line pressure

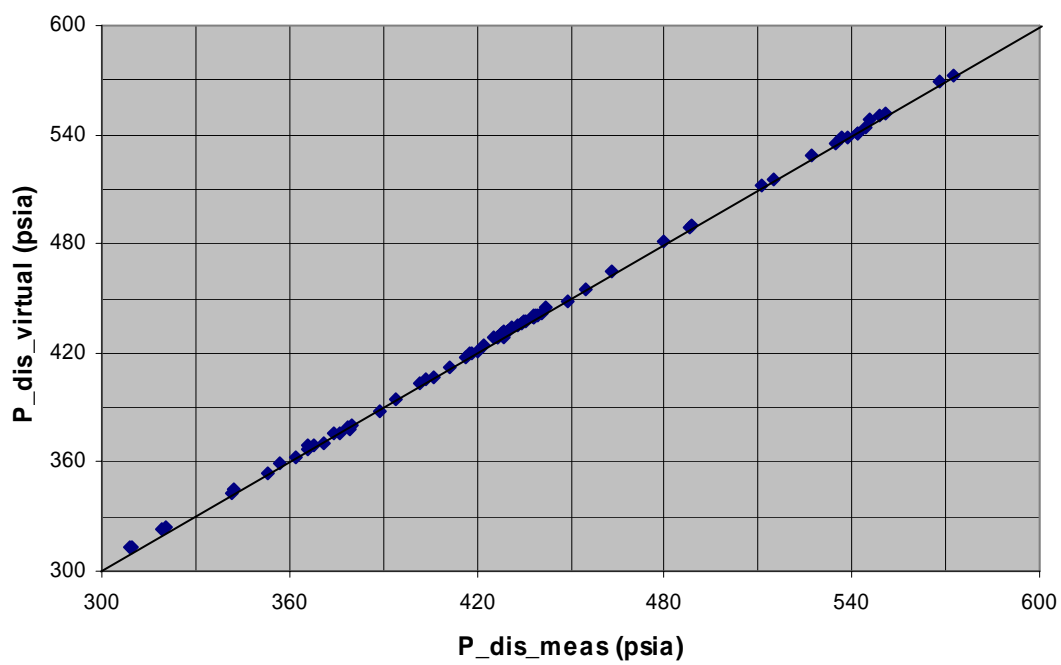


Figure 3.19 Virtual discharge-line pressure vs. measured discharge-line pressure

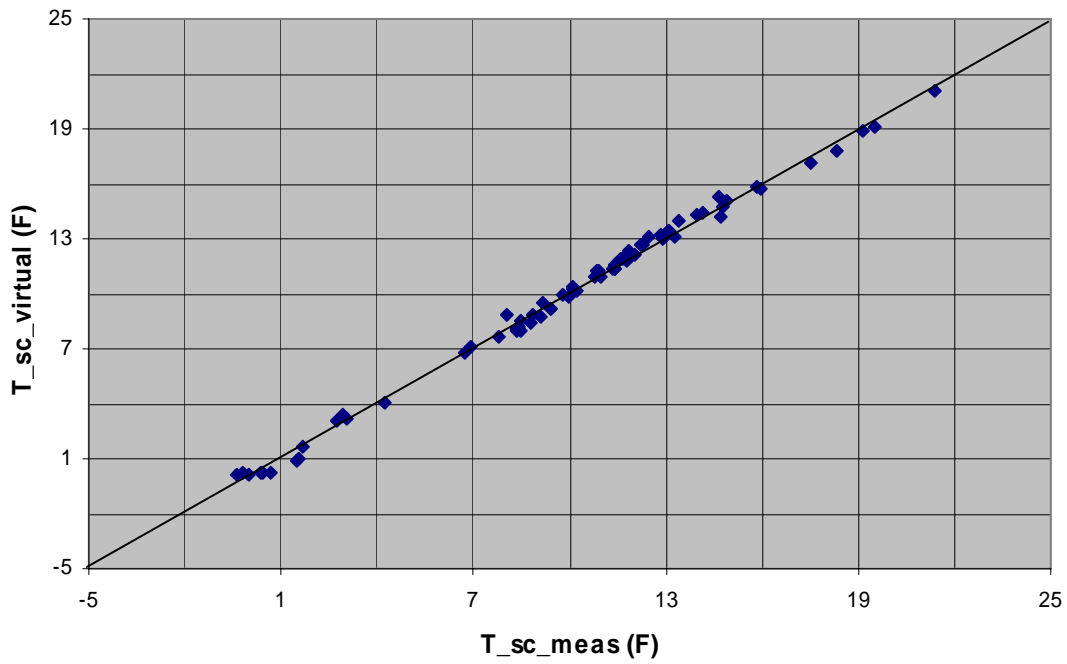


Figure 3.20 Liquid-line subcooling using virtual pressures vs. liquid-line subcooling using measured pressure

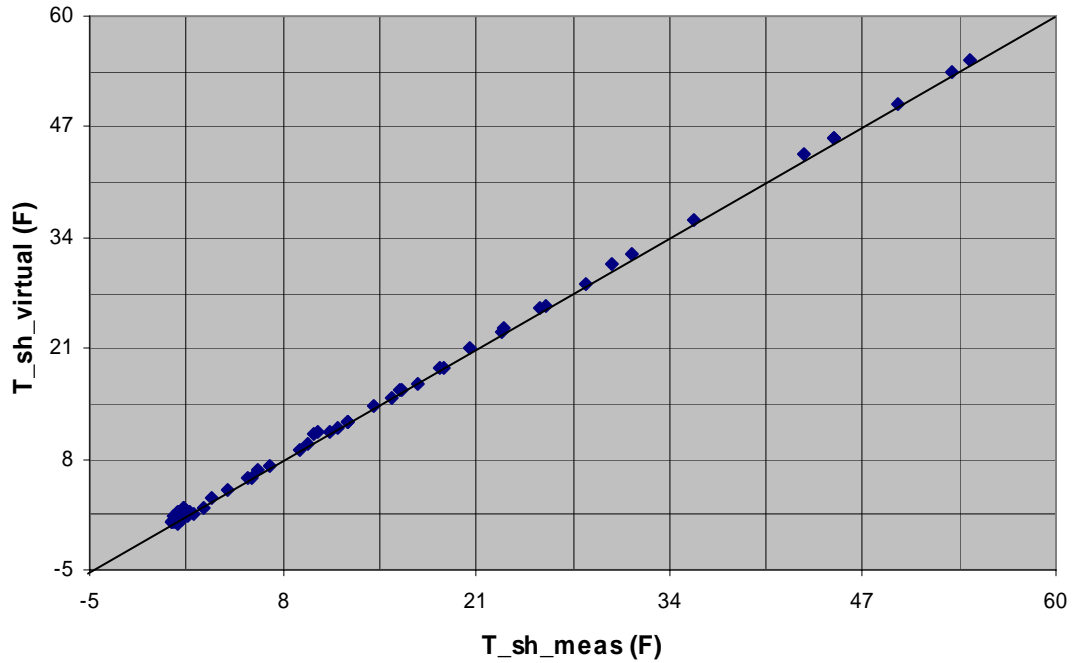


Figure 3.21 Suction-line superheat using virtual pressure vs. suction-line superheat using measured pressures

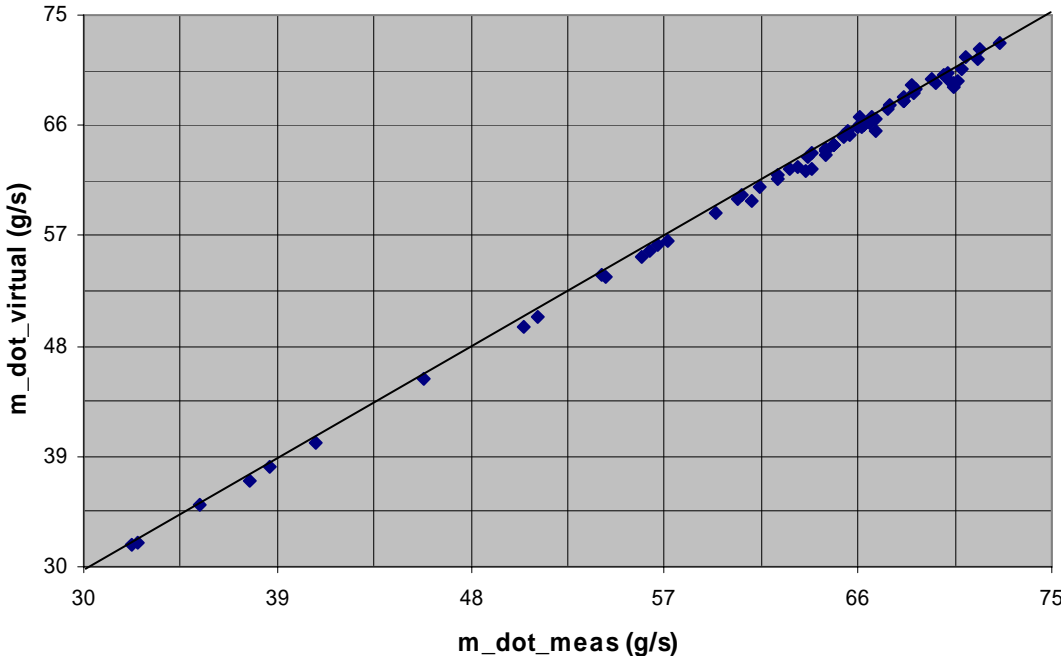


Figure 3.22 Refrigerant mass flow rate using virtual pressure vs. refrigerant mass flow rate using measured pressure

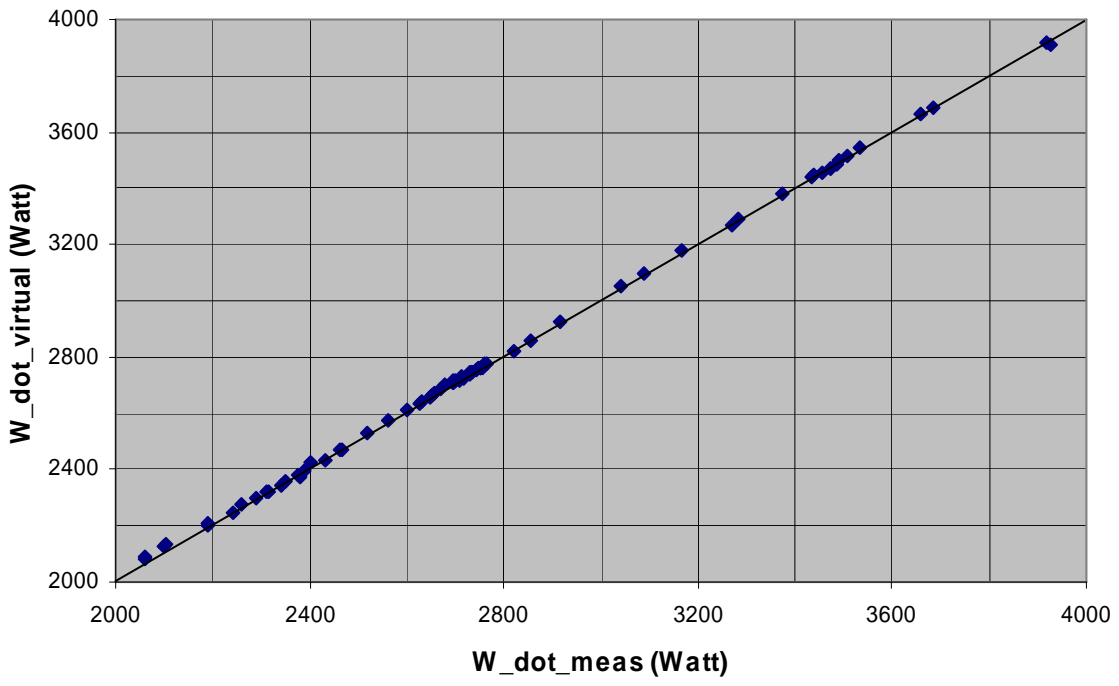


Figure 3.23 Compressor power consumption using virtual pressure vs. compressor power consumption using measured pressure

To demonstrate the impact of virtual pressure sensors on diagnosis, Figures 3.24, 3.25, 3.26 and 3.27 plot fault indicators obtained using virtual pressure sensors vs. those obtained using real pressure sensors. In Figure 3.24, there are three regions: region I –inside of the box, which is the normal operation area, region II – right of the box, where points indicate compressor leakage, and region III – left of the box, where points indicate there is significant heat loss or there is liquid refrigerant entering the compressor. Since a compressor leakage fault was not introduced in testing, most of points reside inside the box. Some points reside in the left side of the green box. This is because there is liquid refrigerant entering the compressor, which was confirmed by the suction line superheat values. It can be seen that compressor leakage fault indicators using virtual pressure sensors agrees with those obtained using real pressure sensors very well and there is no FDD decision difference between using real pressure sensors and using virtual pressure sensors.

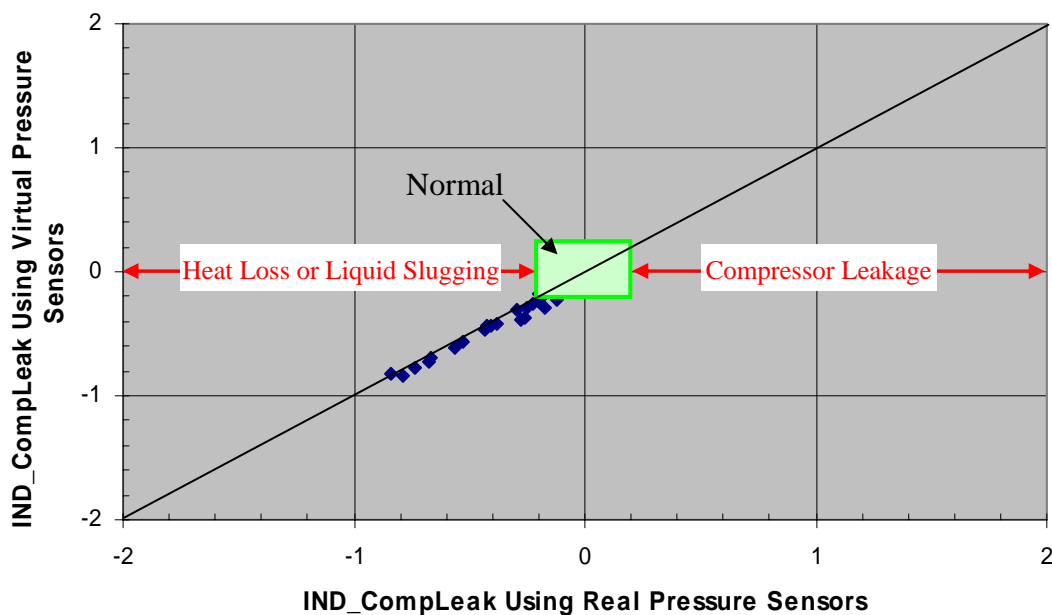


Figure 3.24 Compressor leakage indicator determined using virtual pressure vs. compressor leakage indicator determined using measured pressure

Figure 3.25 plots condenser fouling fault indicators obtained using virtual pressure sensors vs. those obtained using real pressure sensors. Similar to Figure 3.24, there are three regions: region I – inside of the box, which is the normal operation area, region II – right of green box, where points indicate high condenser air CFM, and region III – left of the box, where points indicate low condenser air CFM or fouling. Since a condenser fouling fault is not

introduced in testing, most of points reside inside the green box. Four points reside to the left of the box, which indicates four false alarms. By checking the data, it was found that all these four false alarms occurred when the system was under extremely high charge levels. When the system is under extremely high charge levels, superfluous charge resides in the condenser and less condenser area participates in two-phase heat transfer. Consequently, the heat transfer distribution is significantly changed and air side temperature measurements can not accurately reflect the real heat transfer distribution. However, this situation does not occur for a split system with a type II condenser. It can be seen that condenser fouling fault indicators determined using virtual pressure sensors agree with those for real pressure sensors very well and there is no FDD decision difference between using real pressure sensors and using virtual pressure sensors.

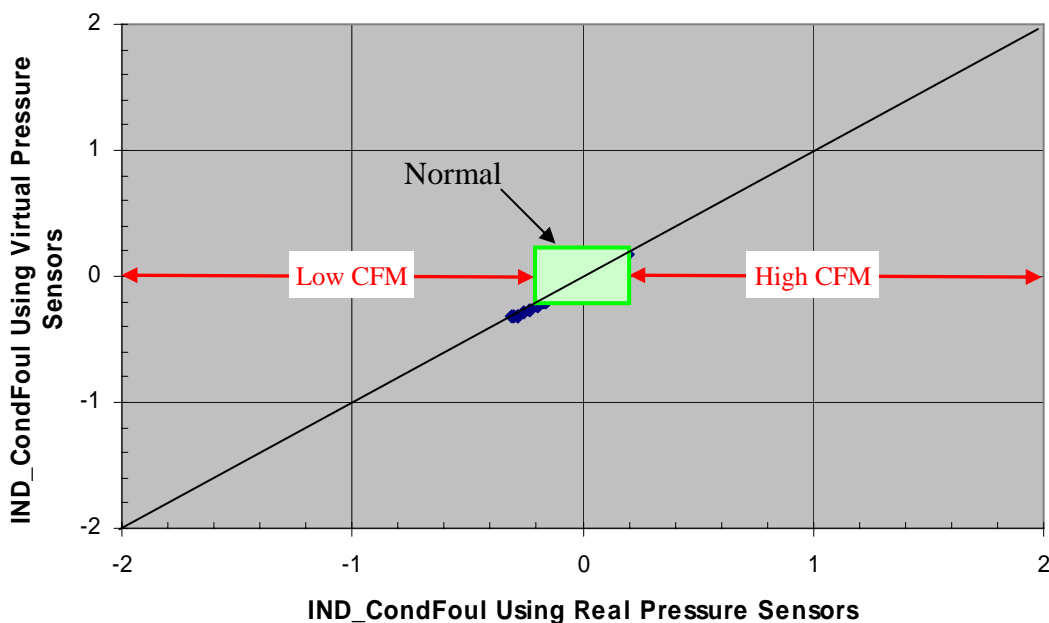


Figure 3.25 Condenser fouling indicator obtained using virtual pressure vs. condenser fouling indicator obtained using measured pressure

Figure 3.26 plots evaporator fouling fault indicators from virtual pressure sensors vs. those from real pressure sensors. Since both low and high evaporator CFMs were introduced in testing, points reside inside, to the left of, and to the right of the box. It can be seen that evaporator fouling fault indicators using virtual pressure sensors agree with those using real

pressure sensors very well and there is no FDD decision difference between using real pressure sensors and using virtual pressure sensors.

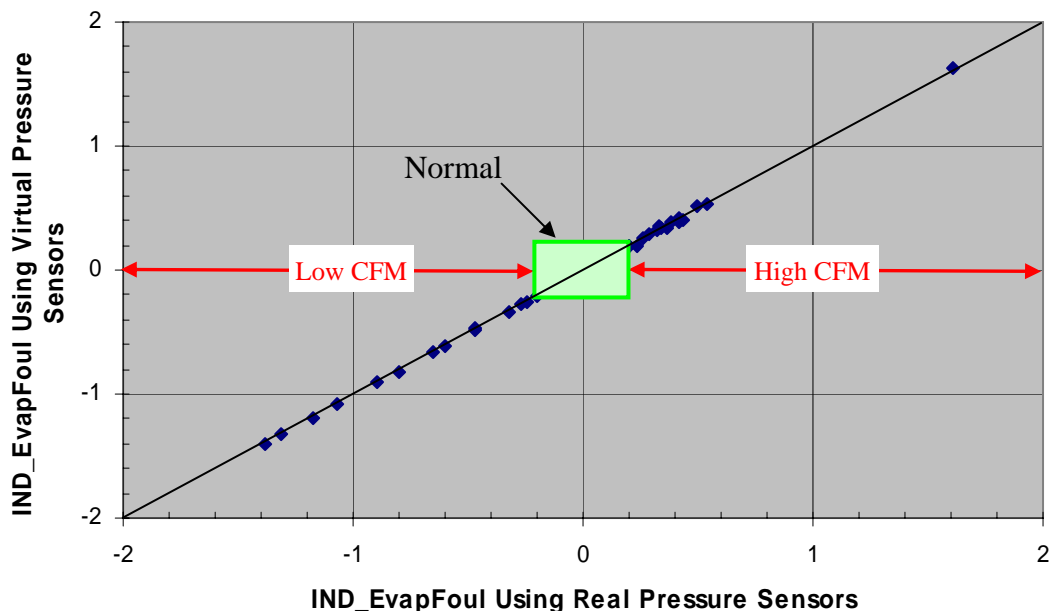


Figure 3.26 Evaporator fouling indicator from virtual pressure vs. evaporator fouling indicator from measured pressure

Figure 3.27 plots refrigerant charge fault indicators from virtual pressure sensors vs. those from real pressure sensors. There are three regions corresponding to normal refrigerant charge level, high refrigerant charge level, and low refrigerant charge level. Since both low and high refrigerant charge levels were introduced in testing, points reside inside, to the left of, and to the right of the box. It can be seen that refrigerant charge fault indicators determined using virtual pressure sensors agree with those determined using real pressure sensors very well and there is no FDD decision difference between using real pressure sensors and using virtual pressure sensors.

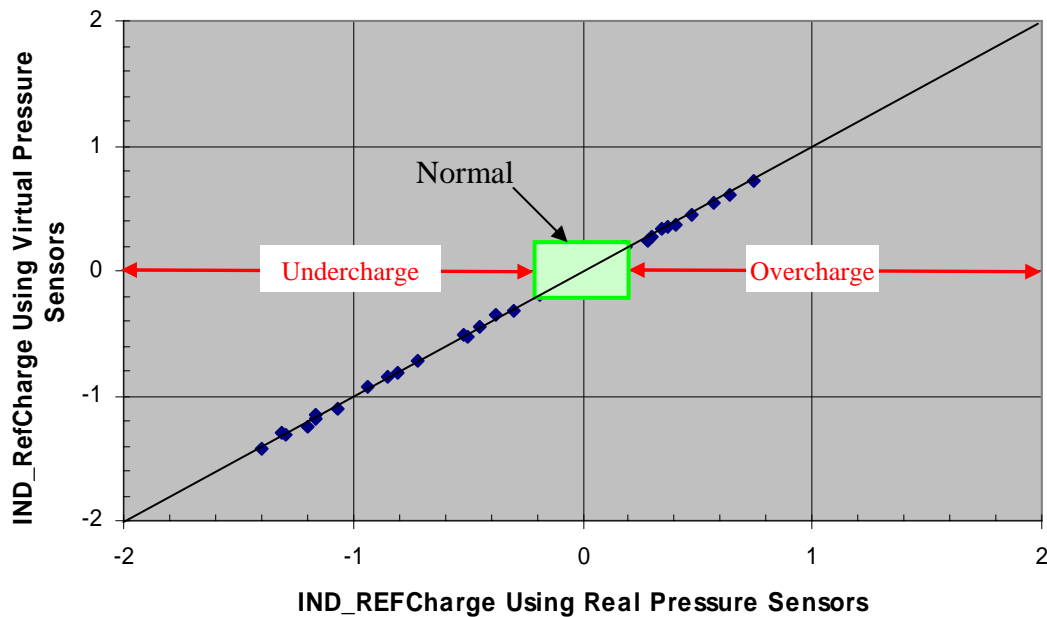


Figure 3.27 Refrigerant charge fault indicator from virtual pressure vs. refrigerant charge fault indicator from measured pressure

3.3.2.2 System II -- Split fixed orifice air conditioners

Similar to the packaged system, diagnosis results for the split fixed orifice system are demonstrated in Figures 3.28, 3.29, 3.30 and 3.31. It can be seen that all fault indicators from virtual pressure sensors agree with those from real pressure sensors very well and there is no FDD decision difference between using real pressure sensors and using virtual pressure sensors.

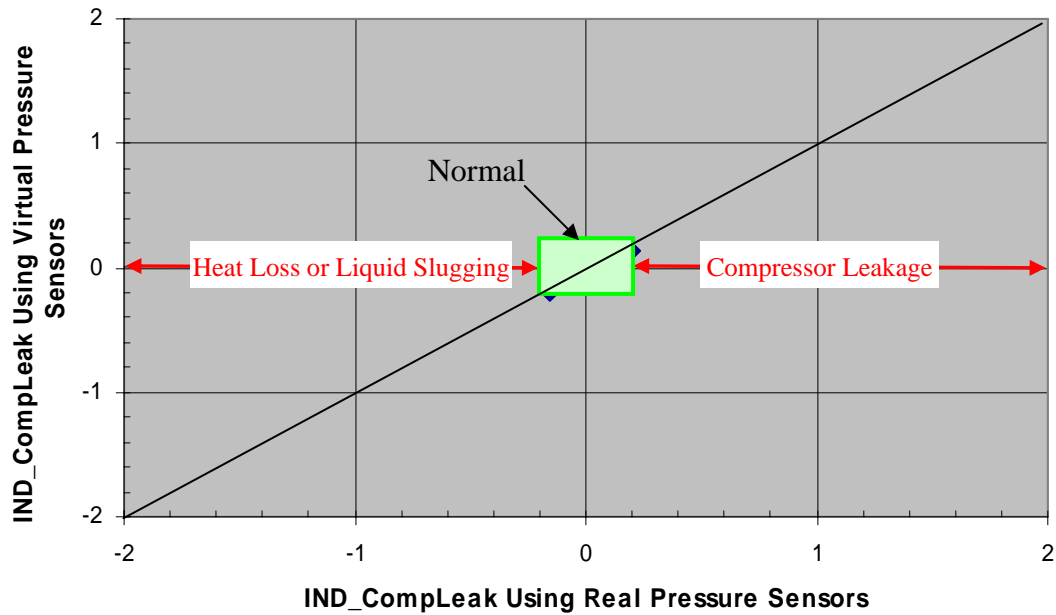


Figure 3.28 Compressor leakage indicator from virtual pressure vs. compressor leakage indicator from measured pressure

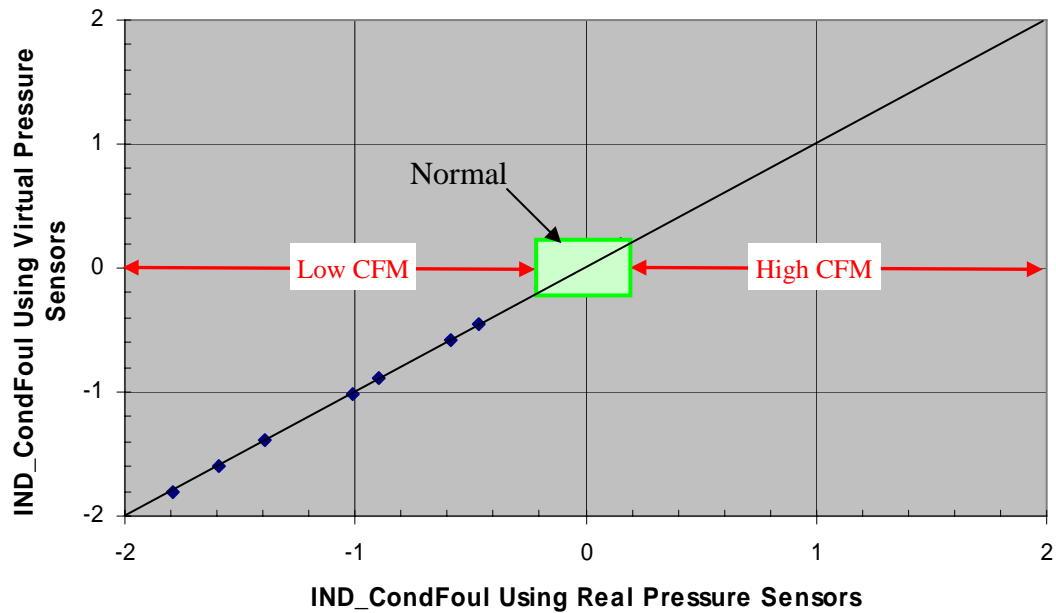


Figure 3.29 Condenser fouling indicator from virtual pressure vs. condenser fouling indicator from measured pressure

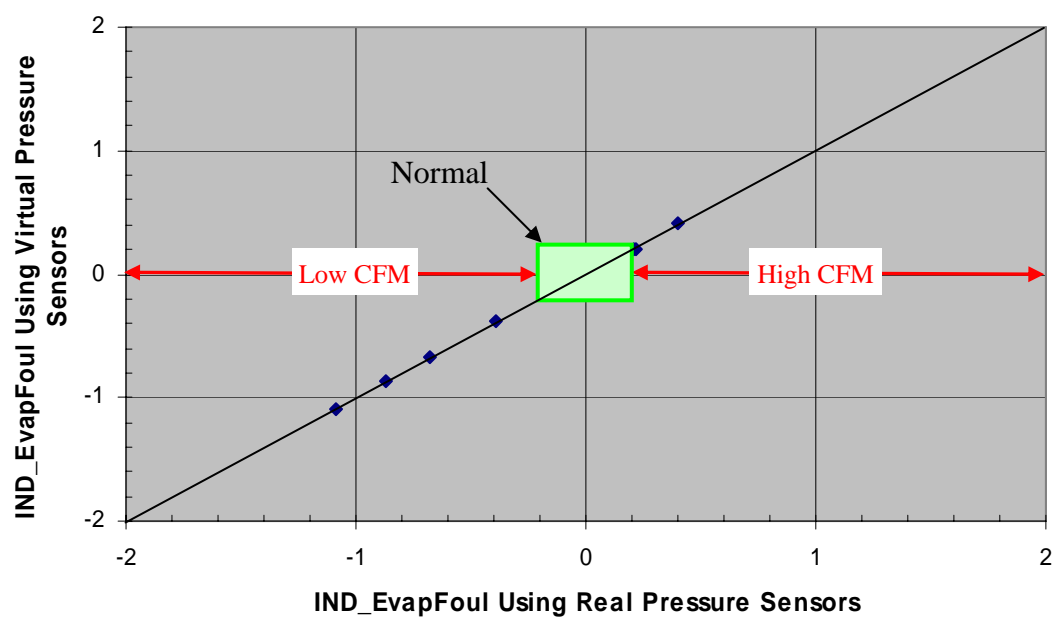


Figure 3.30 Evaporator fouling indicator from virtual pressure vs. evaporator fouling indicator from measured pressure

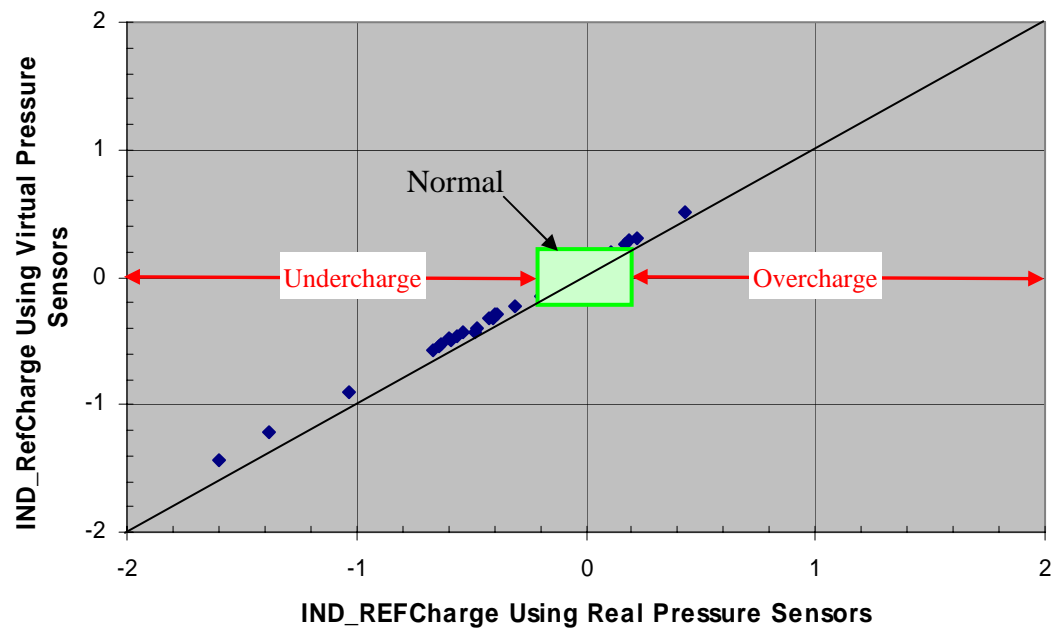


Figure 3.31 Refrigerant charge fault indicator from virtual pressure vs. refrigerant charge fault indicator from measured pressure

3.3.2.3 System III -- Split TXV air conditioners

Diagnosis results for the split TXV system are demonstrated in Figures 3.32, 3.33, 3.34 and 3.35. It can be seen that all fault indicators determined using virtual pressure sensors agree with those obtained using real pressure sensors very well and there is no FDD decision difference between using real pressure sensors and using virtual pressure sensors.

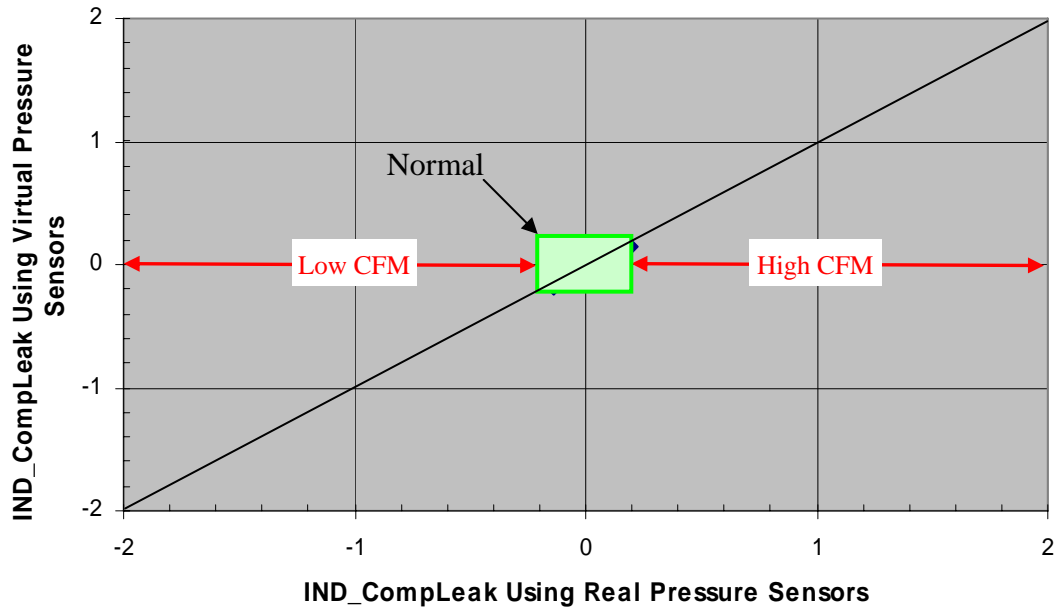


Figure 3.32 Compressor leakage indicator from virtual pressure vs. compressor leakage indicator from measured pressure

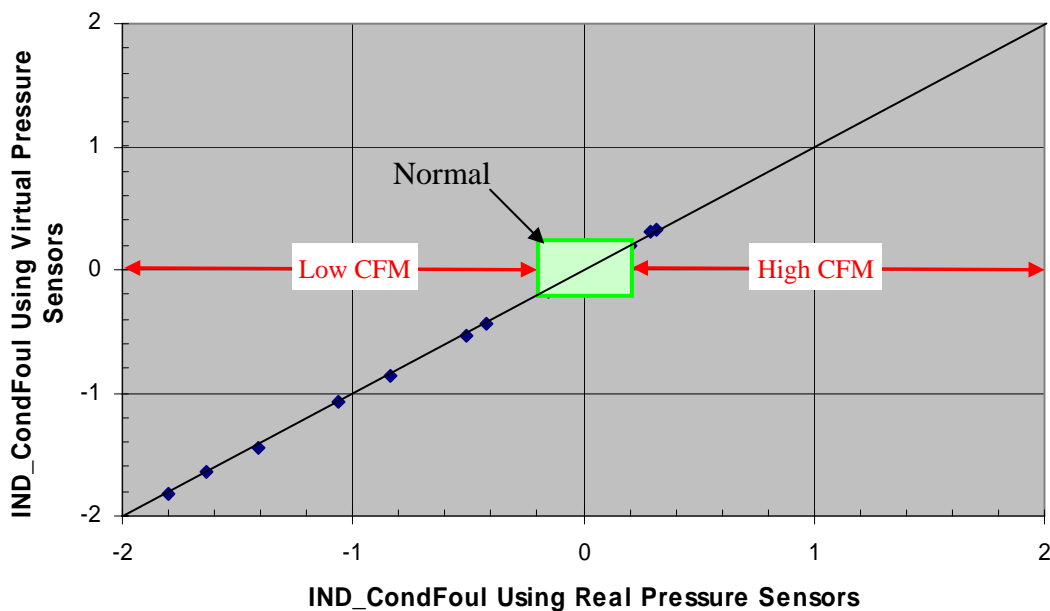


Figure 3.33 Condenser fouling indicator from virtual pressure vs. condenser fouling indicator from measured pressure

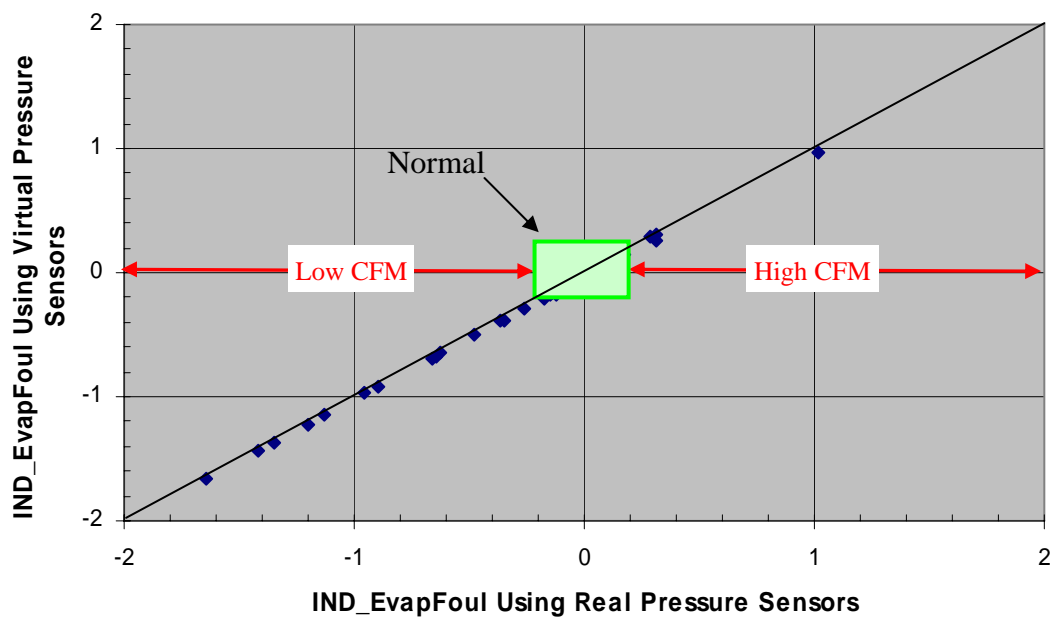


Figure 3.34 Evaporator fouling indicator from virtual pressure vs. evaporator fouling indicator from measured pressure

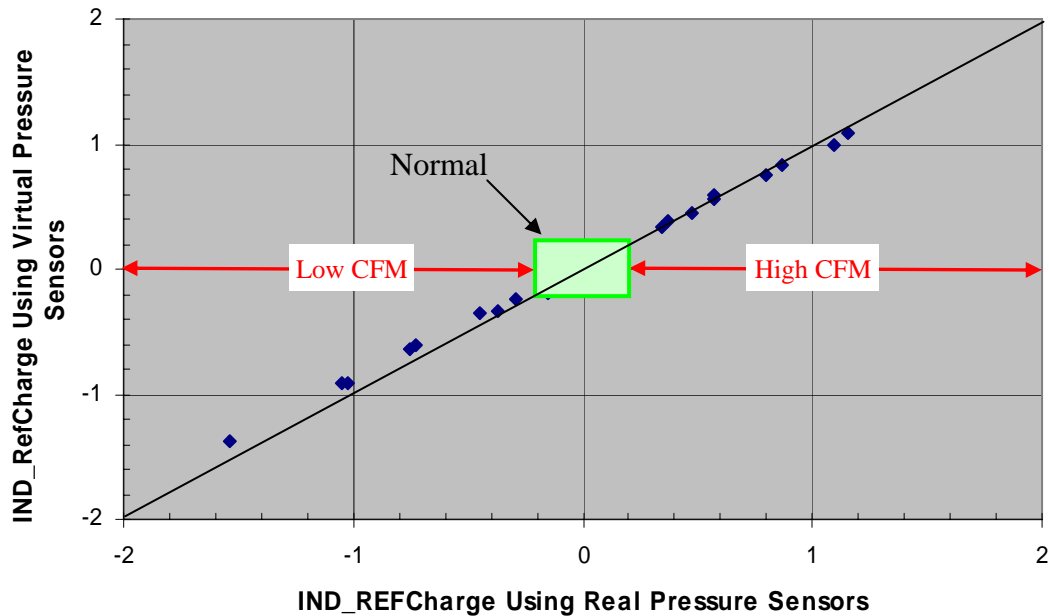


Figure 3.35 Refrigerant charge fault indicator from virtual pressure vs. refrigerant charge fault indicator from measured pressure

3.4 Conclusions

The temperature sensor only technique is practical and feasible: 1) the identified two-phase location is robust, 2) the constant pressure drop approximation method works reasonably well, 3) the resulting calculated variables have reasonably good accuracy, and 4) fault indicators determined using virtual pressure sensors agrees with those obtained using real pressure sensors very well and there is no FDD decision difference between using real pressure sensors and using virtual pressure sensors.

4 PERFORMANCE MONITORING INDICES

To evaluate the performance of the monitored system, simple indices were developed. These indices measure impact on comfort, indoor air quality, efficiency, reliability, control performance, etc. and are determined from low-cost measurements.

4.1 Comfort and Indoor Air Quality Indices

The principal purpose of air conditioning systems is to provide conditions for human thermal comfort. Among various thermal comfort factors, temperature and humidity are widely used as comfort indices. As shown in Figure 4.1, ASHRAE (1993) defines a normal thermal comfort region – the polygon – in the psychrometric chart, which has been updated to ASHRAE Standard 55-22004. Accordingly, return air state (temperature and humidity) can be plotted in the psychrometric chart to indicate whether the conditioned space satisfies the thermal comfort criterion. In Figure 4.1, the points residing inside the polygon indicate that the conditioned space is comfortable, while those points residing outside the red polygon indicate that the conditioned space is uncomfortable.

Since the discomfort identified by checking return air states can be caused either by undersized equipment or cooling capacity degradation due to faults, cooling capacity degradation can be used as a complementary comfort index for discriminating the causes. To visualize cooling capacity degradation, Figure 4.2 plots the current cooling capacity vs. normal cooling capacity expected by given driving conditions for the packaged air conditioner with R410a as the refrigerant and FXO as the expansion device. Cooling capacity can be determined from virtual sensors (Li, 2004).

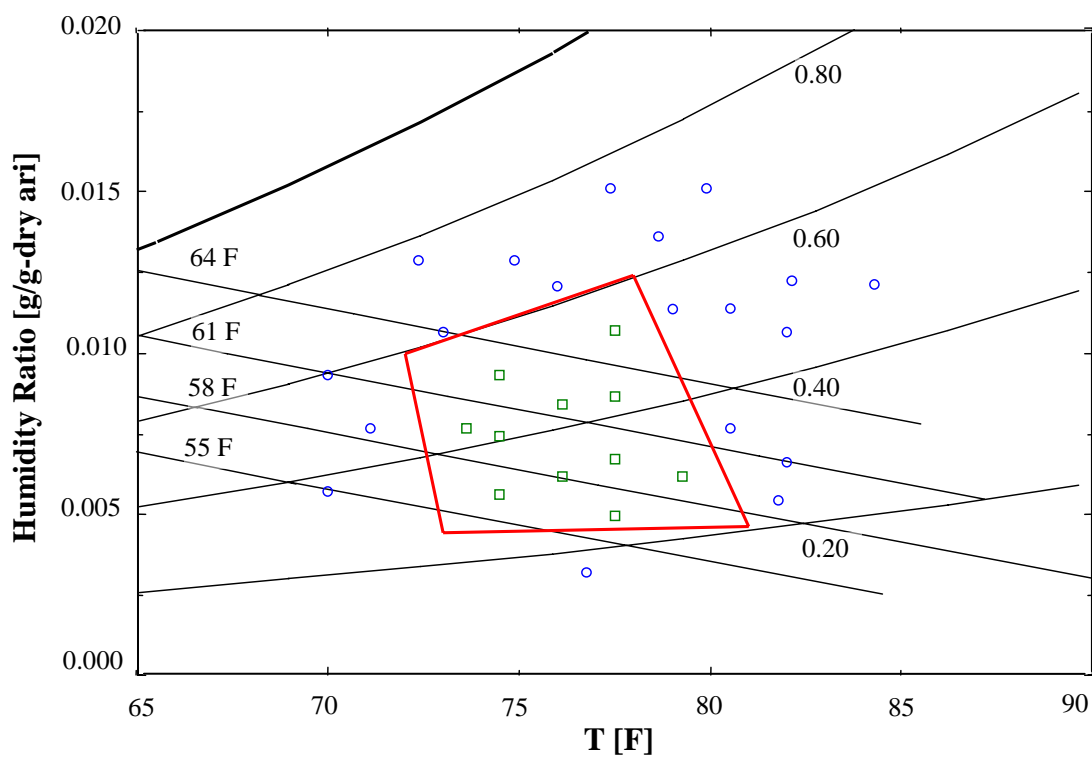


Figure 4.1 Thermal comfort plot in psychrometric chart

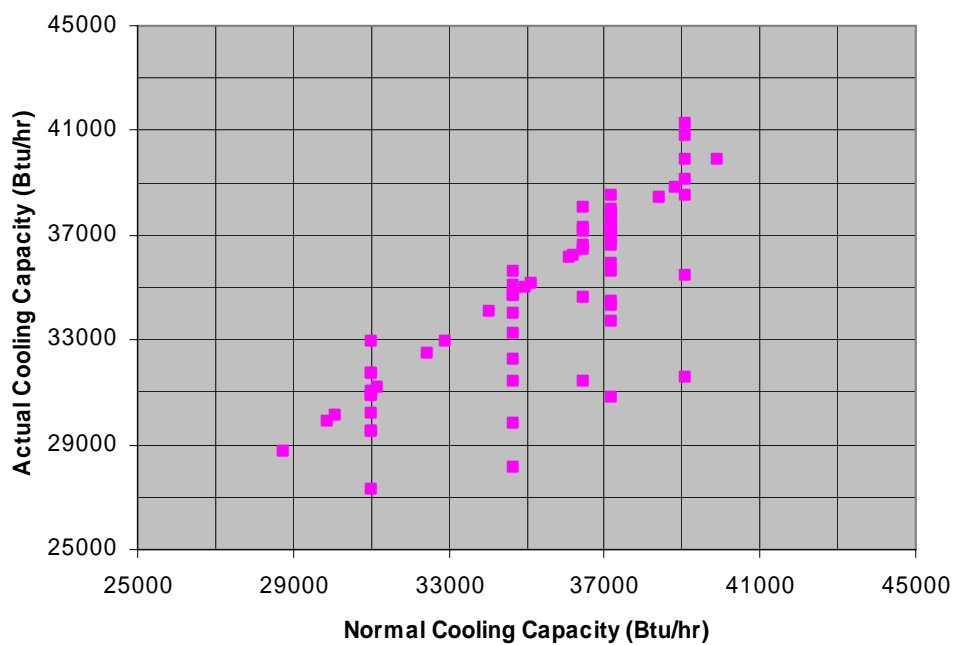


Figure 4.2 Actual cooling capacity vs. normal cooling capacity for the packaged air conditioner with R410a as the refrigerant and FXO as the expansion device

As shown in Figure 4.3, FDSI developed an outdoor air fraction plot as one indicator of outdoor air (OA) damper performance. This plot shows the variation of the outdoor air fraction for a unit on a particular day. The outdoor air fraction (OAF) is divided into 11 bins (range of values). The Y-axis represents the time fraction of a day spent in these bins for the unit and the X-axis represents the OAF bins. This plot can be used to illustrate various operation modes including minimum OA damper position during occupied periods, closed OA damper during unoccupied periods, economizer operation, and demand controlled ventilation operation.

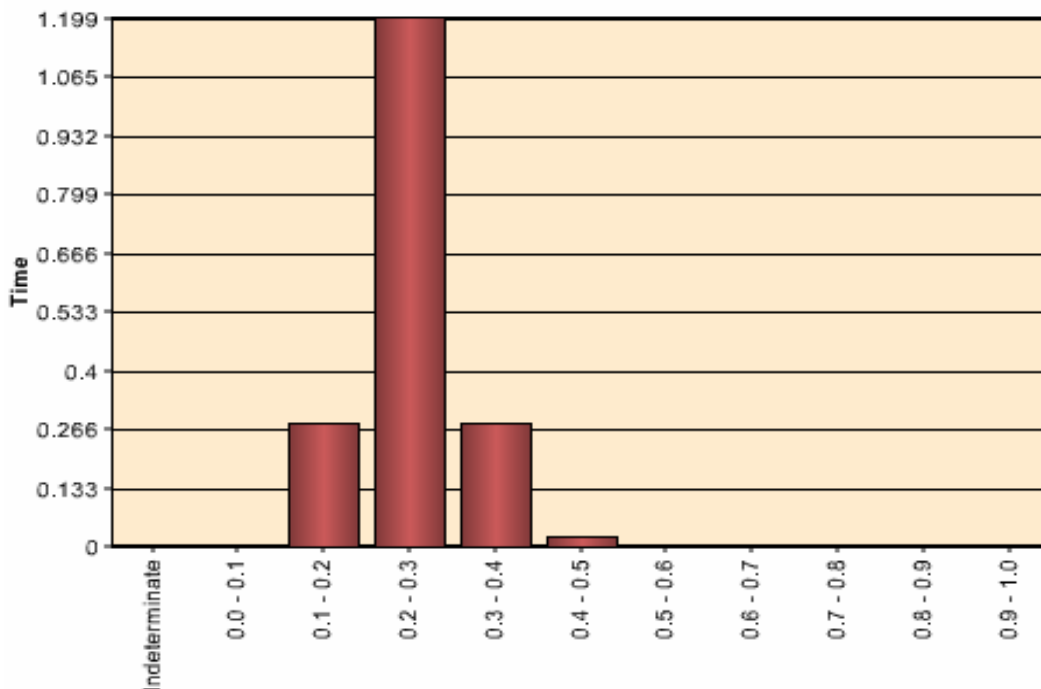


Figure 4.3 Outdoor air fraction plot

4.2 Efficiency and Economic Indices

By definition, energy efficiency ratio (EER) or coefficient of performance (COP) is a simple index for monitoring equipment energy efficiency. When a system runs abnormally, its EER tends to reduce. The more the EER reduces, the more the system degrades. Since the system EER is not only impacted by faults but also varies with its driving conditions, current EER values should be compared with expected normal EER values for the driving conditions. As shown in Figure 4.4, current EER values can be plotted vs. normal EER values to indicate

whether the monitored equipment is running efficiently or not. EER can be estimated using virtual sensors (Li, 2004).

However, degradation of EER (or COP) is not sufficient for evaluating the overall economic performance degradation. Braun and Li (2004a) thoroughly investigated possible factors which affect economics of air conditioning equipment and found that: 1) EER or COP quantifies a portion of the economic performance of a refrigeration system and their degradation directly raises the operating costs; 2) besides compromising the comfort of a conditioned space, capacity degradation also reduces equipment life due to longer runtime required to meet the same load demand; 3) SHR degradation increases operating costs due to higher latent loads for the same sensible load. In order to consider all three performance degradations, a new overall economic performance degradation index, termed EPDI, was defined. EPDI can be used for both fault evaluation and FDD evaluation. Fault evaluation uses EPDI to estimate the operating cost savings related to repairing diagnosed faults.

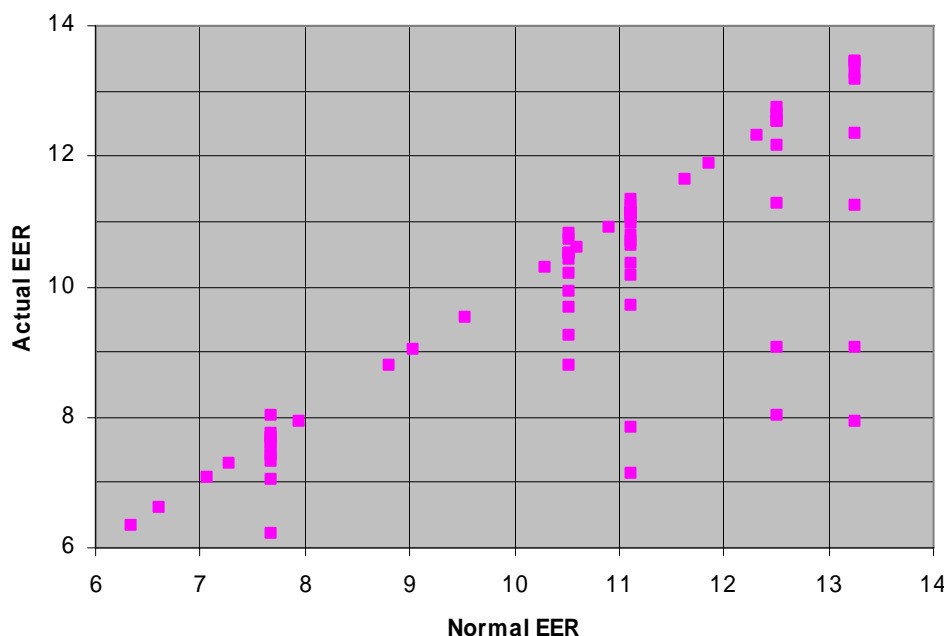


Figure 4.4 Actual EER vs. normal EER for the packaged air conditioner with R410a as the refrigerant and FXO as the expansion device

4.3 Reliability Index

Faults impact equipment reliability/safety through endangering the compressor, which mainly includes two aspects: compressor overheating and slugging. Compressor discharge line temperature and suction line superheat are two inexpensive indices that work well for monitoring compressor reliability/safety due to the following reasons: a) the compressor discharge line temperature is a direct indicator for the maximum compressor operating temperature which is should be less than a certain value (140 C for some compressors) to make sure the compressor lubricant works properly; b) too small suction line superheat will endanger the compressor valve due to slugging and abnormally high suction superheat could not cool the compressor motor enough so that it may burn the coil out. So both compressor discharge line temperature and suction line superheat are used to monitor the compressor safety.

4.4 Control and miscellaneous indices

Besides comfort and efficiency and reliability, some other equipment control-related performance indices were developed by FDSI: 1) compressor run time plots, 2) compressor off time plots, and 3) economizer operation plots.

Compressor cycle performance indices were developed to identify control problems that may lead to a reduction in equipment life. The compressor operation for a cooling cycle is defined as a runtime and off time as shown in Figure 4.5. The data are sorted into bins based on cycle off time and also cycle runtime. An example of compressor runtime data is presented in Figure 4.6. The compressor run time plot depicts the number of compressor run cycles (shown as a percentage) that lie within a specified time range (bins). The data are used to identify if a compressor has short runtimes and the plot is used to illustrate the behavior. An example of compressor off time data is presented in Figure 4.7. The data are used to identify if a compressor has short off times and to evaluate the performance relative to manufacturers' recommendations. Manufacturers' typically recommend a minimum compressor off time of 5 minutes to allow refrigerant pressures to equalize in the system.

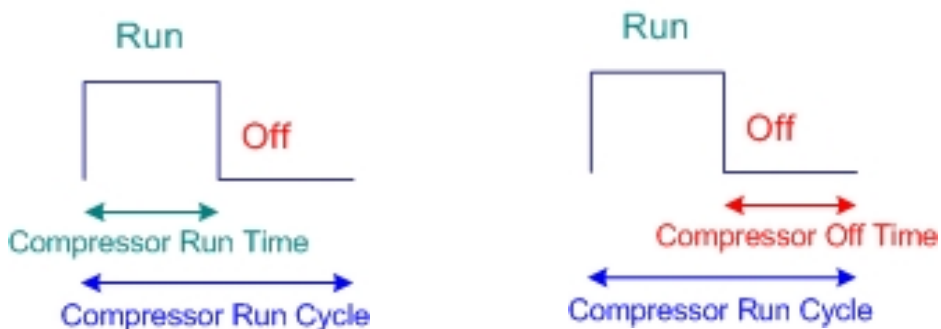


Figure 4.5 Definition of a compressor run cycle

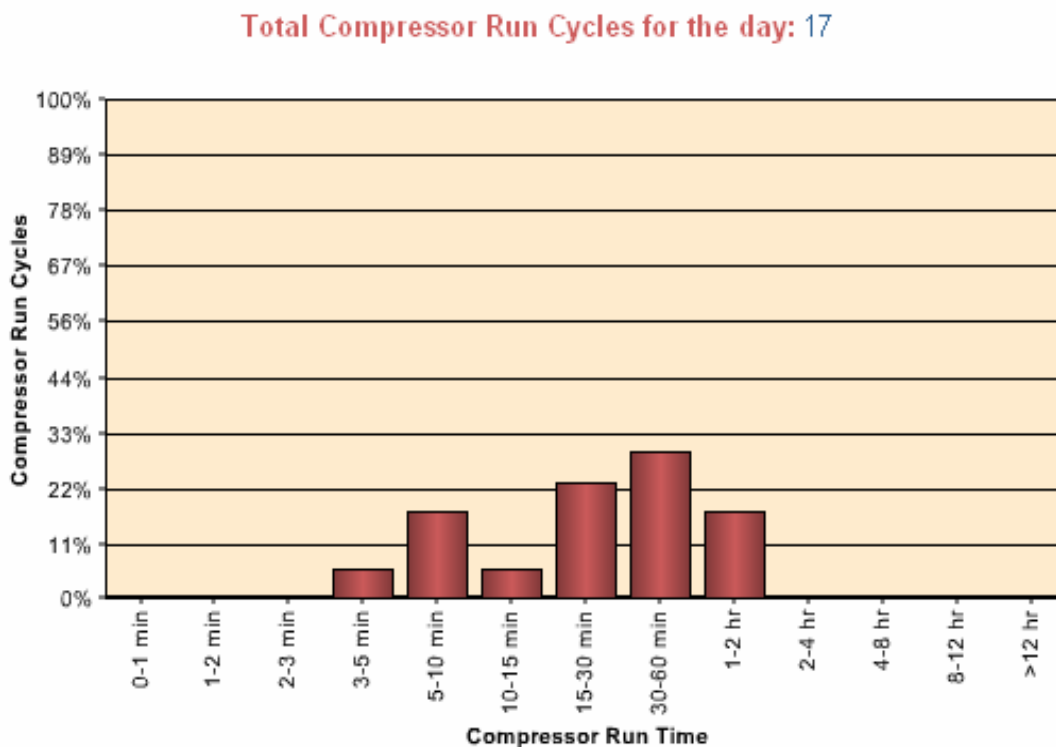


Figure 4.6 Compressor runtime plot

An outdoor air damper performance plot was developed using the air temperature measurements of return air temperature (RAT), outdoor air temperature (OAF) and mixed air temperature (MAT). An example plot is shown in Figure 4.7. The Y-axis is (MAT-RAT) and the X-axis is (OAT-RAT). The white line of slope 1 indicates points when the system is operating

with 100% outdoor air. Any data point above this line ($\text{MAT-RAT} < \text{OAT-RAT}$) represents operation with less than 100% outdoor air. The plot can be used to observe and evaluate several modes of operation including minimum OA damper position during occupied periods, closed OA damper during unoccupied periods, economizer operation, and demand controlled ventilation operation. The example plot represents economizer operation when OAT is less than RAT. An additional line can be added to indicate a damper minimum position during occupied periods.

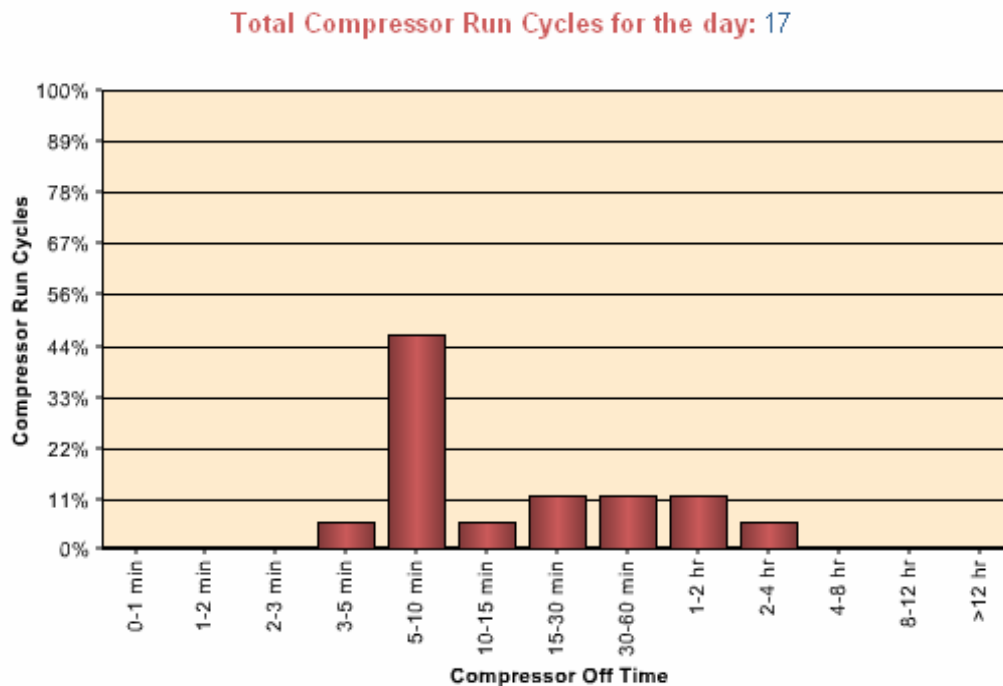


Figure 4.7 Compressor off time plot

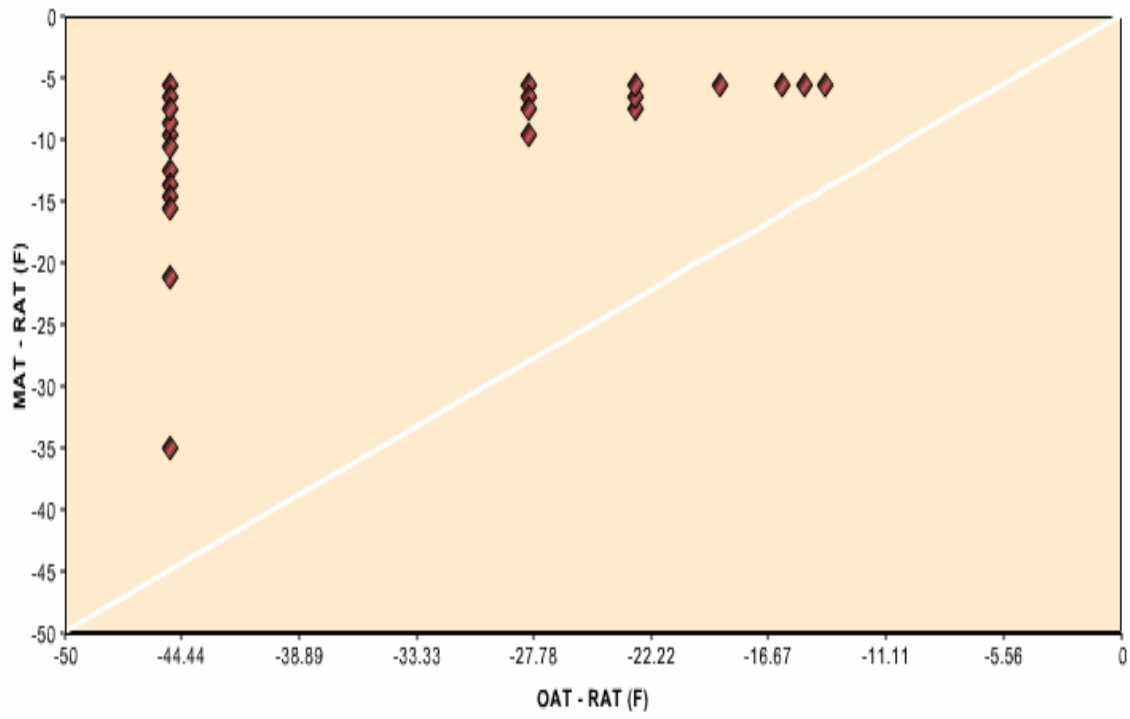


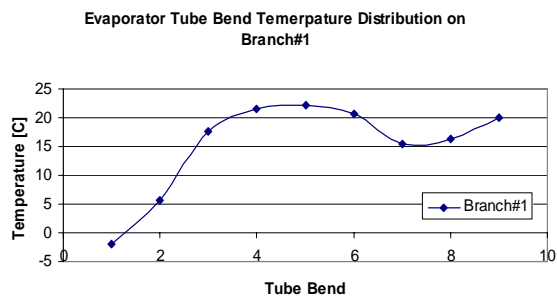
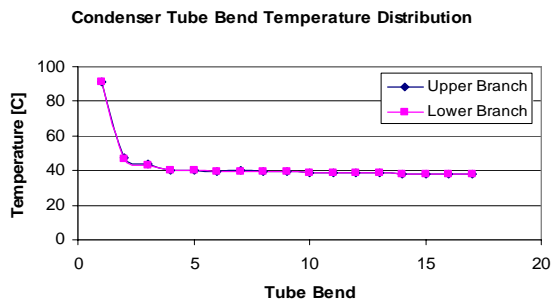
Figure 4.8 Economizer operation plot

REFERENCES

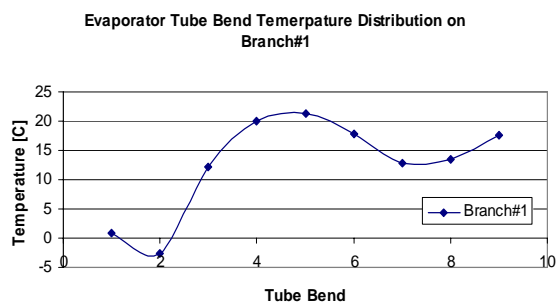
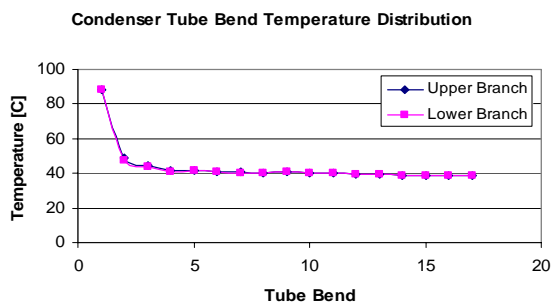
- ASHRAE. 1993, ASHRAE Handbook - 1993 Fundamentals, Atlanta: American Society of Heating, Refrigerating, and Air Conditioning Engineers, Inc., Atlanta, GA 30329.
- Braun, J.E. and Li, Haorong. 2003. "A decoupling-based FDD Approach for Multiple Simultaneous Faults". Progress report submitted to Architectural Energy Corporation.
- Braun, J.E. and Li, Haorong. 2004a. "Final Report for CEC Project Extension". Progress report submitted to Architectural Energy Corporation.
- Braun, J.E. and Li, Haorong. 2004b. "Final Report and Economic Assessment of Automated Fault Detection and Diagnostics of Rooftop Air Conditioners for California". Progress report submitted to Architectural Energy Corporation.
- Li, H., 2004, A Decoupling-Based Unified Fault Detection and Diagnosis Approach for Packaged Air-Conditioners, Ph.D. Thesis, School of Mechanical Engineering, Purdue University.
- Rossi, T.M. and Braun, J.E., 1997. A Statistical, Rule-Based Fault Detection and Diagnostic Method for Vapor Compression Air Conditioners, International Journal of Heating, Ventilating, and Air Conditioning and Refrigerating Research, Vol. 3, No. 1, pp.19-37.

Appendix A Condenser and Evaporator Tube Bend Temperature Profile

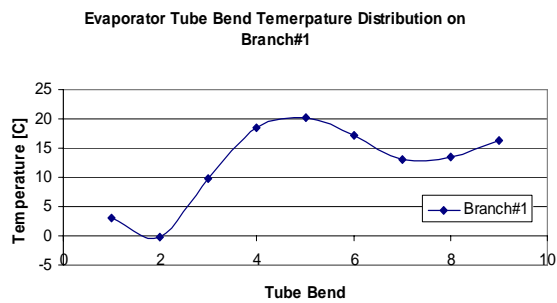
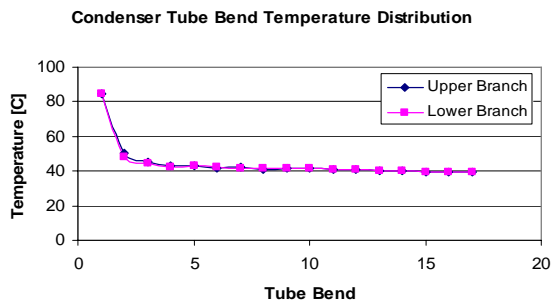
A. 1 Varying Charge with Dry Coil



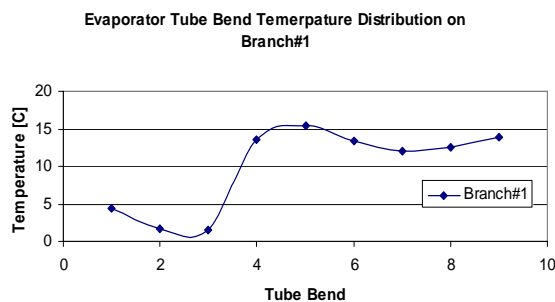
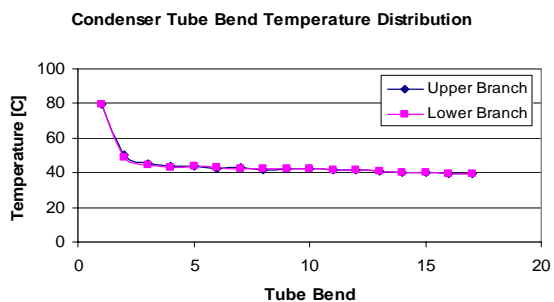
Charge = 3 lb with Dry Coil



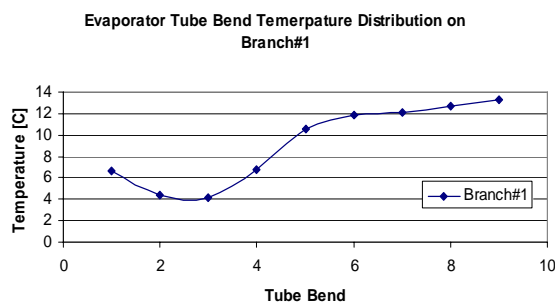
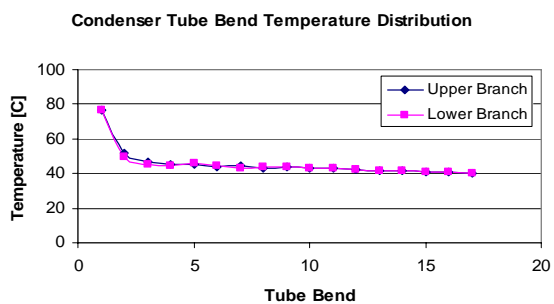
Charge = 3.5 lb Dry Coil



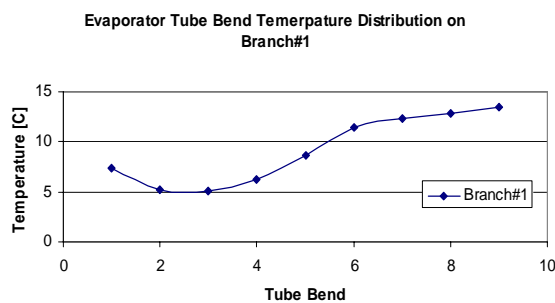
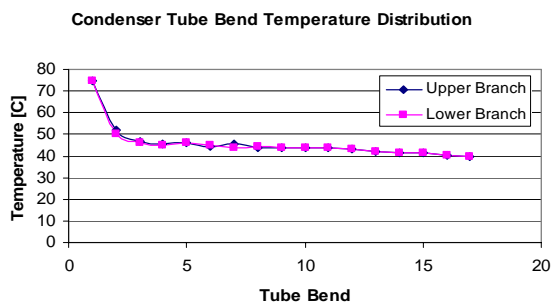
Charge = 4 lb Dry Coil



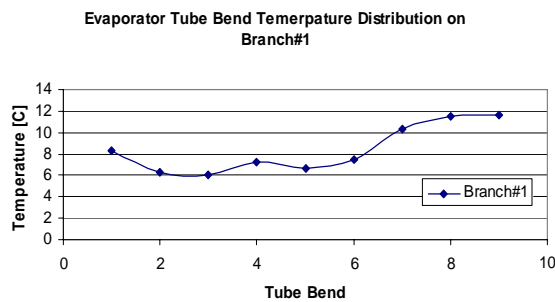
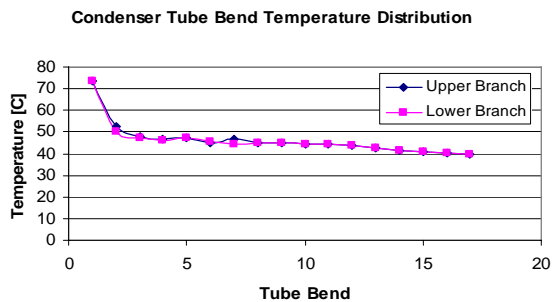
Charge = 4.5 lb Dry Coil



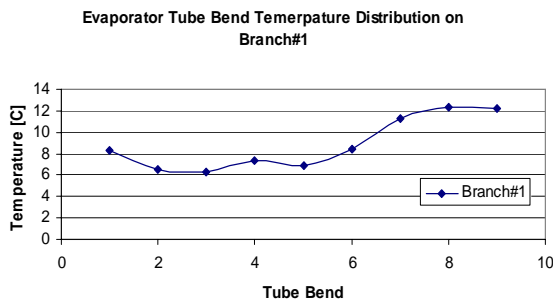
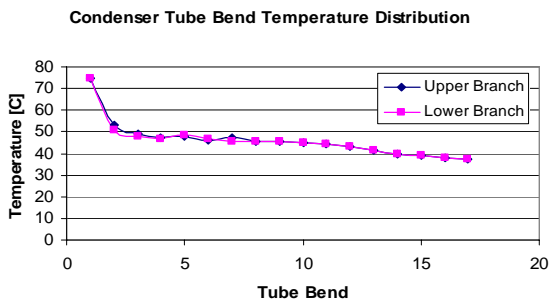
Charge = 5 lb Dry Coil



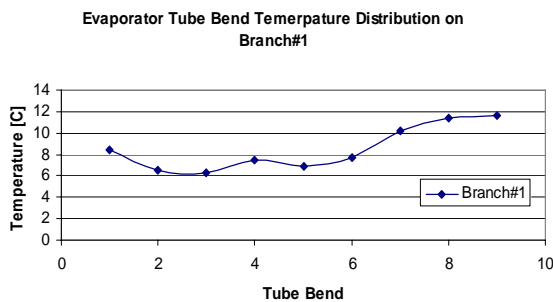
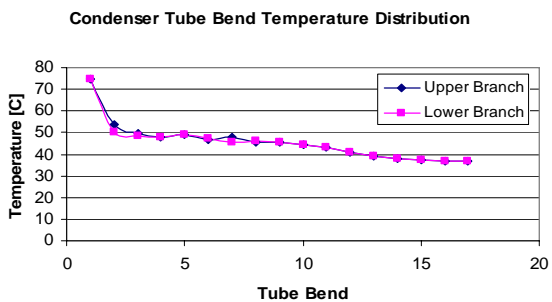
Charge = 5.5 lb Dry Coil



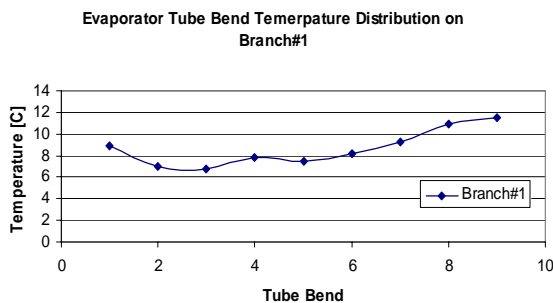
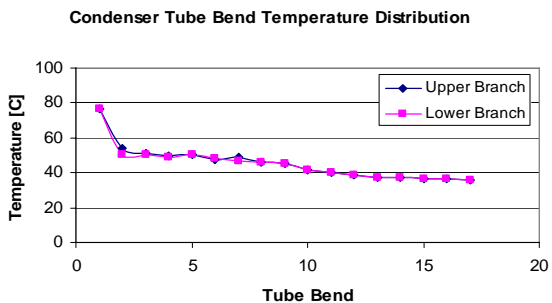
Charge = 6.3 lb Dry Coil



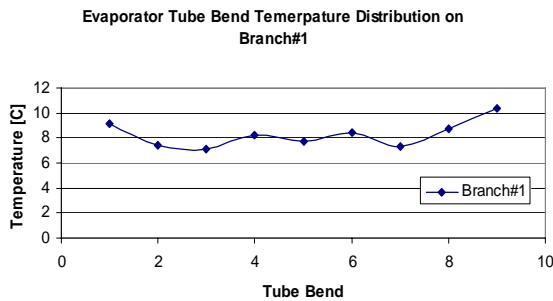
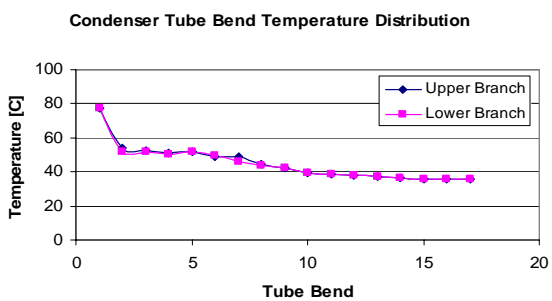
Charge = 6.8 lb Dry Coil



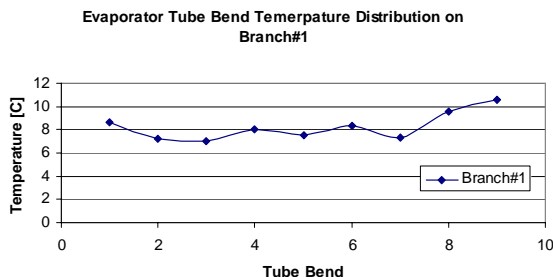
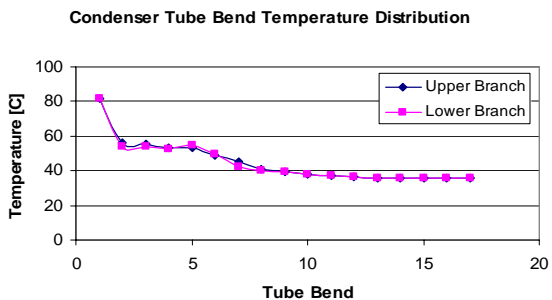
Charge = 7.3 lb Dry Coil



Charge = 7.8 lb Dry Coil

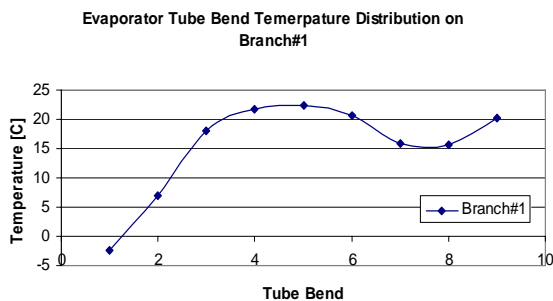
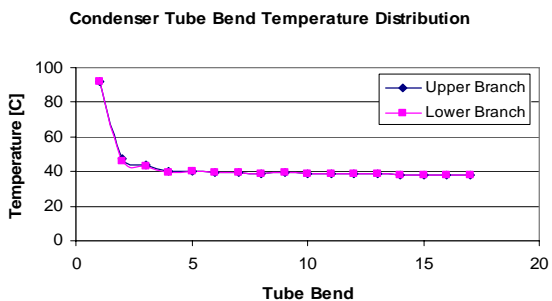


Charge = 8.3 lb Dry Coil

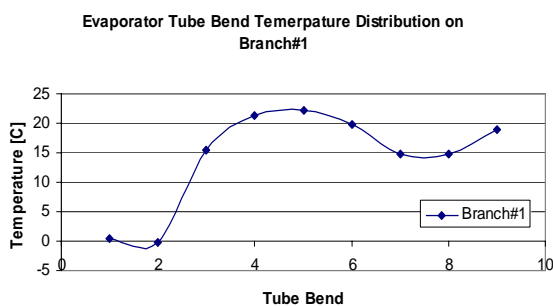
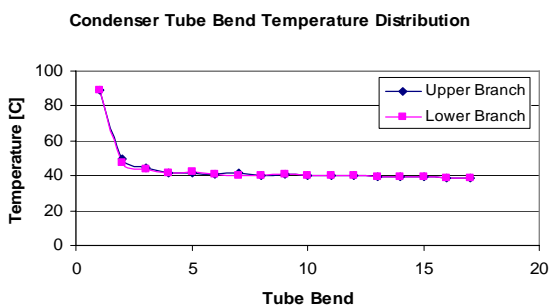


Charge = 8.8 lb Dry Coil

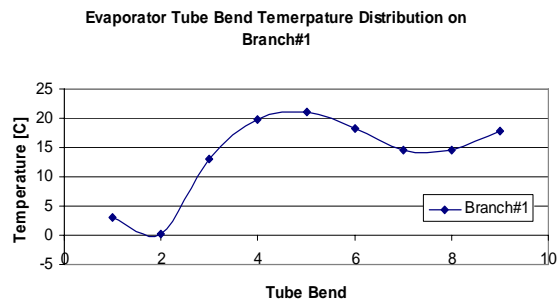
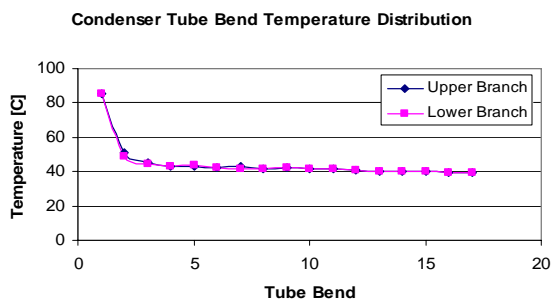
A.2 Varying Charge with Wet Coil



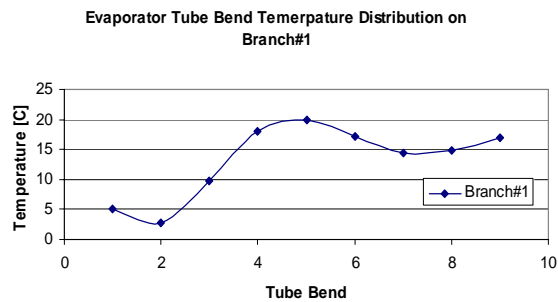
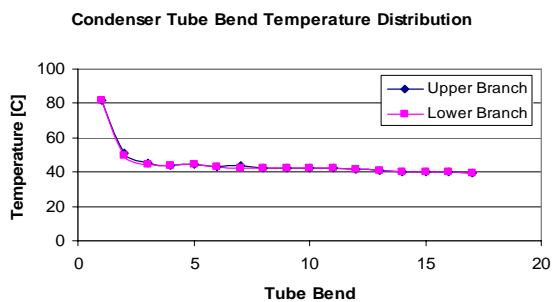
Charge = 3 lb Wet Coil



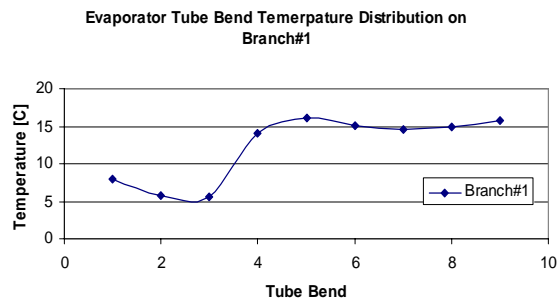
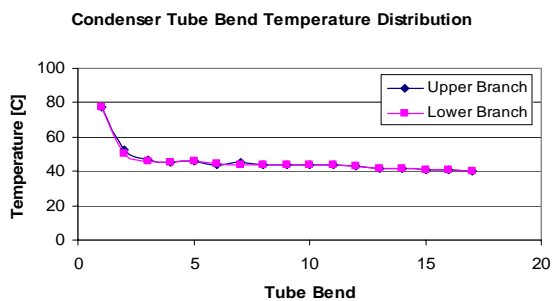
Charge = 3.5 lb Wet Coil



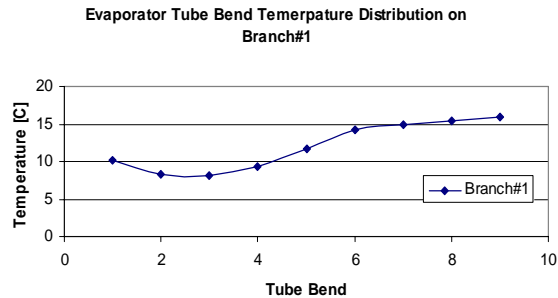
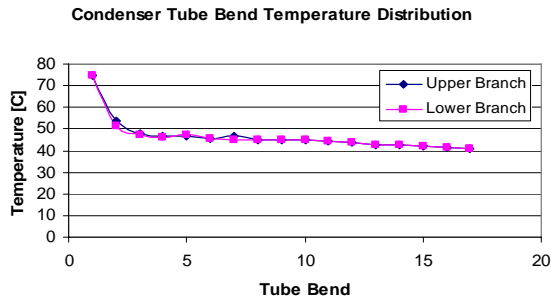
Charge = 4 lb Wet Coil



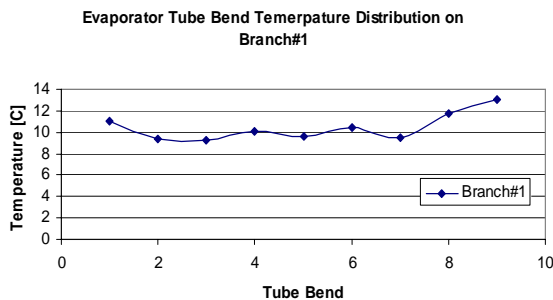
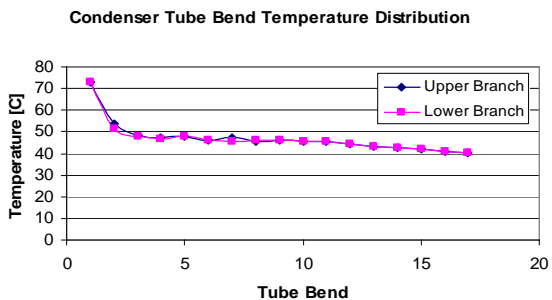
Charge = 4.5 lb Wet Coil



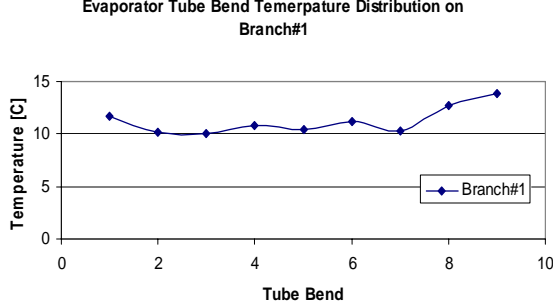
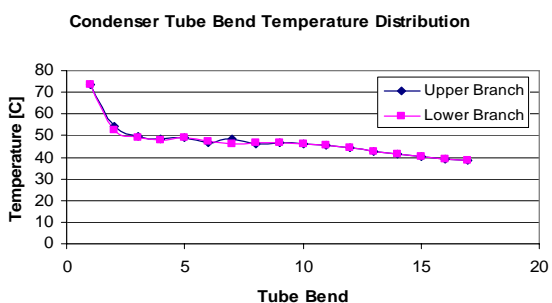
Charge = 5 lb Wet Coil



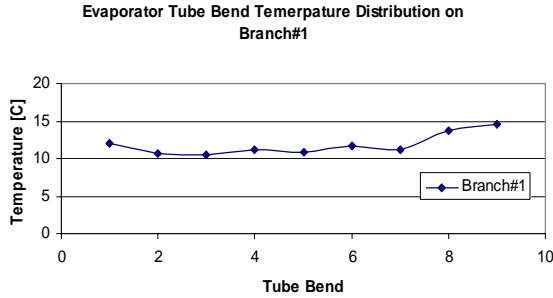
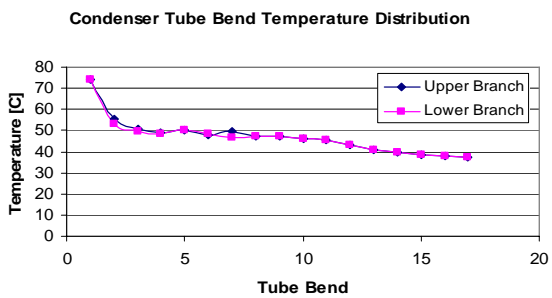
Charge = 5.5 lb Wet Coil



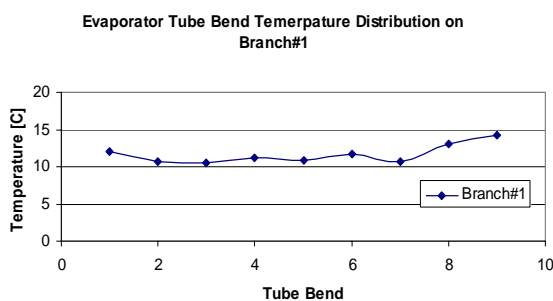
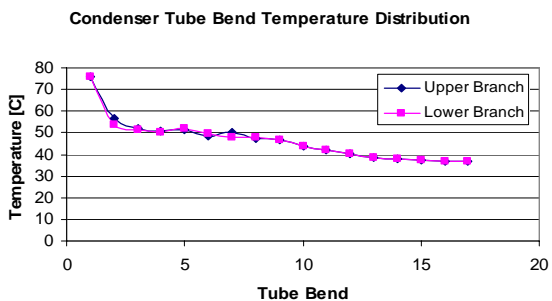
Charge = 6.3 lb Wet Coil



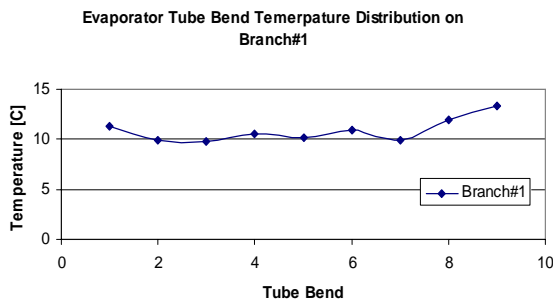
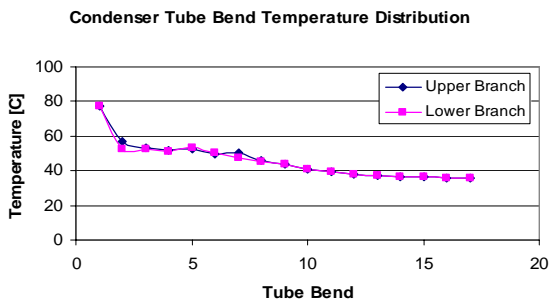
Charge = 6.8 lb Wet Coil



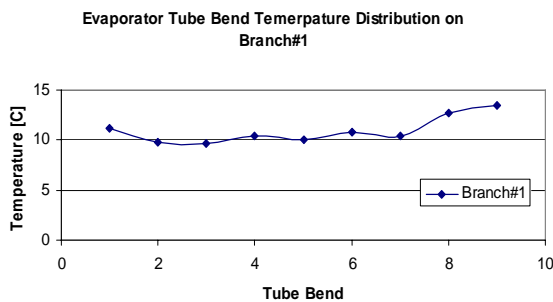
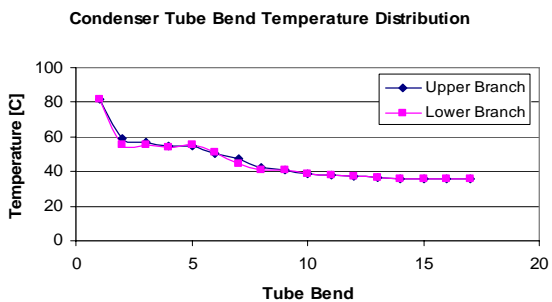
Charge = 7.3 lb Wet Coil



Charge = 7.8 lb Wet Coil

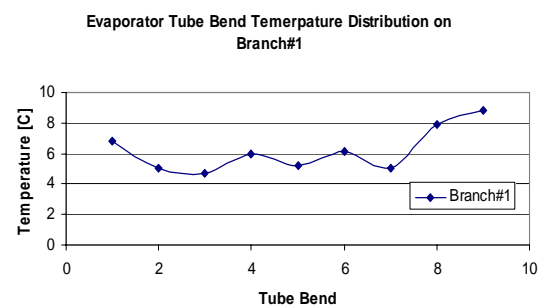
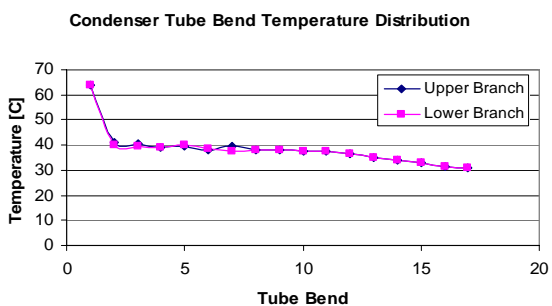


Charge = 8.3 lb Wet Coil

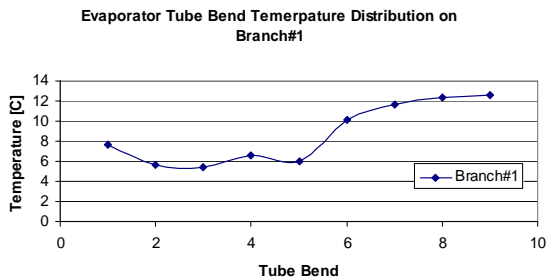
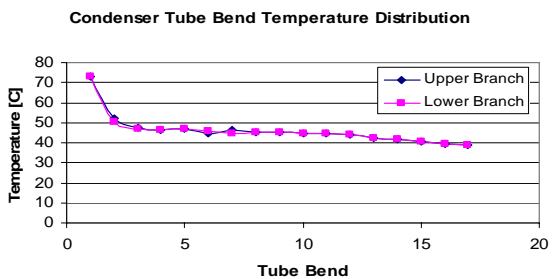


Charge = 8.8 lb Wet Coil

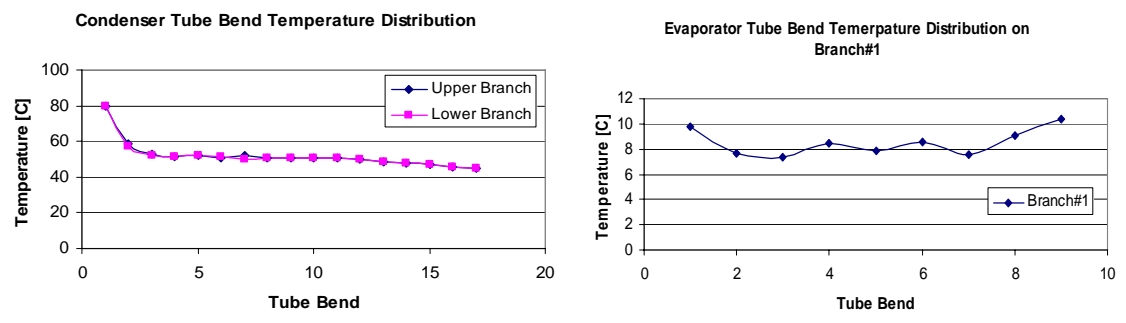
A.3 Varying Ambient Temperature with Dry Coil



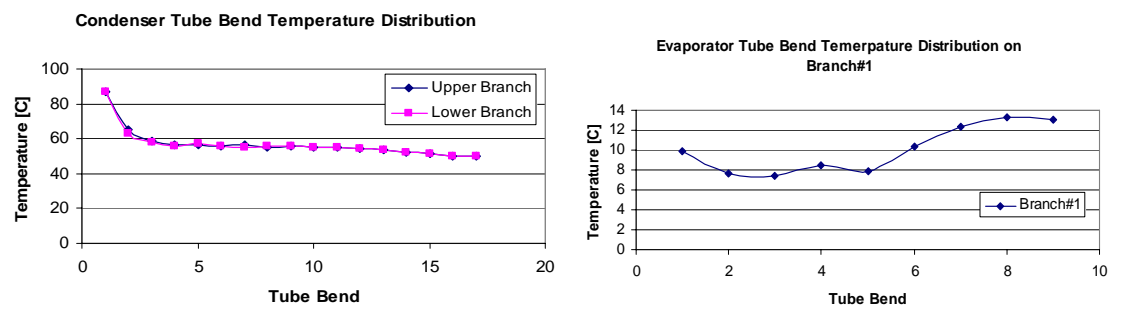
AMB= 82 with Dry Coil



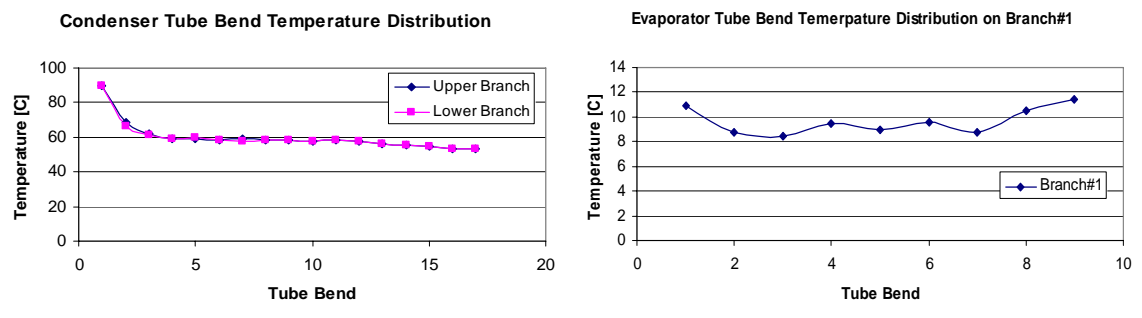
AMB= 95 with Dry Coil



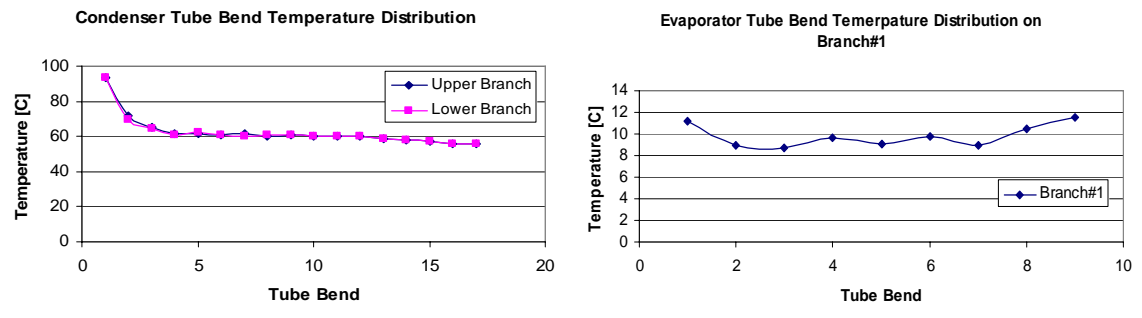
AMB= 105 with Dry Coil



AMB= 115 with Dry Coil

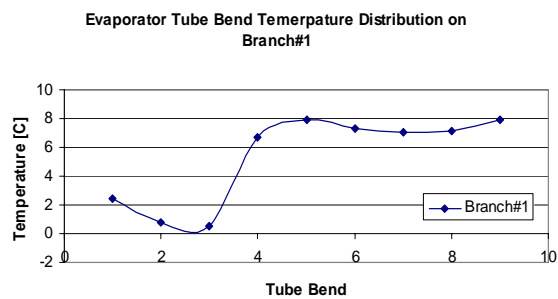
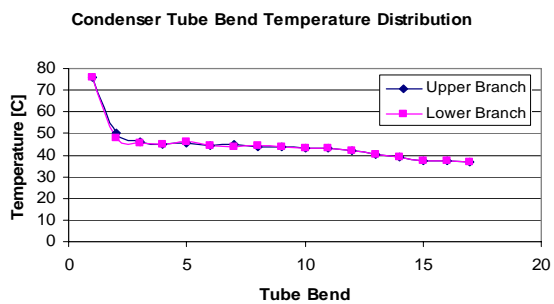


AMB= 120 with Dry Coil

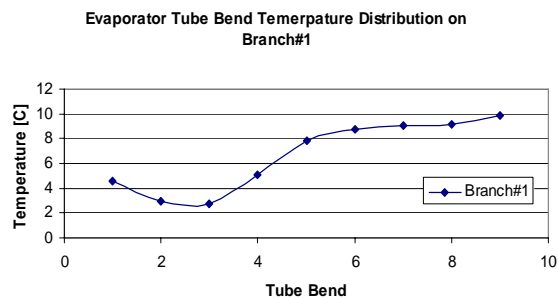
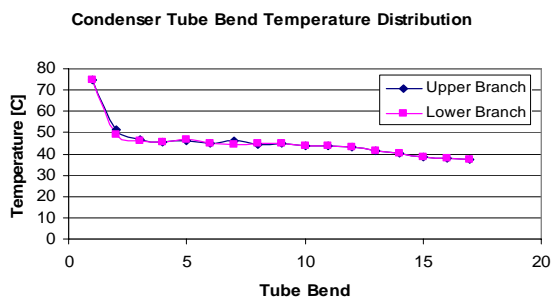


AMB= 125 with Dry Coil

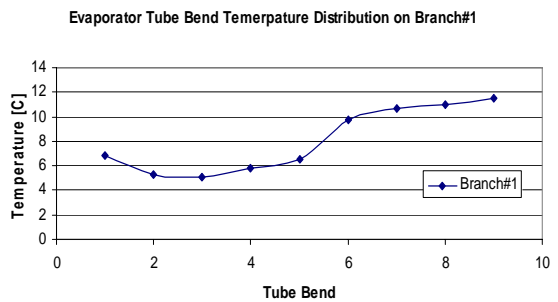
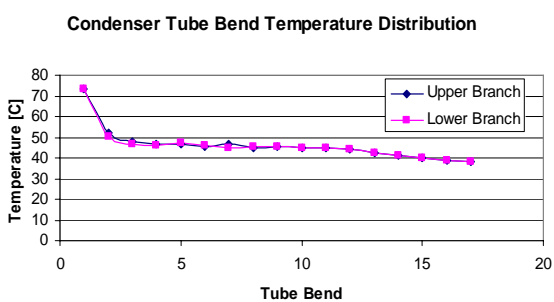
A.4 Varying Evaporator Air Flow (Wet)



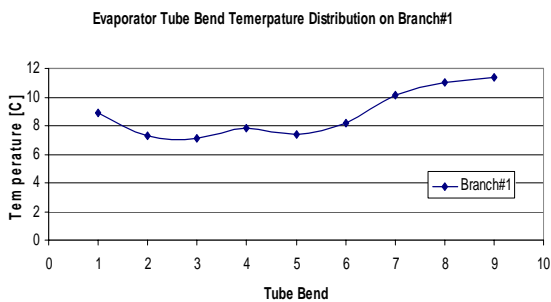
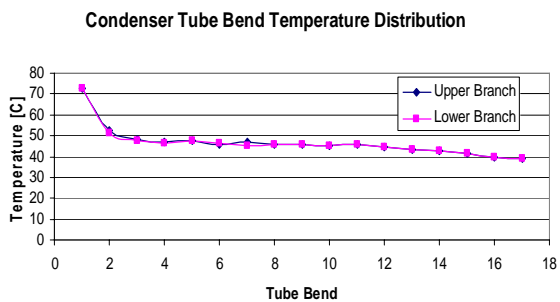
CFM=500



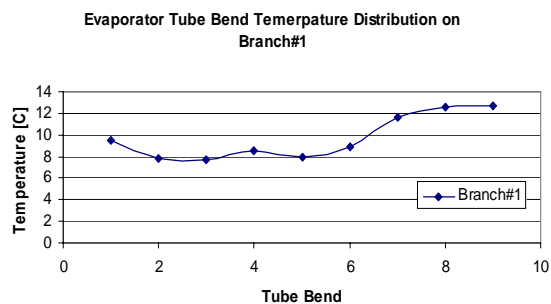
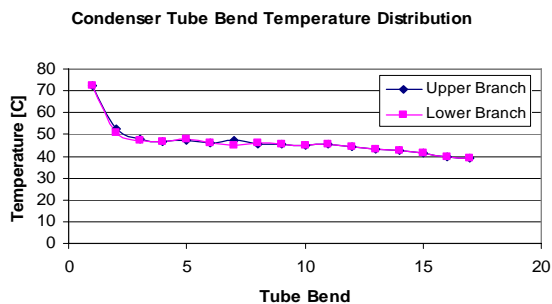
CFM=600



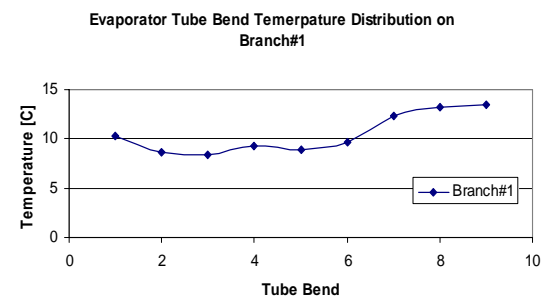
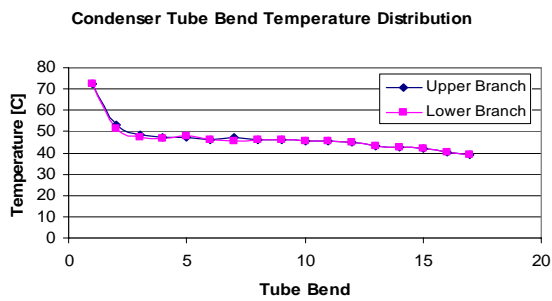
CFM=700



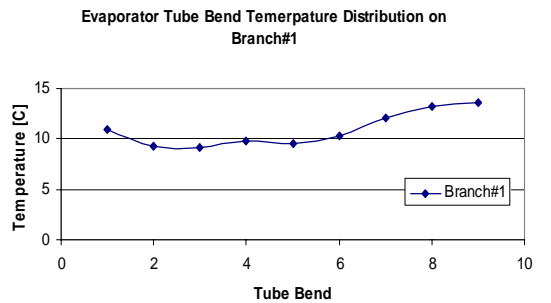
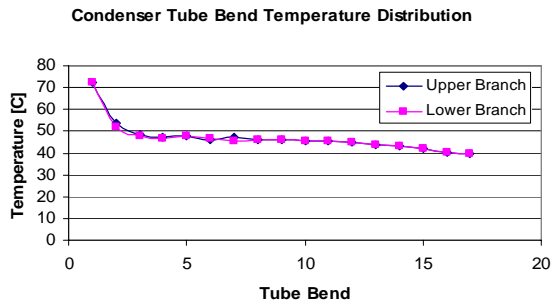
CFM=800



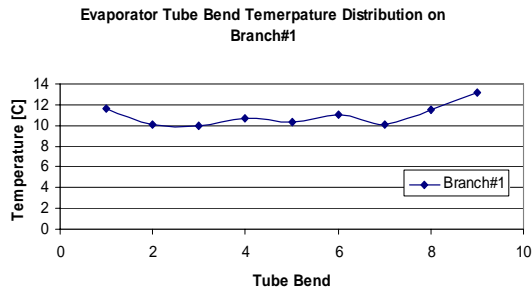
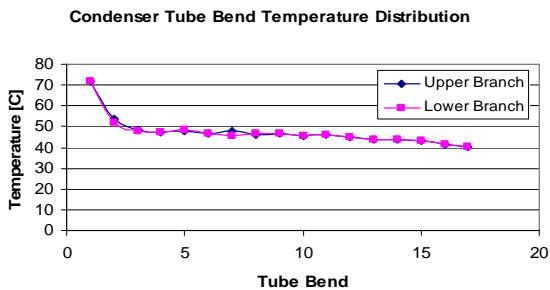
CFM=900



CFM=1000

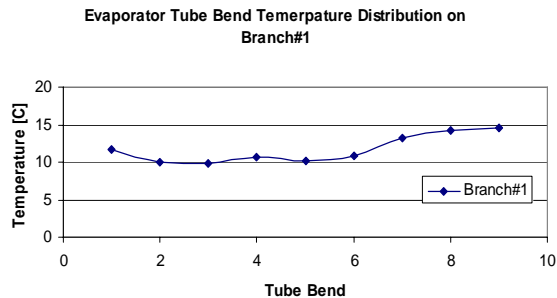
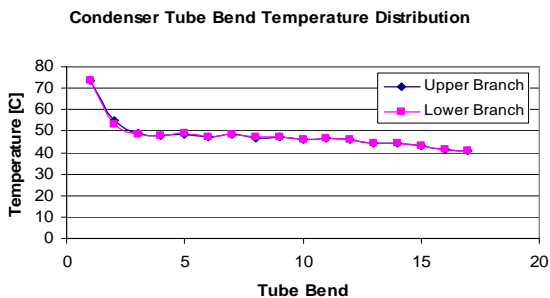


CFM=1100

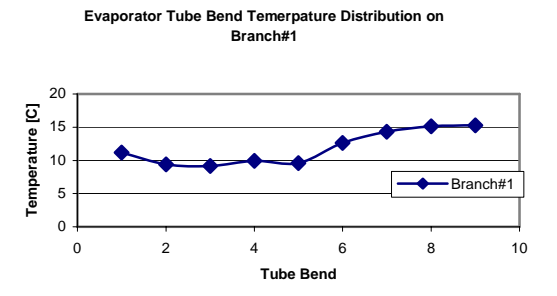
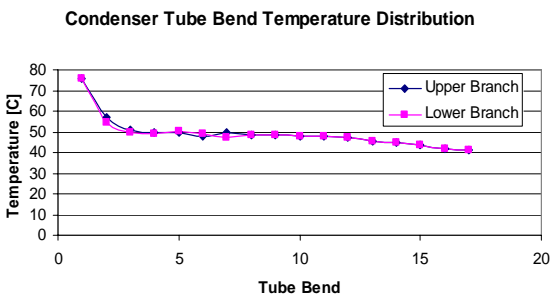


CFM=1200

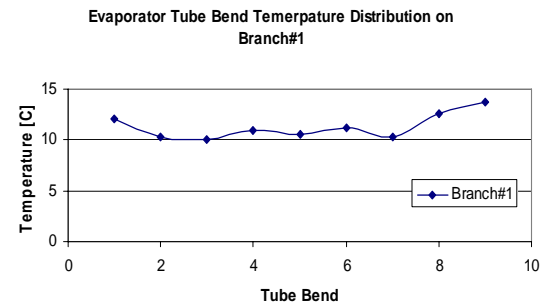
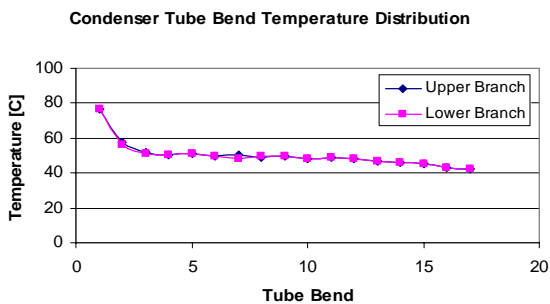
A.5 Varying Condenser Air Flow (Wet)



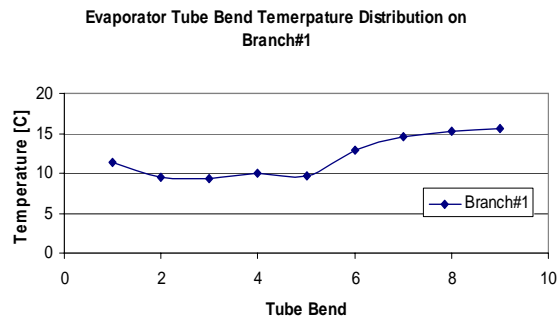
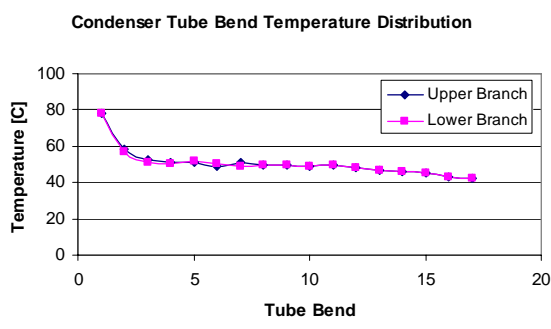
CFM=2520



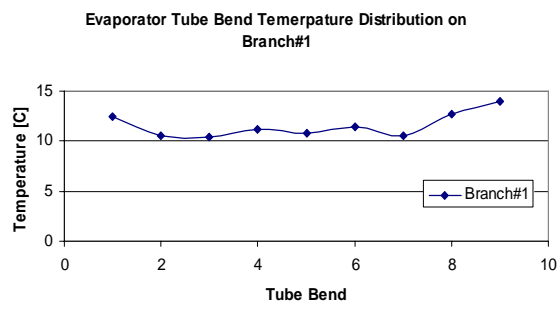
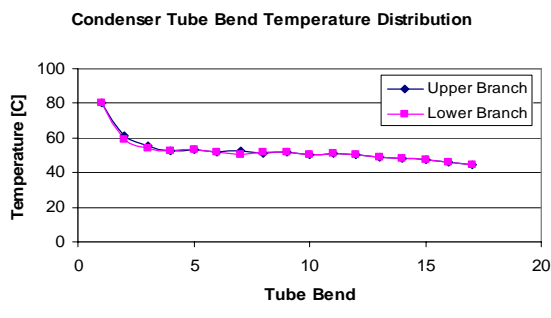
CFM=2240



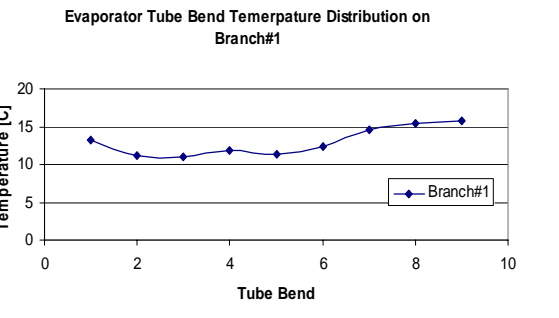
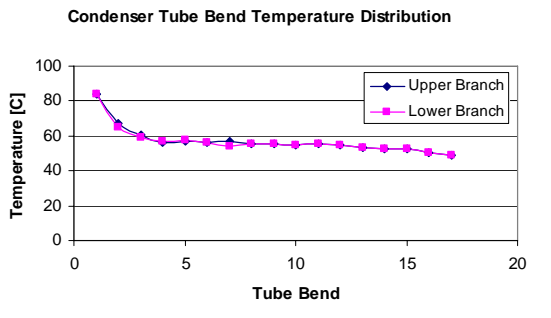
CFM=2234



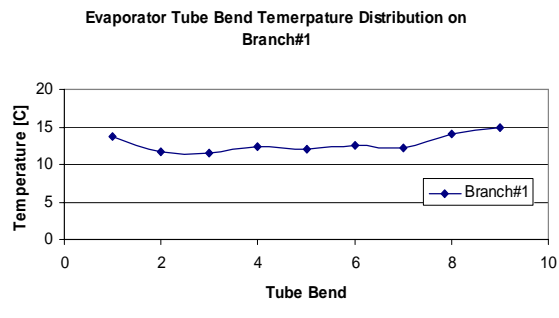
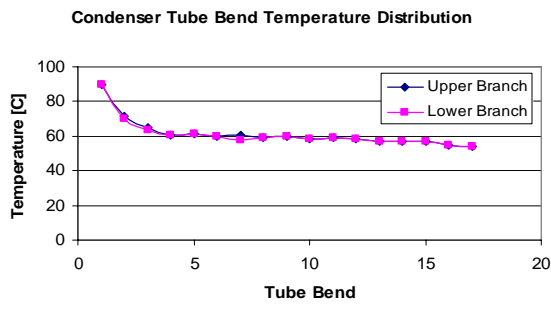
CFM=2162



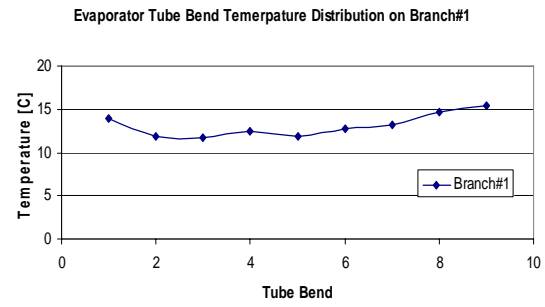
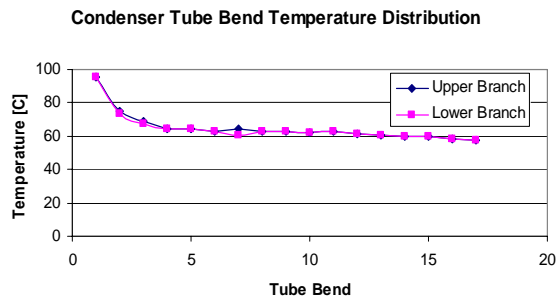
CFM=1799



CFM=1589



CFM=1227



CFM=853